

DUDLEY KNOX LIBRARY
NAVAL POSTGRADUATE SCHOOL
MONTEREY CALIFORNIA 93943-5002

NAVAL POSTGRADUATE SCHOOL

Monterey, California



THESIS

DEVELOPMENT OF A NEW METHOD OF MEASURING THE
CHARACTERISTIC IMPEDANCE AND COMPLEX WAVE
NUMBER OF A POROUS ACOUSTIC MATERIAL

by

Frederick Fay Schulz

June 1987

Thesis Advisors:

S. R. Baker
A. A. Atchley

Approved for public release; distribution is unlimited.

T233656

REPORT DOCUMENTATION PAGE

1a REPORT SECURITY CLASSIFICATION UNCLASSIFIED			1b RESTRICTIVE MARKINGS	
2a SECURITY CLASSIFICATION AUTHORITY			3 DISTRIBUTION / AVAILABILITY OF REPORT Approved for public release; Distribution is Unlimited	
2b DECLASSIFICATION / DOWNGRADING SCHEDULE				
4 PERFORMING ORGANIZATION REPORT NUMBER(S)			5 MONITORING ORGANIZATION REPORT NUMBER(S)	
6a NAME OF PERFORMING ORGANIZATION Naval Postgraduate School		6b OFFICE SYMBOL (If applicable) 61	7a NAME OF MONITORING ORGANIZATION Naval Postgraduate School	
6c ADDRESS (City, State, and ZIP Code) Monterey, California 93943-5000			7b ADDRESS (City, State, and ZIP Code) Monterey, California 93943-5000	
8a NAME OF FUNDING / SPONSORING ORGANIZATION		8b OFFICE SYMBOL (If applicable)	9 PROCUREMENT INSTRUMENT IDENTIFICATION NUMBER	
8c ADDRESS (City, State, and ZIP Code)			10 SOURCE OF FUNDING NUMBERS	
			PROGRAM ELEMENT NO	PROJECT NO
			TASK NO	WORK UNIT ACCESSION NO
11 TITLE (Include Security Classification) DEVELOPMENT OF A NEW METHOD OF MEASURING THE CHARACTERISTIC IMPEDANCE AND COMPLEX WAVE NUMBER OF A POROUS ACOUSTIC MATERIAL				
12 PERSONAL AUTHOR(S) Schulz, Frederick F.				
13a TYPE OF REPORT Master's Thesis		13b TIME COVERED FROM _____ TO _____	14. DATE OF REPORT (Year, Month, Day) 1987 June	
15 PAGE COUNT 128				
16 SUPPLEMENTARY NOTATION				
17 COSATI CODES			18 SUBJECT TERMS (Continue on reverse if necessary and identify by block number)	
FIELD	GROUP	SUB-GROUP	Characteristic Impedance, Complex Wave Number, Biot Theory, DC Flow Resistance, Fluid Saturated Porous Solid, Resonance Curve	
19 ABSTRACT (Continue on reverse if necessary and identify by block number)				
<p>The specific DC flow resistance, characteristic impedance and complex wave number of air-filled fiberglass have been extracted from measurements of the peak and half-power frequencies of the two lowest-frequency normal modes of a rectangular plexiglass cavity partially filled with fiberglass. Using Biot theory [Ref's. 8, 9 and 10] to describe the sound field within the fiberglass, a dispersion relation for the allowed modes in the cavity was derived, from which the above properties were extracted. The values determined by this new method compared favorably (within 25%) with the results of measurements using classical methods. The new method differs from the classical resonance tube method [Ref. 4] by 1) the use of a wave theory to describe the sound field within the fiberglass</p>				
20 DISTRIBUTION / AVAILABILITY OF ABSTRACT <input checked="" type="checkbox"/> UNCLASSIFIED/UNLIMITED <input type="checkbox"/> SAME AS RPT <input type="checkbox"/> DTIC USERS			21. ABSTRACT SECURITY CLASSIFICATION UNCLASSIFIED	
22a. NAME OF RESPONSIBLE INDIVIDUAL Steven R. Baker			22b TELEPHONE (Include Area Code) 408-646-2732	22c OFFICE SYMBOL 61Ba

19. (continued)

2) the use of a mode with particle velocity parallel to the air-fiberglass interface. The differences make it possible to extract the acoustic properties of bulk fiberglass using only a thin sample.

Approved for public release; distribution is unlimited.

Development of a New Method of Measuring the Characteristic Impedance and
Complex Wave Number of Porous Acoustic Material

by

Frederick Fay Schulz
Lieutenant, United States Navy
B.S., United States Naval Academy, 1980

Submitted in partial fulfillment of the
requirements for the degree of

MASTER OF SCIENCE IN ENGINEERING ACOUSTICS

from the

NAVAL POSTGRADUATE SCHOOL
June 1987

5-452
ABSTRACT

The specific DC flow resistance, characteristic impedance and complex wave number of air-filled fiberglass have been extracted from measurements of the peak and half-power frequencies of the two lowest-frequency normal modes of a rectangular plexiglass cavity partially filled with fiberglass. Using Biot theory [Ref's 8, 9 and 10] to describe the sound field within the fiberglass, a dispersion relation for the allowed modes in the cavity was derived, from which the above properties were extracted. The values determined by this new method compared favorably (within 25%) with the results of measurements using classical methods. The new method differs from the classical resonance tube method [Ref. 4] by 1) the use of a wave theory to describe the sound field within the fiberglass and 2) the use of a mode with particle velocity parallel to the air-fiberglass interface. The differences make it possible to extract the acoustic properties of bulk fiberglass using only a thin sample.

ACKNOWLEDGEMENT

I would like to thank the Naval Postgraduate School Foundation Research Council for its interest in funding of this research. Also I would like to express my deepest gratitude to the following individuals: Professor Steven Baker for his patience, guidance and extensive knowledge in the propagation of sound in fluid-saturated porous solids, George Jaksha, who manufactured many of the experimental components used, and Lab Technician Greg Pless for his time and energy providing his experience in the use of the experiment's equipment.

LIST OF CONTENTS

I.	INTRODUCTION -----	11
A.	BACKGROUND-----	11
B.	HISTORY OF CHARACTERISTIC IMPEDANCE AND COMPLEX WAVE NUMBER MEASURING TECHNIQUES-----	11
C.	PURPOSE OF STUDY-----	13
II.	THEORY-----	16
A.	THEORY OF A FLUID-SATURATED RIGID POROUS SOLID-----	16
	1. Development of Dispersion Relation in a Fluid-Filled Cavity Partially Filled With a Porous Solid-----	23
B.	CURRENT METHODS USING TRANSMISSION LINE THEORY-----	30
	1. Impedance Tube-----	31
	2. Resonance Analysis-----	34
	3. Yaniv's Method-----	35
C.	PROBE TUBE METHOD-----	37
D.	MATERIAL PROPERTIES METHOD-----	38
III.	EXPERIMENTAL AND RESULTS-----	41
A.	PROPERTIES OF THE POROUS SOLID-----	41
	1. Flow Resistance Measurements-----	42
	2. Viscous-Inertial Transition Frequency-----	48
B.	CLASSICAL METHODS USING TRANSMISSION LINE THEORY-----	49
	1. Impedance Tube Experiment and Results-----	49
	2. Resonance Analysis Experiment and Results-----	56
	3. Yaniv's Method, Experiment and Results-----	60
C.	PROBE TUBE METHOD, EXPERIMENT AND RESULTS-----	63
D.	MATERIAL PROPERTIES METHOD, EXPERIMENT AND RESULTS-----	65
E.	THE NEW METHOD, EXPERIMENT AND RESULTS-----	70

1. Modal Frequencies up to 2000 Hz for Various Fiberglass Thicknesses-----	75
2. Measured f_c and Q of the [100] and [010] Modes for Various Fiberglass Thicknesses-----	80
3. Source of Loss in the Empty Cavity-----	82
4. Determination of R_{DC} from f_c and Q of the [100] and [010] Modes-----	87
5. Sensitivity of Roots of the Dispersion Relation to Variation in Parameters-----	92
6. Modal Pressure Field for the [100] and [010] Modes-----	92
IV. COMPARISON OF RESULT AND CONCLUSION-----	113
A. COMPARISON OF THE COMPLEX WAVE NUMBER-----	113
B. COMPARISON OF THE CHARACTERISTIC IMPEDANCE-----	117
C. CONCLUSION-----	117
APPENDIX A. METHOD OF SOLUTION OF THE DISPERSION RELATION AND ITS IMPEMENTATION-----	120
APPENDIX B. DETERMINATION OF THE THEORETICAL MODAL PRESSURE DISTRIBUTION IN A PLANE WAVE RESONATOR WITH AN ACOUSTICALLY ABSORBING MATERIAL-----	124
LIST OF REFERENCES-----	125
INITIAL DISTRIBUTION LIST-----	127

LIST OF FIGURES

2.1	High and Low Frequency Limits on Porous Material's Phase Speed-	24
2.2	Geometry for New Theory in Rectangular Cavity-----	25
2.3	Geometry for the Impedance Tube-----	32
2.4	Geometry for Yaniv's Open Circuit Determination-----	36
2.5	Geometry for Yaniv's Short Circuit Determination-----	36
2.6	Chart for Determining the Magnitude of the Propagation Constant b of Rigid Tiles [Figure 19.3 OF Ref. 4, PP. 843]-----	40
2.7	Chart for Determining the Phase Angle of the Propagation Constance b of Rigid Tiles [Figure 19.4 OF Ref. 4, PP. 844]----	40
3.1	DC Flow Resistance Measurement Apparatus-----	43
3.2	Δp vs \dot{V} in Large Sample Holder-----	45
3.3	Δp vs \dot{V} in Small Sample Holder-----	50
3.4	Characteristic Length Scale of Pore Compared to δ_{visc} -----	50
3.5	Experimental Setup for Impedance Tube Method-----	54
3.6	Equipment Setup for Resonance Analysis Technique-----	57
3.7	Rigid Sliding Termination (Yaniv's Method)-----	61
3.8	Equipment Setup for Yaniv's Method-----	62
3.9	Equipment Setup for Probe Tube Experiment-----	66
3.10	Schematic of Probe Tube Extension-----	68
3.11	Grid Map for Rectangular Cavity-----	75
3.12	Experimental Setup for the New Method-----	78
3.13	Mode Structure of the Empty Cavity-----	79
3.14	Mode Structure of Cavity With 11/16" Fiberglass Strip (Sample #5)-----	81
3.15	Mode Structure of Cavity With 1-7/8" Fiberglass Strip (Sample #10)-----	81
3.16	[100] Mode Q_{TOT} vs f_C -- Bounding Flow Resistance-----	89
3.17	[100] Mode Q_F vs f_C -- Bounding Flow Resistance-----	90

3.18	[010] Mode Q_{TOT} vs f_C -- Bounding Flow Resistance-----	93
3.19	[010] Mode Q_F vs f_C -- Bounding Flow Resistance-----	94
3.20	[100] Mode of f_C vs Sample Thickness -- Bounding Flow Resistance-----	95
3.21	[010] Mode of f_C vs Sample Thickness -- Bounding Flow Resistance-----	96
3.22	$ \tilde{z}_{char} /\rho_0 c$ vs f For the New Technique {[100] and [010] Modes}-	97
3.23	$\phi_{z_{char}}$ vs f For the New Technique {[100] and [010] Modes}-----	97
3.24	k vs f For the New Technique {[100] and [010] Modes}-----	98
3.25	a vs f For the New Technique {[100] and [010] Modes}-----	98
3.26	c_{ph} vs f For the New Technique {[100] and [010] Modes}-----	99
3.27	Theoretical [100] Mode Pressure Distribution For Sample #1-----	103
3.28	Theoretical [100] Mode Pressure Distribution For Sample #10----	104
3.29	Experimental [100] Mode Pressure Distribution For Sample #1----	105
3.30	Experimental [100] Mode Pressure Distribution For Sample #10---	106
3.31	Theoretical [010] Mode Pressure Distribution For Sample #1-----	107
3.32	Theoretical [010] Mode Pressure Distribution For Sample #5-----	108
3.33	Experimental [010] Mode Pressure Distribution For Sample #1----	109
3.34	Experimental [010] Mode Pressure Distribution For Sample #5----	111
4.1	k vs f (All Methods)-----	114
4.2	a vs f (All Methods)-----	115
4.3	c_{ph} vs f (All Methods)-----	116
4.4	$ \tilde{z}_{char} /\rho_0 c$ vs f (All Methods)-----	118
4.5	$\phi_{z_{char}}$ vs f (All Methods)-----	119

LIST OF TABLES

1.	ADVANTAGES AND DISADVANTAGES OF METHODS TO DETERMINE CHARACTERISTIC IMPEDANCE AND COMPLEX WAVE NUMBER-----	14
2.	DC FLOW RESISTANCE MEASUREMENT DATA: LARGE SAMPLE HOLDER (FLOW NORMAL TO FIBERGLASS SURFACE)-----	46
3.	DC FLOW RESISTANCE MEASUREMENT RESULTS (FLOW NORMAL TO FIBERGLASS SURFACE)-----	47
4.	DC FLOW RESISTANCE MEASUREMENT DATA AND RESULTS SMALL SAMPLE HOLDER (FLOW NORMAL TO FIBERGLASS SURFACE)-----	51
5.	DC FLOW RESISTANCE MEASUREMENT DATA AND RESULTS SMALL SAMPLE HOLDER (FLOW PARALLEL TO FIBERGLASS SURFACE)-----	52
6.	IMPEDANCE TUBE MEASUREMENT RESULTS ON 12" OF FIBERGLASS-----	55
7.	RESONANCE ANALYSIS SURFACE IMPEDANCE RESULTS (IMPEDANCE TUBE AND CAVITY)-----	58
8.	YANIV'S METHOD EXPERIMENTAL RESULTS-----	64
9.	PROBE TUBE EXPERIMENTAL RESULTS ON 12" OF FIBERGLASS-----	69
10.	MATERIAL PROPERTIES METHOD EXPERIMENTAL RESULTS (ISOTHERMAL LIMIT)-----	72
11.	MATERIAL PROPERTIES METHOD EXPERIMENTAL RESULTS (ADIABATIC LIMIT)-----	73
12.	RECTANGULAR CAVITY FIBERGLASS SAMPLES-----	77
13.	RESONANCE MODES OF THE EMPTY CAVITY (THEORETICAL AND MEASURED)	79
14.	[100] MODE f_c AND Q EXPERIMENTAL RESULTS-----	83
15.	[010] MODE f_c AND Q EXPERIMENTAL RESULTS-----	84
16.	\tilde{k} AND \tilde{z}_{char} RESULTS FOR THE [100] MODE-----	100
17.	\tilde{k} AND \tilde{z}_{char} RESULTS FOR THE [010] MODE-----	101

I. INTRODUCTION

A. BACKGROUND

Elastic wave propagation in a fluid-saturated porous solid is a very important and active subject of research with a wide spectrum of applications including oil prospecting, nuclear test ban treaty verification and sound transmission and reflection at the ocean floor.

When the fluid in the pores is highly compressible (air for example) the acoustic properties are completely determined by the characteristic impedance, \tilde{Z}_{char} , or, equivalently by the complex wave number, \tilde{k} . From these quantities can be extracted parameters which depend only on the microscopic geometry of the porous solid, the values of which can then be used when the fluid in the pores is not highly compressible (water for example). It is therefore desirable to have accurate and reliable methods by which these parameters can be measured.

B. HISTORY OF CHARACTERISTIC IMPEDANCE AND COMPLEX WAVE NUMBER MEASURING TECHNIQUES

Rayleigh (1929) [Ref. 1, p. 328] has investigated the performance of an idealized absorber of sound consisting of small bundles of tubes. He extended the theories of Helmholtz and Kirchhoff that relate to the transmission of sound along tubes and was able to deduce a value for the absorption coefficient at the surface of such a material in terms of the propagation of the surface area occupied by the open pores, the radius of the tubes, and the physical constants of air. This analysis has provided a basis on which to found more general theories and description of sound propagation through porous materials.

Scott (1945) [Ref. 2] proposed a method of determining the complex wave number, \tilde{k} which describes the spatial variation of the acoustic disturbance in a porous medium. This method consists of measuring the attenuation constant and the wavelength constant of a plane progressive wave by probing the porous medium with a probe tube microphone. Scott then determined the characteristic impedance of the material with an apparatus devised by H. O. Taylor (1913) [Ref. 3] to measure the sound damping effects of acoustical materials. This apparatus is similiar to the present day impedance tube.

Beranek (1949) [Ref. 4] describes several methods of obtaining a material's acoustic impedance by measuring the properties of the sound field in the vicinity of an absorbing material exposed to a normally incident sound wave. Two of the most tractable methods are based on transmission line theory: the impedance tube method and the resonance method (normal incidence), with the latter method generally being viable only for determining surface impedance. Beranek also developed a method to calculate the complex propagation constant from measurements of a material's characteristic properties, i.e. porosity, pore size, etc. Once these properties are determined, the characteristic impedance can be calculated.

More recently, Yaniv (1973) [Ref. 5] developed a new method of calculating both the complex propagation constant $\gamma = jk$ and characteristic impedance of a material using transmission line theory applied to an impedance tube device. His method consists of measuring standing wave properties in the proximity of an absorbing material alternately backed with a high impedance and a low impedance termination.

Finally, in 1980, Chung and Blaser [Ref. 6] published their article discussing a Dual-Microphone Transfer Function technique for measuring in-duct acoustic properties, namely the acoustic impedance and reflection

coefficient from which the complex wave number can be determined. This technique was compared to the conventional Standing Wave Tube technique and found to give similar results [Ref. 7].

C. PURPOSE OF STUDY

The objective of this research is to investigate the feasibility of obtaining the characteristic impedance and the complex wave number of a fluid-filled porous solid by measuring the resonance frequencies and half-power widths of a fluid-filled rectangular cavity which is partially occupied by a porous solid of varying thickness. In this investigation, the fluid is air, the porous solid is fiberglass and the cavity is made of plexiglass.

This investigation differs from previous investigations in that 1) Biot Theory [Ref. 8, 9, 10, and 11] is applied to solve for the allowed modes of the partially-filled cavity, and 2) for the primary mode of interest the particle velocity is directed along the length of the fluid-porous solid boundary as opposed to normal to this boundary.

Table 1 summarizes the advantages in the course of this research. The advantage of this technique over the currently existing methods is that it does not require probing the sound field either within or in front of the porous solid as do methods 1, 2, 3, and 5, nor does it require a pair of phase-matched microphones as does method 6. Additionally, characteristic properties of an absorbing material need not be known as in method 4. Also, the acoustic properties of the bulk fiberglass can be determined using only thin samples.

The theory developed for the new method is presented in Chapter II along with a general overview of the equations used in the classical methods. The experimental results for each of the methods used in comparison are presented in Chapter III and comparisons are made and discussed in Chapter IV.

TABLE 1

ADVANTAGES AND DISADVANTAGES OF METHODS USED TO DETERMINE THE CHARACTERISTIC IMPEDANCE AND COMPLEX WAVE NUMBER

<u>Method</u>	<u>Advantages</u>	<u>Disadvantages</u>
1. Probe Tube (Scott)	a) Simple theory.	a) Thick sample needed to get characteristic impedance without a wave model for the porous medium.
	b) Simple procedure.	b) Must probe sound field.
2. Impedance Tube (Beranek)	a) Simple theory.	a) Thick sample needed to get characteristic impedance without a wave model for porous medium.
	b) Simple procedure.	
	c) Probing of material not required.	
	d) Normal absorption easy to measure.	
3. Resonance (Beranek)	a) Probing not required.	a) Theory is somewhat difficult.
	b) Measurement of resonance frequency and half power widths is precise.	b) Discrete frequencies.
		c) Measures surface impedance.
		d) Requires low losses for well defined resonances.
4. Material Properties (Beranek)	a) Sound wave not needed.	a) Complex theory.
		b) Measurement of microscopic properties is complex.

TABLE 1 (continued)

<u>Method</u>	<u>Advantages</u>	<u>Disadvantages</u>
		c) Requires classification of material as rigid or soft.
5. Yaniv	a) Simple theory. b) Simple procedure. c) Probing of material not necessary.	a) Time consuming. b) Quarter wavelength termination needs continuous adjustment with frequency.
6. Two Point Phase Difference (Chung and Blaser)	a) Simple theory. b) Simple procedure. c) Probing of material not necessary.	a) Thick sample needed. b) Microphone positions only optimum for select frequencies. c) Requires accurate microphone phase calibrations.
7. New Method (Baker)	a) Probing not required. b) Simple procedure. c) Ability to determine DC flow resistance non-invasively. d) Bulk properties obtained from thin samples.	a) Complex theory and numerical methods required. b) Discrete frequencies. c) Requires low losses for well defined resonances.

II. THEORY

The theory behind the new method is presented in detail in this section with much of the fundamental concepts and understanding having come from the investigation of sound propagation in a porous solid saturated with super-fluid Helium [Ref 11]. Additionally, the basic theory and equations used are presented for each of the classical methods used in comparison with the new techniques.

A. THEORY OF A FLUID-SATURATED RIGID POROUS SOLID

The linearized equation of motion for the microscopic fluid velocity \vec{v}_{micro} in the Eulerian description is [Ref. 12, p. 49],

$$\rho_f \left[\frac{\partial \vec{v}_{\text{micro}}}{\partial t} + (\vec{v}_{\text{micro}} \cdot \vec{\nabla}) \vec{v}_{\text{micro}} \right] = -\vec{\nabla} p + \eta \nabla^2 \vec{v}_{\text{micro}} + \left(\zeta + \frac{1}{3} \eta \right) \vec{\nabla} (\vec{\nabla} \cdot \vec{v}_{\text{micro}}). \quad (2.1)$$

Using

$$\nabla^2 \vec{v}_{\text{micro}} = \vec{\nabla} (\vec{\nabla} \cdot \vec{v}_{\text{micro}}) - \vec{\nabla} \times \vec{\nabla} \times \vec{v}_{\text{micro}}, \quad (2.2)$$

we can write Eq. (2.1) as

$$\rho_f \left[\frac{\partial \vec{v}_{\text{micro}}}{\partial t} + (\vec{v}_{\text{micro}} \cdot \vec{\nabla}) \vec{v}_{\text{micro}} \right] = -\vec{\nabla} p + \eta \vec{\nabla} \times \vec{\nabla} \times \vec{v}_{\text{micro}} + \left(\zeta + \frac{4}{3} \eta \right) \vec{\nabla} (\vec{\nabla} \cdot \vec{v}_{\text{micro}}), \quad (2.3)$$

Where ρ_f is the fluid mass density, p is the fluid pressure, η is the fluid shear viscosity and ζ is the fluid bulk viscosity. The last term in this equation can be ignored here because its affect is small compared to the other terms on the scale of a pore. Ignoring the last term, Eq. (2.3) becomes

$$\rho_f \left[\frac{D \vec{v}_{\text{micro}}}{D t} \right] = -\vec{\nabla} p - \eta \vec{\nabla} \times \vec{\nabla} \times \vec{v}_{\text{micro}}, \quad (2.4)$$

where $\frac{D\vec{v}_{\text{micro}}}{Dt}$ is the total time derivative of the microscopic fluid velocity. From Eq. (2.4), a phenomenological, linearized equation for the average (over the microscopic structure) fluid velocity, denoted $\langle \vec{v}_{\text{micro}} \rangle$, can be written:

$$\rho_{\text{eff}} \frac{\partial \langle \vec{v}_{\text{micro}} \rangle}{\partial t} = -\vec{\nabla} \langle p \rangle - R_{\text{flow}} \langle \vec{v}_{\text{micro}} \rangle . \quad (2.5)$$

Here ρ_{eff} is the phenomenological effective fluid mass density and R_{flow} is the phenomenological flow resistance [Ref. 13, pp. 252-255]. R_{flow} is defined such that in steady state

$$-\vec{\nabla} \langle p \rangle = R_{\text{DC}} \langle \vec{v}_{\text{micro}} \rangle . \quad (2.6)$$

In general (including oscillatory flow) ρ_{eff} and R_{flow} can be operationally defined by

$$\frac{1}{2} \rho_{\text{eff}} \langle \vec{v}_{\text{micro}} \rangle^2 = \text{kinetic energy per unit fluid volume} \quad (2.7)$$

$$R_{\text{flow}} \langle \vec{v}_{\text{micro}} \rangle^2 = \text{Rate of dissipation of kinetic energy density} \quad (2.8)$$

For $e^{j\tilde{\omega}t}$ time dependence, Eq. (2.5) can be written, upon combining both velocity terms on the left hand side,

$$\left[j\tilde{\omega} \rho_{\text{eff}}(\tilde{\omega}) + R_{\text{flow}}(\tilde{\omega}) \right] \langle \vec{v}_{\text{micro}} \rangle = -\vec{\nabla} \langle \tilde{p} \rangle , \quad (2.9)$$

where ρ_{eff} and R_{flow} are now frequency dependent phenomenological properties which describe the effect on the fluid due to the microscopic geometry [Ref. 11, pp. 334-335]. It should be noted that in Eq. (2.9) and in the remainder of this thesis complex quantities are denoted by a tilde.

Defining complex effective density, $\tilde{\rho}_{\text{eff}}(\tilde{\omega})$, as

$$\tilde{\rho}_{\text{eff}}(\tilde{\omega}) = \rho_{\text{eff}}(\tilde{\omega}) + \frac{R_{\text{flow}}(\tilde{\omega})}{j\tilde{\omega}} , \quad (2.10)$$

Eq. (2.9) may be written in a more compact form as

$$j\tilde{\omega}\tilde{\rho}_{\text{eff}}(\tilde{\omega}) \langle \tilde{\vec{v}}_{\text{micro}} \rangle = -\vec{\nabla} \langle \tilde{p} \rangle . \quad (2.11)$$

Plane progressive wave solutions to Eq. (2.11) travelling in the positive x-direction may be sought by letting the acoustic pressure be given by $\tilde{\delta p} e^{j(\tilde{\omega}t - \tilde{k}x)}$ and letting $\langle \tilde{\vec{v}}_{\text{micro}} \rangle = \tilde{\vec{v}}_{\text{avg}} e^{j(\tilde{\omega}t - \tilde{k}x)}$, where $\tilde{k} = k - ja$ with $k, a > 0$ such that the energy of the wave exponentially decays as one moves deeper into the porous solid (note in order to avoid confusion later, the letter a will be used to denote the attenuation constant, reserving the letter α for the tortuosity in the Biot theory). Eq. (2.11) then becomes

$$j\tilde{\omega} \tilde{\rho}_{\text{eff}}(\tilde{\omega}) \tilde{\vec{v}}_{\text{avg}} = j \tilde{k} \tilde{\delta p} . \quad (2.12)$$

The microscopic equation of continuity for $\tilde{\vec{v}}_{\text{micro}}$ still holds for $\langle \tilde{\vec{v}}_{\text{micro}} \rangle$ if we consider a large enough volume so that irregularities on the order of the pore size average out, and if we consider the density of the fluid in the pores to oscillate about the bulk fluid density with the passing of an acoustic disturbance. Hence we let $\tilde{\rho} = \rho_f + \tilde{\delta \rho} e^{j(\tilde{\omega}t - \tilde{k}x)}$ and the equation of continuity becomes, to first order,

$$j\tilde{\omega}\tilde{\delta \rho} - j\rho_f \tilde{k} \tilde{\vec{v}}_{\text{avg}} = 0 . \quad (2.13)$$

The relation between pressure and density variations (the equation of state) in a fluid-saturated porous solid can be written

$$\frac{\tilde{\delta p}}{\tilde{\delta \rho}} = c_f^2 \frac{\tilde{\gamma}(\tilde{\omega})}{\gamma} , \quad (2.14)$$

where c_f is the speed of sound in the bulk fluid, $\tilde{\gamma}(\tilde{\omega})$ is the complex ratio of specific heats (c_p/c_v) as a function of frequency, and γ is the adiabatic ratio of specific heats.

Eq's. (2.12), (2.13) and (2.14) lead to a wave equation with the phase velocity determined as follows: writing Eq. (2.12) (the equation of motion) as

$$\frac{\tilde{\omega}}{K} \tilde{\rho}_{eff}(\tilde{\omega}) \tilde{v}_{avg} = \frac{\delta \tilde{p}}{\delta \tilde{\rho}} \delta \tilde{\rho} \quad (2.15)$$

and substituting Eq. (2.14) into it results in

$$\frac{\tilde{\omega}}{K} \tilde{\rho}_{eff}(\tilde{\omega}) \tilde{v}_{avg} = c_f^2 \frac{\tilde{\gamma}(\tilde{\omega})}{\gamma} \delta \tilde{\rho} \quad (2.16)$$

Recasting Eq. (2.13) (continuity) as $\rho_f \tilde{v}_{avg} = \frac{\tilde{\omega}}{K} \delta \tilde{\rho}$ and dividing Eq. (2.16) by it results in

$$\left(\frac{\tilde{\omega}}{K}\right)^2 = c_f^2 \frac{\tilde{\gamma}(\tilde{\omega})}{\gamma} \cdot \frac{1}{\frac{\tilde{\rho}_{eff}(\tilde{\omega})}{\rho_f}} \quad (2.17)$$

Defining the complex tortuosity in the fluid saturated porous solid by [Ref. 8, p. 185 and Ref. 11, p. 37]

$$\tilde{\alpha}(\tilde{\omega}) = \frac{\tilde{\rho}_{eff}(\tilde{\omega})}{\rho_f} \quad , \quad (2.18)$$

the phase velocity can be written as

$$\tilde{c}^2 = \left(\frac{\tilde{\omega}}{K}\right)^2 = \frac{c_f^2}{\tilde{\alpha}(\tilde{\omega})} \frac{\tilde{\gamma}(\tilde{\omega})}{\gamma} \quad (2.19)$$

The complex tortuosity can be written as

$$\tilde{\alpha}(\tilde{\omega}) = \alpha + \frac{R_{DC} \tilde{F}(\tilde{\omega})}{j \tilde{\omega} \rho_f} \quad (2.20)$$

where α is the intrinsic, or infinite frequency (inviscid) tortuosity, and $\tilde{F}(\tilde{\omega})$ is a dimensionless correction function whose purpose is to make the frequency dependence of $\tilde{\alpha}(\tilde{\omega})$ come out right [Ref. 8, p. 185 and Ref. 11, p. 37].

The complex tortuosity can be written in the form [Ref. 11, p. 49]

$$\tilde{\alpha}(\tilde{\omega}) = \alpha - j\tilde{r}\tilde{F}(\tilde{\omega}) \quad , \quad (2.21)$$

where

$$\tilde{r} = \frac{R_{DC}}{\tilde{\omega}\rho_f} \quad (2.22)$$

is a dimensionless flow resistance.

The mathematical form for the dimensionless correction function can be taken as [Ref. 11, p. 57 and Ref. 14]

$$\tilde{F}(\tilde{\omega}) = 1 + j\left(\frac{\tilde{\kappa}}{4}\right)^2 \quad , \quad (2.23)$$

where

$$\tilde{\kappa} = \delta\left(\frac{\tilde{r}}{\alpha}\right)^{-1/2} \quad . \quad (2.24)$$

Here δ is the structural factor in Biot's universal correction function and α is the intrinsic tortuosity of the microscopic pore geometry [Ref. 10].

The intrinsic tortuosity is a weighted path length correction factor which satisfies $\alpha \geq 1$. It depends most strongly on porosity P , with $\alpha \rightarrow 1$ as $P \rightarrow 1$ (as is the case for fiberglass). Typical values range from 1 to 4 [Ref. 11, p. 227 and Ref. 15].

The DC flow resistance is proportional to $\eta/(\text{pore size})^2$, so that

$$\frac{\tilde{r}}{\alpha} \sim \frac{\eta}{\alpha\tilde{\omega}\rho_f} \cdot \frac{1}{(\text{pore size})^2} \sim \left(\frac{\text{viscous penetration depth}}{\text{pore size}}\right)^2 \quad . \quad (2.25)$$

The quantity \tilde{r}/α determines the relative importance of flow resistance versus fluid inertia in determining the microscopic flow field.

The structural δ depends upon the average cross-sectional shape of a pore [Ref. 8, p. 185]. Experimentally it appears that $\delta \approx 4$ for many granular porous solids [Ref. 16].

Substituting Eq. (2.22), (2.23) and (2.24) into Eq. (2.21) results in

$$\tilde{\alpha}(\tilde{\omega}) = \alpha \{ 1 - j \left(\frac{R_{DC}}{\alpha \tilde{\omega} \rho_F} \right) [1 + j \left(\frac{\delta}{4} \right)^2 \left(\frac{\alpha \tilde{\omega} \rho_F}{R_{DC}} \right)]^{1/2} \} . \quad (2.26)$$

For all calculations in this research it will be assumed that $\alpha=1$ and $\delta=4$ for fiberglass [Ref. 11, pp. 49-59].

The complex ratio of specific heats, $\tilde{\gamma}(\tilde{\omega})$, is defined as

$$\tilde{\gamma}(\tilde{\omega}) = \tilde{c}_p / \tilde{c}_v \quad (2.27)$$

where \tilde{c}_p and \tilde{c}_v are, respectively, the complex, frequency dependent specific heats per gram at constant pressure and at constant volume. For an ideal gas $\tilde{c}_p - \tilde{c}_v = \frac{R}{M}$, where M is the molar mass, and so

$$\tilde{\gamma}(\tilde{\omega}) = 1 + \frac{R}{M \tilde{c}_v} . \quad (2.28)$$

The propagation of sound in the porous medium will vary from isothermal at low frequencies when the thermal penetration depth is large compared to a pore size, hence $\tilde{c}_v \rightarrow \infty$, to adiabatic at high frequencies when the thermal penetration depth is small compared to a pore size, and $\tilde{c}_v =$ bulk fluid value. Since the transport of momentum and energy in a gas both arise from molecular collisions, it will be assumed that the functional form $(\tilde{\gamma} - 1)$ has the same form as the complex tortuosity $\tilde{\alpha}(\tilde{\omega})$, only with the thermal penetration depth δ_{th} in place of the viscous penetration depth δ_{visc} . Hence we take [S. Baker, private communication]

$$\tilde{\gamma}(\tilde{\omega}) = 1 + \frac{(\gamma-1)}{1-j \tilde{\gamma} F(\tilde{\omega}) \cdot \frac{\delta_{th}^2}{\delta_{visc}^2}} \quad (2.29)$$

where \tilde{r} and $\tilde{F}(\tilde{\omega})$ are given by Eq's (2.22) and (2.23), respectively. The viscous penetration depth, δ_{visc} , and the thermal penetration depth δ_{th} are defined by

$$\delta_{\text{visc}} = \sqrt{\frac{2\eta}{\omega\rho_f}} \quad \delta_{\text{th}} = \sqrt{\frac{2\kappa}{\omega\rho_f c_p}} \quad (2.30)$$

where η is the fluid shear viscosity, ρ_f is the bulk fluid density, κ is the thermal conductivity and c_p is the specific heat per gram at constant pressure.

The factor $\frac{\delta_{\text{th}}^2}{2\delta_{\text{visc}}}$ can be recast as

$$\frac{\delta_{\text{th}}^2}{2\delta_{\text{visc}}} = \frac{\chi}{\nu} = \frac{1}{\text{Pr}} \quad (2.31)$$

where

$$\nu = \eta/\rho_f \equiv \text{kinematic viscosity} \quad (2.32)$$

and

$$\chi = \kappa/\rho c_p \equiv \text{thermal diffusivity} \quad (2.33)$$

and $\text{Pr} \equiv$ Prandtl number which has a value of 0.733 for air at 20°C. Hence the complex ratio of specific heats can be rewritten as

$$\tilde{\gamma}(\tilde{\omega}) = 1 + \frac{(\gamma-1)}{1-j\tilde{r}} \frac{\tilde{F}(\tilde{\omega})}{\text{Pr}} \quad (2.34)$$

In the high frequency limit, the square of the phase velocity in the porous material (Eq. 2.19) goes to the fluid inertia dominated limit in which sound propagates at the bulk fluid speed reduced by the square root of the tortuosity. Conversely, in the low frequency limit, flow resistance

dominates, and pressure oscillations diffuse through the porous material. The crossover from inertia dominance to flow resistance dominance occurs when the viscous penetration depth is approximately equal to a characteristic pore size. Figure 2.1 summarizes the limiting conditions.

1. Development of Dispersion Relation in a Fluid-Filled Cavity Partially Filled With a Porous Solid

Consider a rectangular cavity which is partially filled with a fluid-saturated porous solid. The region occupied by bulk fluid is denoted as region 1; the region occupied by the fluid-saturated porous solid is identified as region 2. The porous solid is assumed homogeneous and isotropic. Figure 2.2 depicts the geometry used to develop the dispersion relation for standing waves in the cavity. It will be assumed that all cavity walls are perfectly rigid so that $\hat{n} \cdot \vec{u} = 0$. Then $\hat{n} \cdot \vec{\nabla} p = 0$ at these boundaries and the velocity potential in regions 1 and 2 can be written as follows:

In region 1 (bulk fluid),

$$\tilde{\phi}_1 = \tilde{\phi}_{10} e^{j\tilde{\omega}t} \cos[k_x x] \cos[\tilde{k}_{1z}(z-d_1)] \quad (2.35)$$

where

$$k_x = \frac{n\pi}{L} ; \quad n = 0, 1, 2, \dots , \quad (2.36)$$

$$\tilde{\omega}^2 = (k_x^2 + \tilde{k}_{1z}^2) c_f^2 \quad (2.37)$$

$$c_f^2 = B_f / \rho_f , \quad (2.38)$$

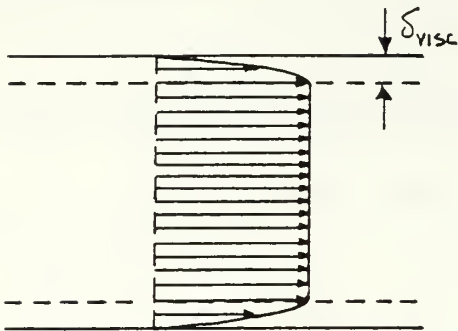
and

B_f = bulk modulus of fluid

$\tilde{\phi}_{10}$ = complex amplitude of the velocity potential in region 1.

High and Low Frequency Limits on Phase Velocity in a Porous Material

High Frequency Limit



Plug Flow

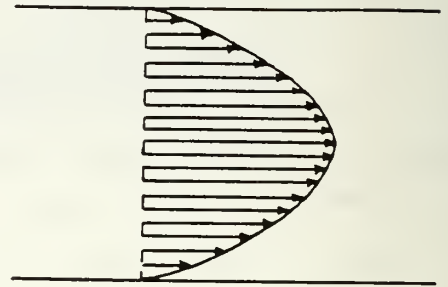
$$\tilde{\alpha}(\tilde{\omega}) \rightarrow \alpha_{\infty}$$

$$\tilde{\gamma}(\tilde{\omega}) \rightarrow \gamma$$

$$\tilde{c}^2 \rightarrow \frac{c_F^2}{\alpha_{\infty}}$$

- Fluid Inertia Dominates
- Sound Propagates

Low Frequency Limit



Laminar Flow

$$\tilde{\alpha}(\tilde{\omega}) \rightarrow -j \frac{R_{DC}}{\rho_F \tilde{\omega}}$$

$$\tilde{\gamma}(\tilde{\omega}) \rightarrow 1$$

$$\tilde{c}^2 \rightarrow j \frac{c_F^2 \tilde{\omega} \rho_F}{\gamma R_{DC}}$$

- Flow Resistance Dominates
- Sound does not Propagate
(Pure Diffusion)

Cross-over when:

$\delta_{visc} \approx \text{characteristic pore size}$

Figure 2.1 High and Low Frequency Limits on Phase Velocity in a Porous Material

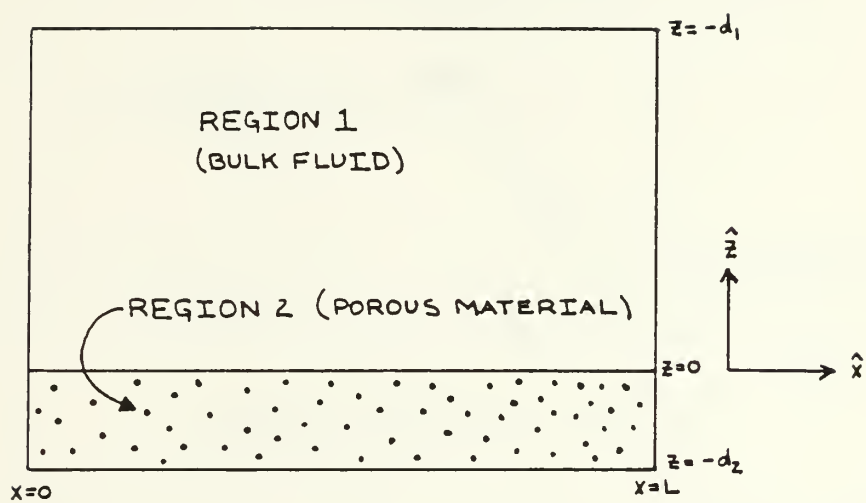


Figure 2.2 Rectangular Cavity Geometry for New Method.

The x-component of the wave number is a pure real number since the boundary conditions of rigid walls normal to the x-direction at $x = 0$ and $x = L$ force real and discrete values for k_x .

In region 1 the particle velocity can be written as

$$\vec{\tilde{v}}_1 = \vec{\nabla} \tilde{\phi}_1 \quad (2.39)$$

and the pressure as

$$\tilde{p}_1 = -j\tilde{\omega} \rho_F \tilde{\phi}_1. \quad (2.40)$$

In region 2 (porous material),

$$\tilde{\phi}_2 = \tilde{\phi}_{20} e^{j\tilde{\omega}t} \cos[k_x x] \cos[\tilde{k}_{2z}(z+d_2)] \quad (2.41)$$

where

$$k_x = \frac{n\pi}{L}; \quad n = 0, 1, 2, \dots, \quad (2.42)$$

$$\tilde{\omega}^2 = (k_x^2 + \tilde{k}_{2z}^2) \tilde{c}_2^2, \quad (2.43)$$

$$\tilde{c}_2^2 = \frac{c_F^2}{\tilde{\alpha}(\tilde{\omega})} \frac{\tilde{\gamma}(\tilde{\omega})}{\gamma}, \quad (2.44)$$

and

$\tilde{\phi}_{20}$ = complex amplitude of the velocity potential in region 2.

The particle velocity in region 2 is

$$\vec{\tilde{v}}_2 = \vec{\nabla} \tilde{\phi}_2 \quad (2.45)$$

and the pressure is, from Eq. (2.11),

$$\tilde{p}_2 = -j\tilde{\omega} \tilde{\alpha}(\tilde{\omega}) \rho_F \tilde{\phi}_2. \quad (2.46)$$

With the velocity potentials defined in both regions 1 and 2 all that is left is to match conditions at the boundary between the bulk fluid and porous material (i.e., at $z = 0$) to produce the desired dispersion relation. The two boundary conditions that must be satisfied at $z = 0$ are:

1. continuity of pressure across the boundary:

$$\tilde{\phi}_1(z=0) = \tilde{\alpha}(\tilde{\omega}) \tilde{\phi}_2(z=0) \quad (2.47)$$

and

2. continuity of the normal component of volume velocity:

$$\left. \frac{\partial \tilde{\phi}_1}{\partial z} \right|_{z=0} = P \left. \frac{\partial \tilde{\phi}_2}{\partial z} \right|_{z=0} , \quad (2.48)$$

where P is the porosity of the material. Applying boundary condition 1 results in

$$\tilde{\phi}_{10} \cos[\tilde{k}_{1z}d_1] = \tilde{\alpha}(\tilde{\omega}) \tilde{\phi}_{20} \cos[\tilde{k}_{2z}d_2] . \quad (2.49)$$

Applying boundary condition 2 results in

$$\tilde{\phi}_{10} \tilde{k}_{1z} \sin[\tilde{k}_{1z}d_1] = -\tilde{\phi}_{20} P \tilde{k}_{2z} \sin[\tilde{k}_{2z}d_2] . \quad (2.50)$$

Dividing Eq. (2.50) by Eq. (2.49) results in the dispersion relation

$$\tilde{k}_{1z} \tan[\tilde{k}_{1z}d_1] + \frac{P}{\tilde{\alpha}(\tilde{\omega})} \tilde{k}_{2z} \tan[\tilde{k}_{2z}d_2] = 0 , \quad (2.51)$$

where

$$\tilde{k}_{1z} = \left[\frac{\tilde{\omega}^2}{c_f^2} - k_x^2 \right]^{1/2} , \quad (2.52)$$

$$\tilde{k}_{2z} = \left[\frac{\tilde{\omega}^2}{c^2} \tilde{\alpha}(\tilde{\omega}) \frac{\gamma}{\tilde{\gamma}(\tilde{\omega})} - k_x^2 \right]^{1/2}, \quad (2.53)$$

and

$$k_x = \frac{n\pi}{L}; \quad n = 0, 1, 2, \dots \quad (2.54)$$

In Eq. (2.53) the forms of $\tilde{\alpha}(\tilde{\omega})$ and $\tilde{\gamma}(\tilde{\omega})$ have already been defined in Eq. (2.26) and Eq. (2.34), respectively. Eq. (2.51) is a transcendental equation in $\tilde{\omega}$ whose roots determine the natural frequencies and half power widths or, equivalently, the quality factors, of the allowed "standing wave" modes of this system. From these roots can be determined the complex wave numbers \tilde{k}_{1z} and \tilde{k}_{2z} and the resulting pressure distribution.

Two approaches to the use of the dispersion relation become evident. The first is the "forward" problem, where the roots of Eq. (2.51) for $\tilde{\omega}$ may be regarded as functions of R_{DC} and α , and measured resonance frequencies and Q 's may be compared with predictions; the second in the "inverse" problem, where R_{DC} and α are regarded as functions of the roots of Eq. (2.51) for $\tilde{\omega}$ and are found by variation such that the best fit is obtained between the measured and calculated spectra. The aim of this work is to verify the technique to solve the inverse problem by comparing the value of R_{DC} extracted from resonance data with that actually measured. Appendix A discusses the numerical technique to determine the roots of the dispersion relation and the algorithm used to determine the best fit value of R_{DC} .

Once the "best fit" value of R_{DC} has been determined, then, since the roots of the dispersion relation in terms of $\tilde{\omega}$ are known for this value of R_{DC} , the complex wave number is found from

$$\tilde{k} = \frac{\tilde{\omega}}{c} = k - ja \quad (2.56)$$

with \tilde{c} found from Eq's. (2.19), (2.26) and (2.34). The characteristic impedance can be calculated from

$$\tilde{Z}_{\text{char}} = \tilde{\rho}_{\text{eff}}(\tilde{\omega}) \tilde{c} \quad (2.57)$$

where $\tilde{\rho}_{\text{eff}}(\tilde{\omega})$ is given by Eq. (2.10). Normalizing the characteristic impedance to that of the bulk fluid ($\rho_0 c$) results in

$$\tilde{Z}_{\text{char}} (\text{normalized}) = \tilde{Z}_{\text{char}} / \rho_0 c \quad (2.58)$$

The complex pressure field for both regions may be calculated once the roots of Eq. (2.51) are found. The pressure distribution in region 1 can be written in terms of the velocity potential in region 1 as

$$\delta \tilde{p}_1 = -j \tilde{\omega} \rho_f \tilde{\phi}_1, \quad (2.59)$$

where $\tilde{\phi}_1$ is given by Eq. (2.35). The pressure distribution in region 2 can be written in terms of the velocity potential in region 2 as

$$\delta \tilde{p}_2 = -j \tilde{\omega} \tilde{\alpha}(\tilde{\omega}) \rho_f \tilde{\phi}_2, \quad (2.60)$$

where $\tilde{\phi}_2$ is given by Eq. (2.41).

The velocity potentials $\tilde{\phi}_1$ and $\tilde{\phi}_2$ are related by the boundary condition that pressure be continuous across the interface between the bulk fluid and the porous material, Eq. (2.47), which requires that

$$\tilde{\phi}_{10} \cos[\tilde{k}_1 z d_1] = \tilde{\alpha}(\tilde{\omega}) \tilde{\phi}_{20} \cos[\tilde{k}_2 z d_2] \quad (2.61)$$

For simplicity, choose $\tilde{\phi}_{20}$ to depend on $\tilde{\phi}_{10}$, resulting in

$$\tilde{\phi}_{20} = \frac{\tilde{\phi}_{10}}{\tilde{\alpha}(\tilde{\omega})} \frac{\cos \tilde{k}_1 z d_1}{\cos \tilde{k}_2 z d_2} \quad (2.62)$$

The pressure distribution in each region may be written as follows:

$$\delta \tilde{p}_1 = \left[-j \tilde{\omega} \rho_f \cos[k_x x] \cos[\tilde{k}_1 z(z-d_1)] \right] \tilde{\phi}_{10} e^{j \tilde{\omega} t}, \quad (2.63)$$

and for region 2,

$$\tilde{p}_2 = \left[-j\tilde{\omega} \rho_F \cos[k_x x] \frac{\cos \tilde{k}_{1z} d_1}{\cos \tilde{k}_{2z} d_2} \cos[\tilde{k}_{2z}(z+d_2)] \right] \tilde{\phi}_{10} e^{j\tilde{\omega}t} \quad (2.64)$$

With Eq. (2.63) and Eq. (2.64), and the values of \tilde{k}_{1z} and \tilde{k}_{2z} determined from the roots of the dispersion relation of Eq. (2.51), the pressure distribution throughout the cavity may be calculated. See Appendix B for a more detailed discussion of the pressure calculation.

B. CURRENT METHODS USING TRANSMISSION LINE THEORY

Three of the five classical methods for determining the characteristic impedance and complex wave number of a porous acoustic material are based on transmission line theory. These methods involve measurement of various properties of the standing wave and data are taken at various points somewhat removed from the sample surface [Ref. 4, pp. 317-321]. The three methods considered are:

- Impedance Tube Method
- Resonance Analysis Method
- Yaniv's Method

Only Yaniv's method allows direct determination of the material's characteristic impedance and complex wave number. The impedance tube method allows direct measurement of the resistive and reactive components of the surface impedance. The complex wave number can only be calculated if reflections from the far side of the porous material can be neglected and one has some knowledge of the complex effective mass density of the fluid in the pores. As developed by Beranek, the resonance analysis method measures the same quantities as the impedance tube method, with the same limitations. It is

discussed primarily for its similarity to the new technique in that the parameters of the resonance curve are measured.

1. Impedance Tube Method

In this method the non-dissipative acoustic transmission line is considered a smooth rigid-walled tube whose lateral dimensions are small compared to a wavelength. The losses at the wall and in the bulk volume are considered small compared to the losses associated with the absorbing material under test. Assuming that the source of sound is at one end of the tube ($x=0$) and the sample under test is located at the opposite end ($x=L$), the surface impedance can be determined. Figure 2.3 depicts the geometry of the impedance tube.

The impedance tube that has a constant cross section S and the source vibrates harmonically at a frequency sufficiently low that only plane waves can propagate. A standing wave pattern is set up by the right and left travelling waves and can be expressed mathematically as

$$\tilde{p} = \tilde{A} e^{j[\omega t + k(L-x)]} + \tilde{B} e^{j[\omega t - k(L-x)]} \quad (2.65)$$

where \tilde{p} is the acoustic pressure, \tilde{A} and \tilde{B} are determined from the boundary conditions at $x=0$ and $x=L$.

It has been shown [Ref. 17, pp. 200-206] that the surface impedance of the termination may be written in the form,

$$\frac{\tilde{z}_L}{\rho_0 c} = \frac{1 + B/A e^{j\theta}}{1 - B/A e^{j\theta}}, \quad (2.66)$$

where B/A is the ratio of the reflected wave amplitude to the incident wave amplitude and θ is the phase difference between the reflected and incident wave. Thus given B/A and θ , the surface impedance of the termination can be calculated.

Solving for the amplitude $|\tilde{p}|$ of the standing wave it can be seen that the amplitude at pressure antinode is $A+B$, and at a pressure node is $A-B$. The ratio of the pressure amplitude at an antinode to that at a node is the standing wave ratio, or SWR:

$$SWR = \frac{A+B}{A-B} = \frac{P_{anti}}{P_{node}}, \quad (2.67)$$

which can be rearranged to give the ratio B/A :

$$\frac{B}{A} = \frac{SWR-1}{SWR+1}. \quad (2.68)$$

Thus measurement of the SWR by probing the sound field in the impedance tube with a small microphone yields the value of B/A [Ref. 17, p. 206].

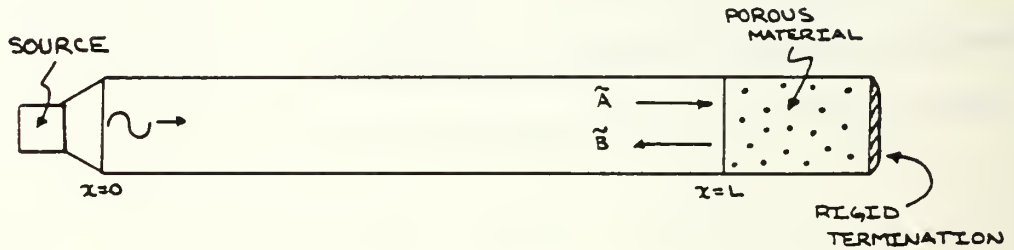


Figure 2.3 Geometry for the Impedance Tube

The phase angle θ can be evaluated from determining the distance to the first node from the end at $x=L$. These nodes are located at

$$k(L-x_n) - \theta/2 = (n-1/2)\pi; \quad n = 1, 2, \dots, \quad (2.69)$$

so that the phase angle for the first node is

$$\theta_1 = 2k(L-x_1) - \pi. \quad (2.70)$$

With the SWR and θ_1 known, the resistive and reactive portions of the impedance can be determined graphically using a "Smith" chart. To determine the characteristic impedance of the porous material, the sample thickness is increased such that the reflected wave from the rigid termination is insignificant compared to the incident wave. From the definition of the material's characteristic impedance, the complex wave number can be found assuming that we know how the fluid reacts in the pores of the material. The characteristic impedance may be written as

$$\tilde{Z}_{\text{char}} = \tilde{\rho}_{\text{eff}} \tilde{c} \quad (2.71)$$

where $\tilde{\rho}_{\text{eff}}$ is the complex effective fluid density in the pores and \tilde{c} is the phase velocity of the acoustic disturbance in the pores. The phase speed \tilde{c} in a fluid, can expressed as

$$\tilde{c}^2 = \tilde{B}_f / \tilde{\rho}_{\text{eff}} \quad (2.72)$$

where \tilde{B}_f is the complex bulk modulus of the fluid in the pores. Therefore Eq. (2.71) becomes, upon substituting Eq. (2.72) for $\tilde{\rho}_{\text{eff}}$,

$$\tilde{Z}_{\text{char}} = \tilde{B}_f / \tilde{c} \quad (2.73)$$

and since $\tilde{c} = \frac{\tilde{\omega}}{\tilde{k}}$, the equation that describes the complex wave number \tilde{k} can be written as

$$\tilde{k} = \frac{\tilde{\omega}}{\tilde{B}_f} \tilde{Z}_{\text{char}} \quad (2.74)$$

If it is assumed that the material pore size is small compared to the viscous and thermal penetration depths (in air these two parameters are approximately equal) in the frequency range of interest, we can write

$$\tilde{B}_f \approx B_T \quad (2.75)$$

where B_T is the isothermal bulk modulus of the fluid in the pores. Additionally for an ideal gas, the isothermal bulk modulus can be written as

$$B_T = 1/\kappa_T \quad (2.76)$$

where κ_T is the isothermal compressibility of the gas, and is equal to $1/P$, where P is the pressure in the pores [Ref. 18, p. 47]. Hence Eq. (2.74) can be written, assuming isothermal conditions exist, in the form,

$$\tilde{k} = \omega \kappa_T \tilde{z}_{\text{char}} \quad (2.77)$$

where $\tilde{k} = k - ja$, for a wave travelling in the positive x-direction in the porous solid. Eq. (2.77) is presented to show the relationship between the complex wave number and the characteristic impedance assuming isothermal conditions in the pore volume. This equation was used only to check Beranek's Material Properties Method in the isothermal limit. Only the values for \tilde{z}_{char} extracted by the impedance tube method are reported here.

2. Resonance Analysis Method

The resonance analysis method is used to determine the surface impedance of a porous acoustic material. This method requires low loss within the material to be successful. A resonance curve may be traced out by varying either the tube length or the frequency in this method. For the present research, the impedance tube discussed previously was used, with frequency swept to trace out a resonance.

Beranek presents the equation needed to determine the impedance of a sample under test and is rewritten here only for discussion [Ref. 4, pp. 329-334].

The normalized surface impedance of the sample is written,

$$\frac{\tilde{z}_{\text{surf}}}{\rho_0 c} = \frac{\psi/\phi + k_m/\omega_m}{1} \cong \coth [(k_m - j\omega_m)l/c] \quad (2.78)$$

where $\psi = |\tilde{z}_{\text{surf}}|/\rho_0 c$, ϕ being the phase angle of $|\tilde{z}_{\text{surf}}|$ and \tilde{z}_{surf} is the impedance at the surface of the sample which is to be determined. At

the resonance peak, the peak frequency ω_p is approximately equal to the normal angular frequency of longitudinal vibration, ω_m , or

$$\omega_p \approx \omega_m . \quad (2.79)$$

At the half power frequencies (-3 dB down from the peak) the half-power half width (HPHW) can be written as

$$\text{HPHW} = \frac{\omega_u - \omega_l}{\omega_p} = \frac{\omega_m k_1}{\omega_p} \approx k_1 , \quad (2.80)$$

where $k_1 = k_m + k_{na}$, and k_{na} is the spatial damping constant without the porous material present (i.e., it takes into account wall and driver losses). Therefore k_m , the spatial damping factor due to the sample under test can be written as

$$k_m = k_1 - k_{na} \quad (2.81)$$

Assuming the ratio $k_m/\omega_m \ll 1$, the surface impedance of the sample can be determined once ω_u , ω_l , ω_p , l , and c are measured.

3. Yaniv's Method

Equations have been developed in transmission line theory for determination of the input impedance of an electrical transmission line in terms of the line characteristics: propagation constant, characteristic impedance and length of line [Ref. 5]. When the line is terminated in an open or short circuit, the input impedance of the line may be expressed in terms of the line parameters with the following equations:

$$\tilde{z}_{os} = \tilde{z}_{char} \coth [\tilde{\gamma}L] \quad (2.82)$$

and

$$\tilde{z}_{ss} = \tilde{z}_{char} \tanh [\tilde{\gamma}L] \quad (2.83)$$

where \tilde{z}_{os} is the input impedance to a line terminated in an open circuit (Figure 2.4), \tilde{z}_{ss} is the input impedance to a line terminated in a short

circuit (Figure 2.5), \tilde{Z}_{char} is the characteristic impedance of the line, $\tilde{\gamma} \equiv \tilde{j}k$ is the complex propagation constant of the line and L is the length of the line.

From Eq. (2.82) and Eq. (2.83) we can solve for the material's characteristic impedance:

$$\tilde{Z}_{\text{char}} = [\tilde{Z}_{\text{ss}} \tilde{Z}_{\text{os}}]^{1/2}, \quad (2.84)$$

and for the complex propagation constant

$$\tanh[\tilde{\gamma}L] = [\tilde{Z}_{\text{ss}}/\tilde{Z}_{\text{os}}]^{1/2}. \quad (2.85)$$

The high-impedance termination for an acoustical line may be realized by termination with a rigid wall and a low-impedance termination for an acoustical line may be realized by terminating the line with a column of fluid equal to a quarter wavelength, itself terminated in a rigid wall [Ref. 5].

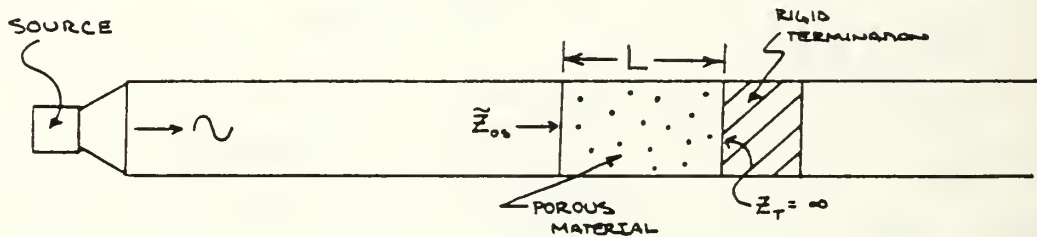


Figure 2.4 Geometry for Yaniv's Open Circuit Determination

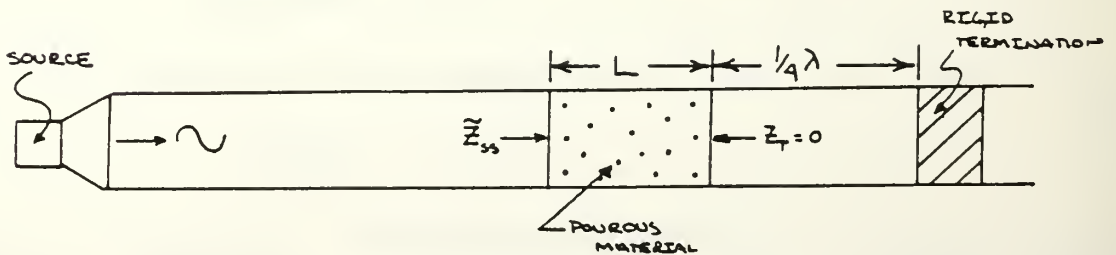


Figure 2.5 Geometry for Yaniv's Short Circuit Determination

By measuring the standing wave inside the tube alternatively terminated with an open circuit and then a short circuit, both \tilde{z}_{OS} and \tilde{z}_{SS} may be determined. With these two values, Eq. (2.84) and Eq. (2.85) may be solved for the desired complex propagation constant and characteristic impedance.

C. PROBE TUBE METHOD

This method was first presented by Scott (1946) [Ref. 2] to allow the determination of the complex wave number from the characteristics of an acoustic disturbance propagating through a fluid-saturated porous solid by probing the sound field existing in the material and extracting the wave number and absorption coefficient.

To determine the complex wave number in the porous medium, which describes the spatial variation of the acoustic disturbance for a uniform, progressive plane wave, Scott writes the velocity potential $\tilde{\phi}$ of the average motion in the pores as,

$$\tilde{\phi} = \phi_0 e^{-j\tilde{k}x} e^{j\omega t} \quad (2.86)$$

where $\tilde{k} \equiv k - ja$ is the complex wave number and x represents distance in the direction of propagation of the wave. Eq. (2.86) may be rearranged such that,

$$\tilde{\phi} = \phi_0 e^{-ax} e^{j(\omega t - kx)} \quad (2.87)$$

where a is the absorption coefficient and $k = 2\pi/\lambda$ is the wave number. Experimentally, one measures the acoustic pressure amplitude as a function of distance in the material, along with the wave length.

To determine the characteristic impedance of the porous material, Scott writes,

$$\tilde{z}_{\text{char}} = - \frac{\tilde{\rho}_{\text{eff}}(\omega) \omega}{\tilde{k}} \quad (2.88)$$

where $\rho_{\text{eff}}(\omega)$ is the complex frequency dependant effective density of the fluid in the pores. Determination of \tilde{z}_{char} assumes of course, that the effective fluid density is known, for example, from Biot theory. Eq. (2.88) was used only to check that the measured values of \tilde{k} were consistent with the values of \tilde{z}_{char} from the other methods. Only the values of \tilde{k} measured with Scott's method are reported here.

D. MATERIAL PROPERTIES METHOD

This method requires determination of five properties of the material to calculate the complex propagation constant and characteristic impedance of a material. Beranek [Ref. 4, Ch. 19] discusses this method in detail and only that portion of the theory applicable to the comparison with the new technique will be presented.

Beranek has shown that both the propagation constant and characteriustic impedance are derivable with the aid of charts from the basic physical properties of the material [Ref. 4, p. 839].

These properties are:

- (a) the specific flow resistance
- (b) the porosity
- (c) the structure factor
- (d) the volume coefficient of elasticity of the air in the interstices
- (e) the volime coefficient of elasticity of the skeleton of the material.

First, one must determine whether the material under investigation can be considered a soft blanket or a rigid/dense blanket. This determination is made by considering the ratio of the volume coefficient of elasticity of the

air in the interstices to that of the skeleton. If this ratio is less than $\frac{1}{20}$ the material is considered to be a rigid/dense blanket [Ref. 4, p. 840].

The fiberglass material chosen for the rigid/dense blanket criterion for Beranek provides an equation for the propagation constant $\tilde{b} = j\tilde{k}$, of such a material, namely

$$\tilde{b} = j\tilde{k} = j\omega \sqrt{\frac{\rho_0 k_{st} Y}{K}} \sqrt{1 - \frac{R_1}{\rho_0 k_{st} \omega}} , \quad (2.89)$$

where

\tilde{b} = complex propagation constant (same as Yaniv's $\tilde{\gamma}$),

\tilde{k} = complex wave number,

k_{st} = structure factor (same as Biot's tortuosity, α),

K = volume coefficient of elasticity of air in the interstices (i.e., the bulk modulus, and can be isothermal, adiabatic or complex),

R_1 = dynamic specific resistance per unit thickness (approximately the DC flow resistance),

ρ_0 = density of air, and

Y = porosity (same as P in Biot's theory).

By the use of Figure 2.6 and Figure 2.7 the magnitude and phase of \tilde{b} can be determined. The characteristic impedance may then be determined from

$$\tilde{Z}_{char} = -j \frac{K}{\omega Y} \tilde{b} . \quad (2.90)$$

This method suffers from the fact that not all of the material properties can be experimentally determined and thus reasonable assumptions for their values must be made [Ref. 4, p. 840].

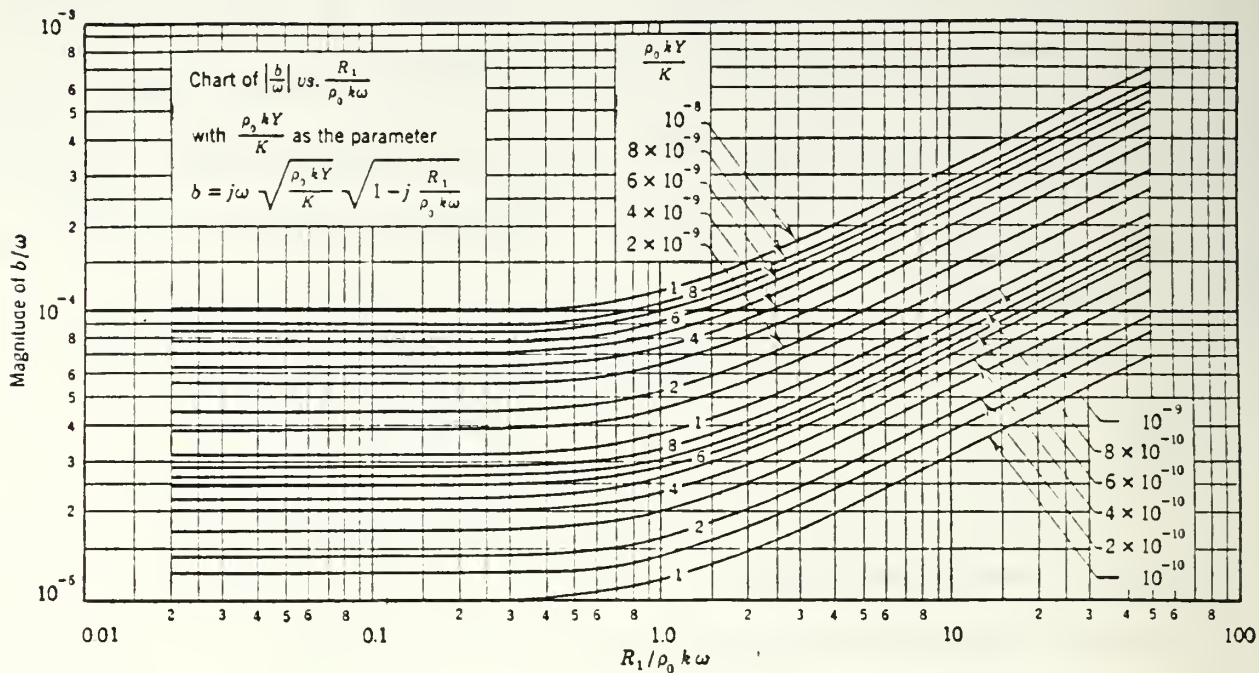


Figure 2.6 Chart for Determining the Magnitude of the Propagation Constant \tilde{b} of Rigid Tiles [Figure 19.3 of Ref. 4, p. 843]

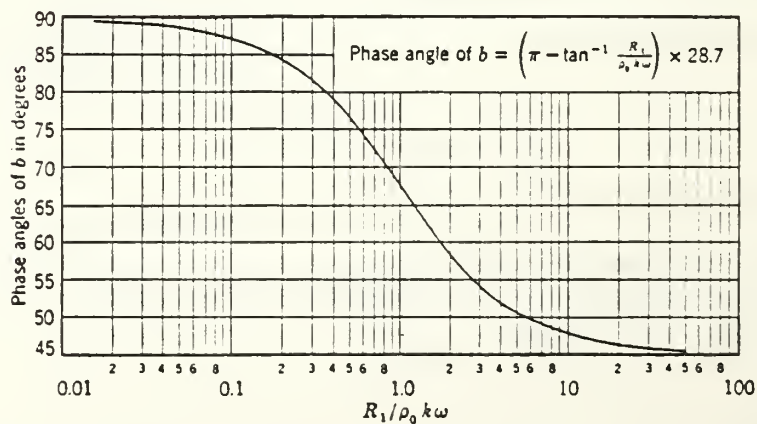


Figure 2.7 Chart for Determining the Phase Angle of the Propagation Constant \tilde{b} of Rigid Tiles [Figure 19.4 of Ref. 4, p. 844]

III. EXPERIMENT AND RESULTS

The objective of this study was to develop a new technique to measure both the complex wave number and characteristic impedance of a fluid-saturated porous solid. As with any new technique, comparison with classical methods is a good basis on which to judge one's theory. This section will first present the experimental results of the five classical techniques discussed previously, and then the new technique. A comparison of measured data for all methods will be presented in Chapter IV.

A. PROPERTIES OF THE POROUS SOLID

The porous solid used in all experiments was a semi-rigid type of fiberglass, much like Owens-Corning Tupe 705 fiberglass, used in the insulation of refrigeration type equipment. This material has sufficient rigidity to allow it to be cut from sheets into a variety of shapes and to allow it to be inserted into tubes without excessive compression. This property was important in the flow resistance and impedance tube measurements where a snug fit was required.

Discs with nominal dimensions 3-29/32 inches in diameter and 1-29/32 inches thick were cut from three sheets of this material, weighed, and measured to determine the material's volume. From two sets of measurements, the average material density was found to be $43.0 \pm 5.0 \text{ kg/m}^3$. For comparison, Owens-Corning Type 705 fiberglass is reported to have a density of 96 kg/m^3 [Ref. 5], while rock-wool, also known commercially as Stillite, is reported to have a density of 80 kg/m^3 [Ref. 2].

The porosity of the fiberglass material was measured by immersing a 1-inch cube in a graduated beaker of water and measuring the volume of displaced water. The fiberglass material itself was assumed to be non-absorbing. The resulting porosity was found to lie between 0.99 and 1.0.

1. Flow Resistance Measurements

Next, measurement was made of the specific DC flow resistance per unit length of sample. For most homogeneous, isotropic materials this flow resistance may be measured with sufficient accuracy by applying a known steady air flow across a sample and measuring the resulting pressure differential. The actual method used is similar to that presented by Beranek [Ref. 4, p. 850].

The quantities measured were: [Ref. 4, p. 847]

Δp = pressure differential between the two faces of the sample

v = velocity of the linear flow of air through the sample due to Δp

The pressure differential was measured with a standard water manometer (± 0.1 cm accuracy) and the velocity of linear flow was determined by measuring the time required to collect a sufficient volume of water (which drew air through the sample by a siphon) in a graduated cylinder. The experimental apparatus used is shown in Figure 3.1. All tube connections were sealed with RTV Silicon Rubber to prevent leaks.

The velocity of linear flow produced by Δp is,

$$v = \frac{V}{At} \quad , \quad (3.1)$$

where

V = volume of water collected in time t , and

A = cross-sectional area of sample.

Then the DC flow resistance R_{DC} is given by

$$R_{DC} = \frac{\Delta p}{vT} = \frac{\Delta p At}{VT} = \frac{\rho g \Delta h At}{VT} \quad , \quad (3.2)$$

where ρ is the density of water, g is the acceleration of gravity, Δh is the difference in water height in the two arms of the manometer, and T is the thickness of the sample. The units of R_{DC} are in Rayl/unit thickness, which can be written in CGS or MKS units $\text{gm/cm}^2 \cdot \text{sec/cm}$ or $\text{kg/m}^2 \cdot \text{sec/m}$, respectively.

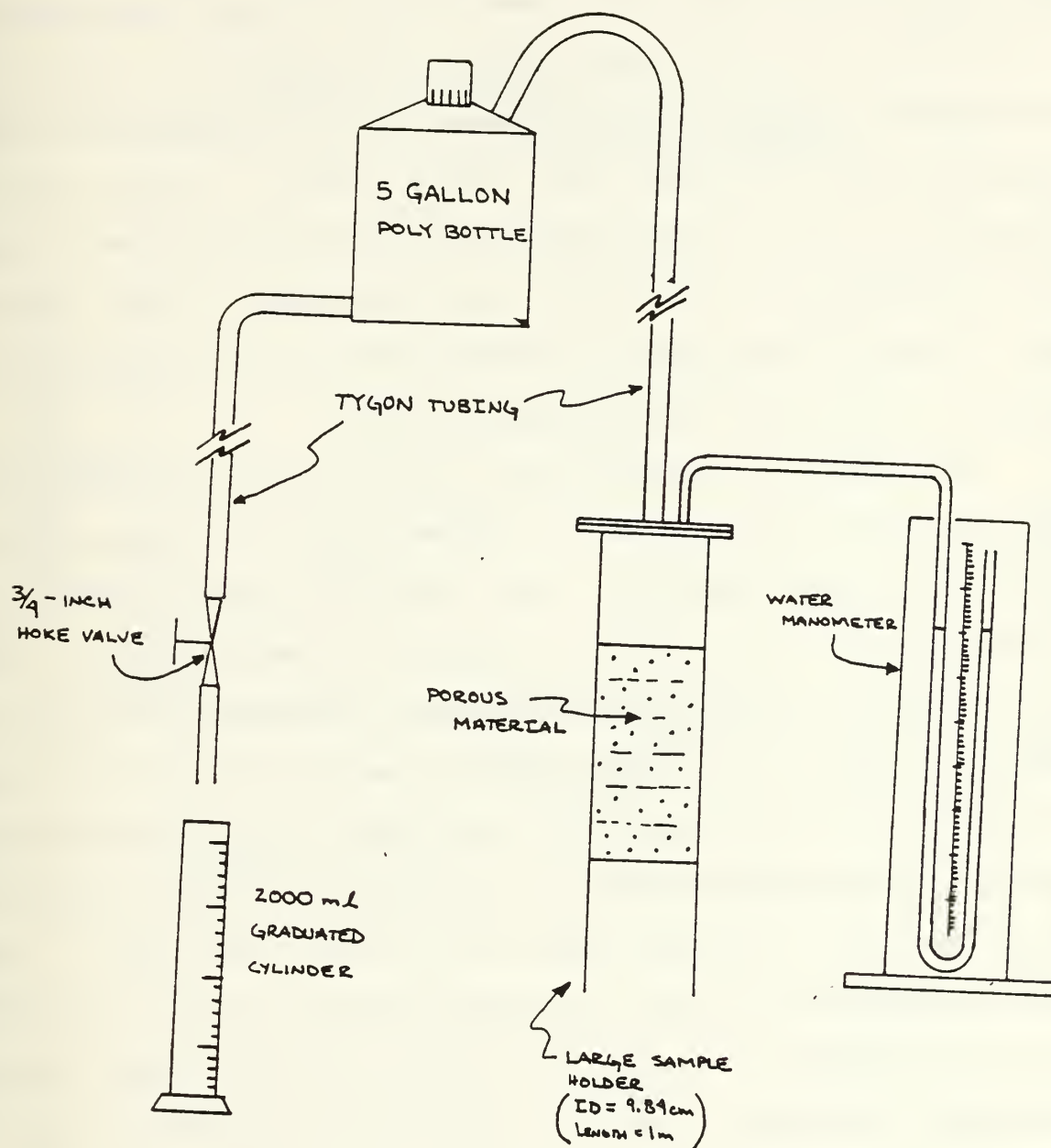


Figure 3.1 DC Flow Resistance Measurement Apparatus

In the first flow resistance experiment seven discs were placed into the large sample holder, each disc having a diameter of 9.85 cm and a thickness of 4.76 cm. The samples were made as close-fitting as possible but, unfortunately, the die used to cut these discs had a diameter approximately 0.1 cm greater than that of the sample holder. While providing a tight fit along the tube wall, this led to a compression in the material's thickness by approximately 10% as they were pushed into the holder. At that time it was thought that the effect of this compression would not be significant enough to require re-machining the cutting die. Later measurements of flow resistance using a different holder, however, gave values which were a factor of 2 smaller than that for flow normal to the fiberglass surface.

Measurements were conducted over a limited range of air flow velocity by adjusting the 3/4 inch Hoke valve on the water side of the apparatus to give the desired pressure differential. When steady state conditions were reached, the volume flow was then plotted as a function of volume flow rate. This is shown in Figure 3.2. Within experimental error, the variation in Δp with \dot{V} was found to be linear up to the highest flow rate measured, which was many orders of magnitude greater than expected for a sound wave. Since the sound pressures appearing at the surface of a sample are seldom greater than 1000 dynes/cm² in practice (100 Pa or 0.5 inches water) it can be seen that even at higher pressure differentials the linear relationship between Δp and \dot{V} is maintained. The DC flow resistance had a value of $59,100 \pm 4,200$ MKS Rayl/m using the uncompressed thickness. Table 2 lists the experimental data and Table 3 lists the DC flow resistance results using the compressed and uncompressed thickness.

It was discovered later (while attempting to reconcile these measurements with the DC flow resistance required to fit the resonance data) that the DC flow resistance of our fiberglass samples is quite anisotropic (the

DC flow resistance required to fit the [100] modes resonances, which has its particle velocity parallel to the air-fiberglass surface, was between 10,000 to 20,000 MKS Rayl/m).

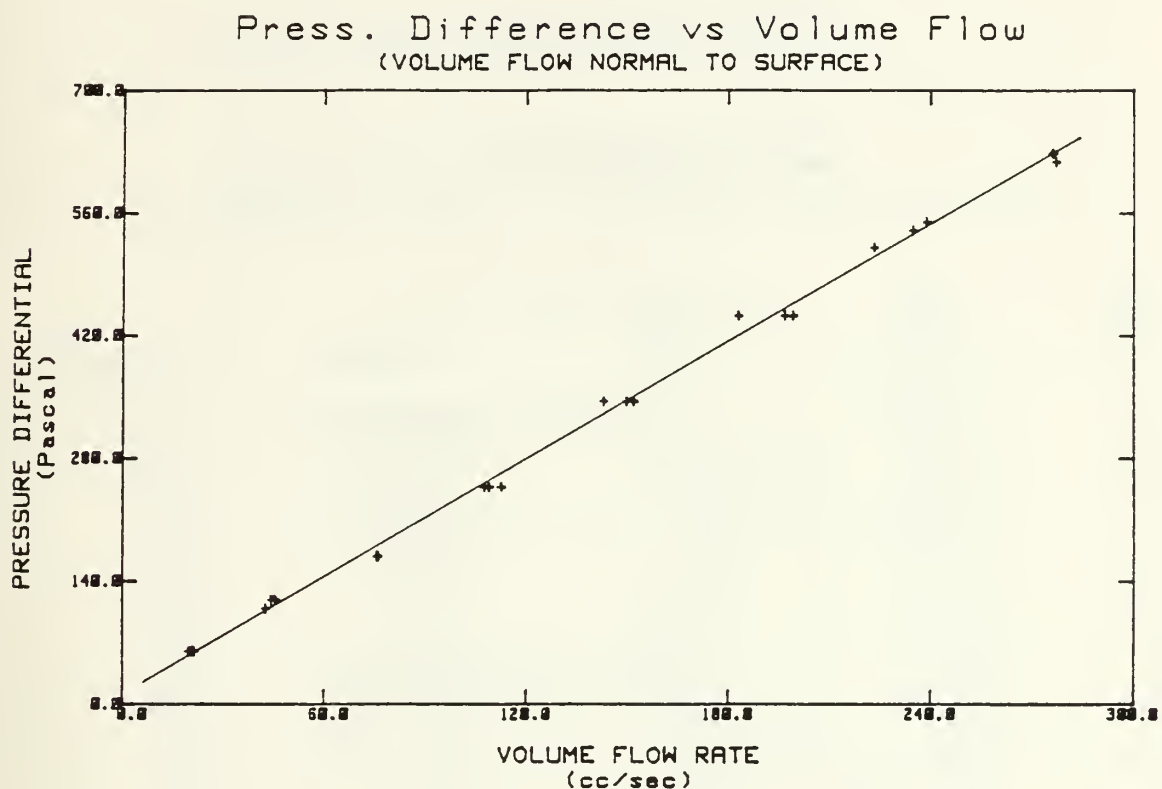


Figure 3.2 Δp vs \dot{V} in the Large Sample Holder

TABLE 2

LARGE SAMPLE HOLDER DC FLOW RESISTANCE MEASUREMENT DATA

(Flow Normal to Surface)

Uncompressed thickness = 33.34 ± 0.1 cmCompressed thickness = 29.80 ± 0.1 cmSample holder diameter = 9.84 ± 0.1 cm

Room temperature = 23.3 deg. Centigrade

Δh (cc)	Vol. (cc)	t (sec)	\dot{V} (cc/sec)	R_{DC}^* (MKS Rayl/m)
6.4 ± 0.1	2038 ± 4	7.3 ± 0.1	278.0 ± 0.5	$57.5 \times 10^3 \pm 700$
6.4	2102	7.6	277.7	57.6
6.3	2074	7.4	278.8	56.5
5.6	2016	8.4	240.6	58.2
5.5	2056	8.7	236.6	58.1
5.3	2008	8.9	225.1	58.8
4.5	2046	10.3	198.6	56.6
4.5	2122	10.6	201.1	55.9
4.3	2108	11.4	184.9	60.8
3.5	2128	14.1	151.5	57.7
3.5	2063	14.3	144.7	60.4
3.5	2074	13.5	153.6	56.9
2.5	2077	18.1	114.6	54.5
2.5	2062	18.8	109.5	57.1
2.5	2103	19.0	110.9	56.3
1.7	2098	27.0	77.9	54.5
1.7	2081	26.8	77.6	54.8
1.7	2072	26.7	77.5	54.8
1.1	2086	46.9	44.4	61.8
1.2	2120	46.0	46.1	65.1
1.2	2100	44.3	47.4	63.3
0.6	2110	98.5	21.4	70.0
0.6	2116	94.4	22.4	66.8
0.6	2161	93.3	23.2	64.7

*Compressed Thickness Data

TABLE 3

LARGE SAMPLE HOLDER DC FLOW RESISTANCE MEASUREMENT RESULTS

(flow normal to surface)

Compressed Thickness:

Mean $R_{DC} = 59.1 \times 10^3$ MKS Rayl/m

Std. Deviation = 4.2×10^3 MKS Rayl/m

Uncompressed Thickness:

Mean $R_{DC} = 53.2 \times 10^3$ MKS Rayl/m

Std. Deviation = 4.2×10^3 MKS Rayl/m

A smaller sample holder was subsequently constructed and samples were cut which allowed the measurement of flow resistance with particle velocity normal to the fiberglass surface and with particle velocity parallel to the fiberglass surface. Figure 3.3 shows the results.

Not only is the DC flow resistance anisotropic by a factor of two to three but the effect of the 10% compression of the material in the large sample holder is evident. The resulting flow resistance parallel to the surface of the material was found to be $15,200 \pm 500$ MKS Rayl/m while that normal to the surface was $34,000 \pm 900$ MKS Rayl/m. Table 4 and Table 5 give the measured data.

2. Viscous-Inertial Transition Frequency

The ratio of the viscous penetration depth to the characteristic pore size is one of the most fundamental dimensionless parameters that determines the nature of elastic wave propagation in a fluid-saturated porous solid. If $\delta_{\text{visc}} \ll \text{pore size}$, then the motion of the fluid in the pores is essentially the same as if the fluid were inviscid. However, if $\delta_{\text{visc}} \gg \text{pore size}$ then the fluid in the pores is essentially frozen to the solid, and sound cannot propagate within the fluid. Microscopic photographs of the fiberglass material provided an estimate of the average distance between fibers. This mean distance was determined to be $220 \pm 80 \mu\text{m}$. The crossover from where fluid inertia dominates to where flow resistance dominates occurs when $\delta_{\text{visc}} \approx 1/2$ (mean pore diameter). This value was estimated to be $110 \pm 40 \mu\text{m}$. Since, the thermal penetration depth in air is approximately the same as the viscous penetration depth, the crossover from isothermal to adiabatic compression in the pores was expected to be nearly coincident with the viscous-inertial transition. Figure 3.4 shows the viscous penetration depth over the frequencies of interest. The transition frequency for this case was

approximately 400 Hz. For a collection of straight pipes of radius a , the DC flow resistance is given by,

$$R_{DC} = \frac{8\eta}{a^2} \quad (3.3)$$

Considering the DC flow resistance measured with flow parallel to the air-fiberglass surface, the equivalent radius would be 98 μm . This figure compares very well with the microscopic observations. A radius of 98 μm results in a transition frequency of 500 Hz.

3. CLASSIC METHODS OF TRANSMISSION LINE THEORY

1. Impedance Tube Experiment and Results

The impedance tube technique is the most widely used to determine a material's characteristic impedance, being relatively simple in both theory and measurement. This experiment was the first conducted of the five classical methods.

A Bruel and Kjaer Type 4002 Standing Wave apparatus was used for these measurements. The tube was constructed of clear plexiglass which allowed visual inspection of the sample. The tube is 1 meter in length and 9.8 cm in diameter. This sets a lower limit on the usable frequency range to be approximately 85 Hz for the length of the tube to be greater than 1/4 wavelength, and a higher limit of approximately 2006 Hz for operation below the lowest crossmode, thus ensuring only plane waves are propagated. the HP4192A Low Frequency Impedance Analyzer was used for signal generation and detection. It has a built in frequency synthesizer with a resolution of 1 mHz and a phase-sensitive detector with a 0.1 Hz bandwidth to preclude noise and harmonics interfering with measurements. Figure 3.5 shows the experimental setup. Since we are primarily interested in the lowest longitudinal mode in the rectangular cavity (particle velocity parallel to the surface of the fiberglass), which has a frequency in the range of 600 to 700 Hz, the impedance

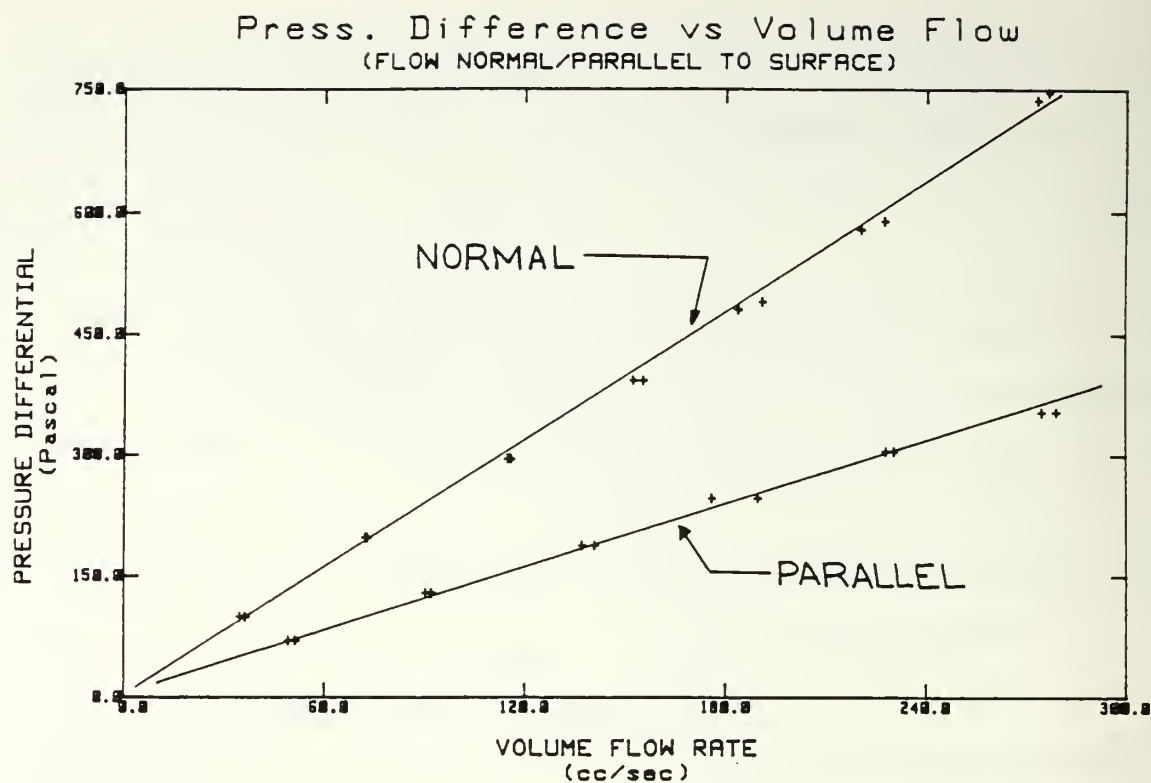


Figure 3.3 Δp vs \dot{V} in the Small Sample Holder

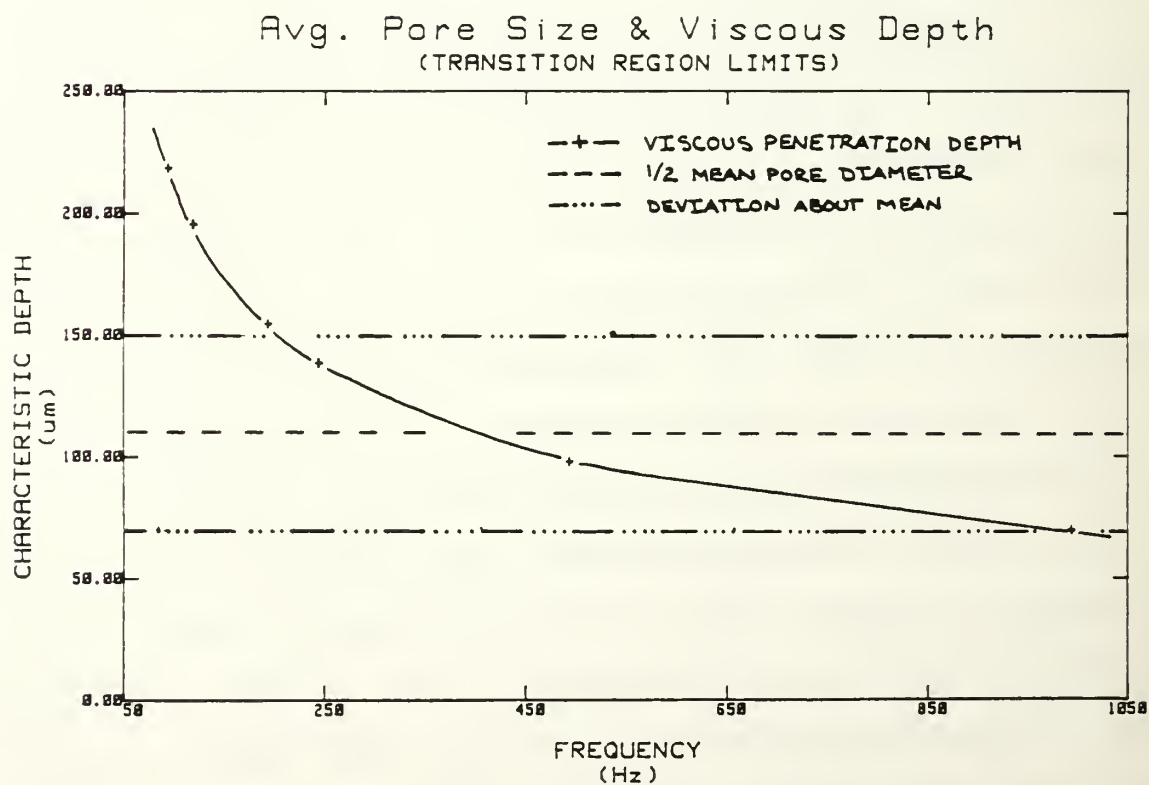


Figure 3.4 Characteristic Length Scale of a Pore Compared to the Viscous Penetration Depth

TABLE 4

SMALL SAMPLE HOLDER DC FLOW RESISTANCE MEASUREMENT DATA AND RESULTS
(Flow Normal to Surface)

Thickness = 15.60 ± 0.01 cm
Cross-Sectional Area = 20.5 ± 0.1 cm²

Δh (cc)	Vol. (cc)	t (sec)	V (cc/sec)	R_{DC} (MKS Rayl/m)
7.6 ± 0.1	2165 ± 4	7.8 ± 0.1	278.6 ± 0.5	$35.1 \times 10^3 \pm 900$
7.5	2086	7.6	275.2	35.1
6.0	2052	9.0	229.3	33.7
5.9	2096	9.4	222.3	34.2
4.9	2082	11.2	185.6	34.0
5.0	2108	10.9	192.9	33.4
4.0	2084	13.5	154.3	33.4
4.0	2116	13.4	157.4	32.7
3.0	2150	18.3	117.6	32.9
3.0	2098	18.0	116.6	33.2
2.0	2118	28.4	74.6	34.6
2.0	2151	29.1	74.0	34.8
1.0	2116	57.8	36.6	35.2
1.0	2121	55.4	38.3	33.7

Mean $R_{DC} = 34.0 \times 10^3$ MKS Rayl/m
Std Deviation = 0.9×10^3 MKS Rayl/m

TABLE 5

SMALL SAMPLE HOLDER DC FLOW RESISTANCE MEASUREMENT DATA AND RESULTS
(Flow Parallel to Surface)Thickness = 17.80 ± 0.01 cmCross-Sectional Area = 20.5 ± 0.1 cm²

Δh (cc)	Vol. (cc)	t (sec)	V (cc/sec)	R_{DC} (MKS Rayl/m)
3.6 ± 0.1	2068 ± 4	7.5 ± 0.1	276.8 ± 0.5	$14.7 \times 10^3 \pm 500$
3.6	2100	7.5	281.1	14.4
3.1	2066	9.0	229.8	15.2
3.1	2120	9.1	232.2	15.1
2.5	2109	11.9	177.7	15.9
2.5	2124	11.1	191.5	14.7
1.9	2126	14.9	142.8	15.0
1.9	2115	15.2	139.0	15.4
1.3	2075	22.1	94.0	15.6
1.3	2108	22.9	92.0	15.9
0.7	2150	42.2	51.0	15.5
0.7	2104	39.6	53.3	14.9

Mean $R_{DC} = 15.2 \times 10^3$ MKS Rayl/m
 Std. Deviation = 0.5×10^3 MKS Rayl/m

tube measurements were carried out at frequencies between 100-1000 Hz with sample thicknesses of 4, 8, and 12 inches. The different sample thicknesses were used in order to determine how thick the material had to be for reflections from the rigid termination to be negligible, thus allowing the material's characteristic impedance to be determined.

Measurements of the reflection coefficient from 100 to 1000 Hz for all three samples indicated that the material could be considered infinite for thicknesses greater than 8 to 12 inches. The reflection coefficient, R , is given by

$$R = |B/A| , \quad (3.4)$$

where the ratio B/A is given by Eq. (2.68). The reflection coefficient changes noticeably in the frequency region between 400 and 500 Hz. This is thought to be due to the transition from isothermal to adiabatic compression of the gas in the pores.

The standing wave ratio and the distance to the first pressure node were measured for the 12" sample at frequencies between 100 and 1000 Hz. The normalized characteristic impedance $|\tilde{Z}_{\text{char}}|/\rho_0 c$ was calculated using the "Smith" chart nomogram with the SWR and phase at the first node as input parameters. Table 6 gives the results.

It was observed that at frequencies below 200 Hz fluctuations occur in both magnitude and phase of the impedance. The position and the amplitude of the pressure antinode and node were very difficult to measure accurately below 200 Hz, and so these data are not as reliable as the data taken above 200 Hz. From 200 to 400 Hz, the impedance magnitude decreases at a larger rate than at frequencies above 500 Hz, apparent evidence of the isothermal to adiabatic transition occurring in the pores. This transition is seen in both magnitude and phase as well as the reflection coefficient. The transition coincides

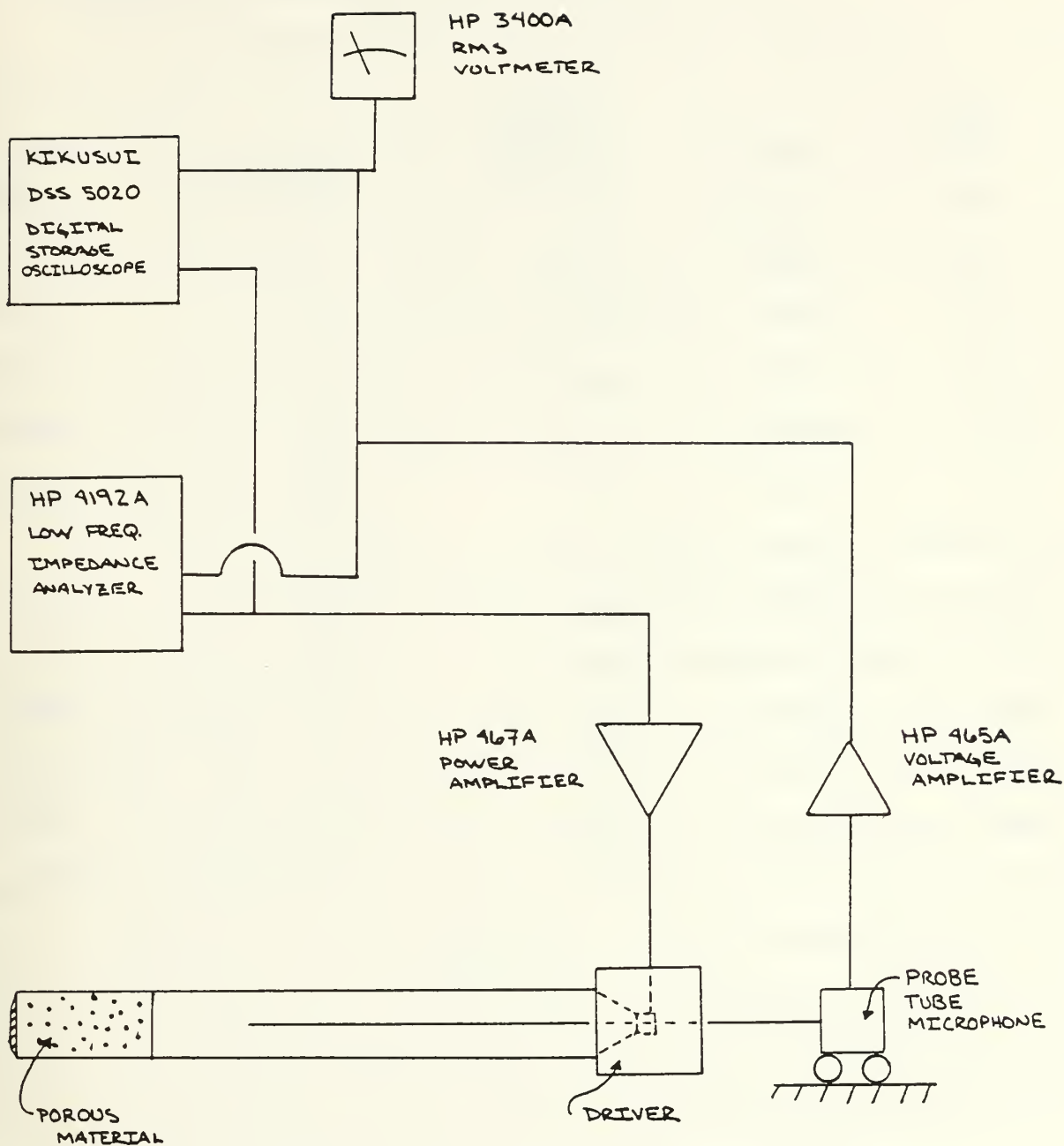


Figure 3.5 Experimental Setup for the Impedance Tube Method

TABLE 6

IMPEDANCE TUBE MEASUREMENT RESULTS ON 12" OF FIBERGLASS

<u>Freq. (Hz)</u>	<u>SWR</u>	<u>Distance to first node(cm)</u>	<u>$\tilde{z}_{\text{char}} /\rho_0 c$</u>	<u>$\phi_{z_{\text{char}}}$ (Degrees)</u>
100	2.79	59.70	1.60	-44.0
125	5.83	59.70	3.74	-48.0
200	4.79	36.80	2.64	-52.7
250	4.40	28.75	2.87	-45.6
300	4.00	24.10	2.83	-42.1
400	3.46	18.00	2.60	-38.0
500	2.23	14.45	1.95	-22.9
600	2.47	11.40	1.94	-31.7
700	2.26	9.65	1.80	-29.3
800	2.30	8.25	1.75	-31.7
900	2.15	7.75	1.81	-24.4
1000	2.11	6.90	1.77	-25.1

with the velocity profile changing from laminar flow in the low frequency limit to plug flow in the high frequency limit (see Figure 2.1).

2. Resonance Analysis Experiment and Results

Of all the classic methods, this technique is most similar to the new technique in that parameters are extracted from the resonance curve to determine a sample's characteristic impedance. As previously commented, this method is limited to discrete frequencies and thin samples since the resonances of the tube become weaker as thicker samples are introduced. The upper limit thickness for our fiberglass was found to be about 2 inches. A 1 inch thick sample was chosen since Yaniv's method was conducted with the same sample thickness and since three of the five empty tube resonances were still distinct enough to make measurements.

The experimental setup is very similar to the impedance tube experiment. A Bruel and Kjaer Type 4002 Standing Wave apparatus was used along with a HP3580A Spectrum Analyzer. The spectrum analyzer was used to determine the resonance frequencies and half-power widths of the lowest three peaks in both the empty tube and in the tube filled with the 1 inch thick fiberglass sample. A HP3314A Function Generator was then set to the frequency of each of these peak and the distance between the fiberglass surface and the pressure maximum closest to the speaker was measured. This is needed to calculate the effective tube length, as an infinite impedance loudspeaker is assumed in the theory. The surface impedance of the sample was then determined from these measurements using Eq. (2.78). Figure 3.6 shows the experimental setup and Table 7 gives the resulting values of normalized impedance values.

The lowest two resonances (center frequencies of 253 Hz and 400 Hz, respectively) gave plausible values of surface impedance, however the highest mode with the absorbing material present (center frequency of 538 - 544 Hz) had

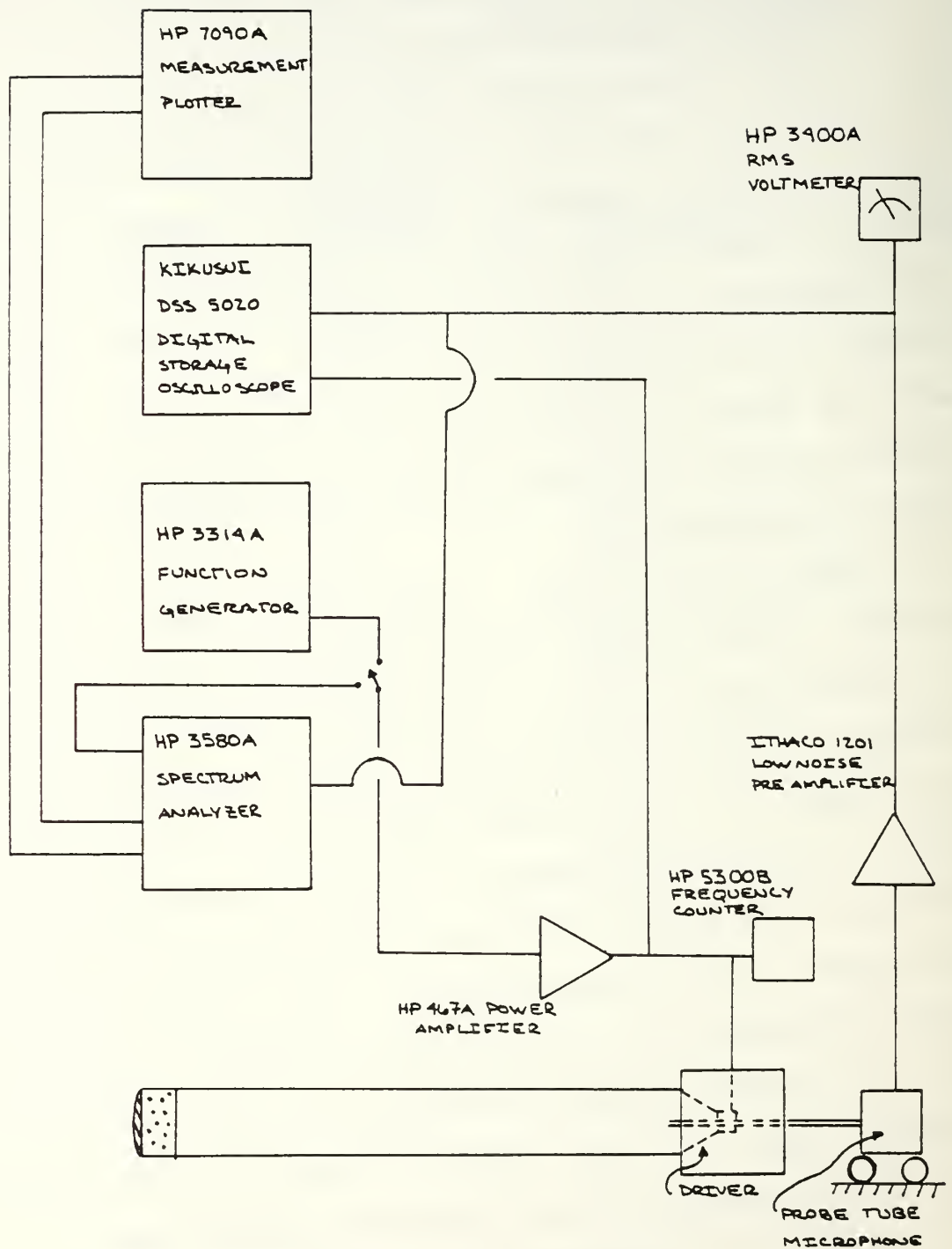


Figure 3.6 Equipment Setup For Resonance Analysis Method

TABLE 7

RESONANCE ANALYSIS SURFACE IMPEDANCE RESULTS
 (Impedance Tube and Rectangular Cavity)
 (1 Inch Thick Fiberglass Sample)

Surface Impedance Results in Impedance Tube

<u>Resonance Peak Number</u>	<u>Center Frequency (damped) (Hz)</u>	<u>HPFW (Hz)</u>	<u>$\tilde{z}_{\text{surf}} /\rho_0 c$</u>	<u>$\phi_{z_{\text{surf}}}$ (degrees)</u>	<u>k_m/ω_m</u>
1	253	23	2.9	-85.9	0.0078
2	400	18	2.1	-88.9	0.0013
3*	543	41	7.7	+66.4	-0.0055

Surface Impedance Results in Rectangular Cavity

<u>Resonance Peak Number</u>	<u>Center Frequency (damped) (Hz)</u>	<u>HPFW (Hz)</u>	<u>$\tilde{z}_{\text{surf}} /\rho_0 c$</u>	<u>$\phi_{z_{\text{surf}}}$ (degrees)</u>	<u>k_m/ω_m</u>
1	841	126	1.8	-65.4	0.071

* This point was discarded, as discussed in text.

a higher Q than in the empty tube and was therefore discarded. The erroneous data for the third resonance peak is attributed to the significant broadening of its resonance curve and the resultant overlapping with adjacent modes.

This resonance analysis method was applied to the rectangular cavity with and without a 1 inch thick strip of fiberglass while exciting the [010] mode to verify the results obtained in the tube. The [010] mode was chosen because for this mode the particle velocity is normal to the fiberglass surface, as in the impedance tube. For these measurements in the rectangular cavity the source was placed at grid point (0,0) (Figure 3.11) and the receiver at grid point (20,0). The resonance curve was first measured in the empty cavity; it had a center frequency of 873 Hz. The normalized magnitude of the surface impedance obtained agreed closely with the value obtained by the impedance tube for frequencies between 800 and 900 Hz. However a significant phase discrepancy was evident. The reason for the discrepancy is not known. Perhaps it is a result of using a point source located in a corner. Table 7 lists the results.

As with other impedance tube measurements, this method relies upon a plane propagating wave, where incidence on the porous material is assumed normal to the surface of the sample under test. With a point source located in one corner of the cavity used, departure from plane wave propagation can be expected with increasing sample thickness as the quality factor of the resonance degrades. The extracted impedances are surface values. In both geometries in which this method was used the magnitude of the surface impedance decreased with increasing frequency (which was expected). The phase in all measurements indicates that the impedance remains largely reactive, and that the gas in the pores acts like a stiffness. Use of samples of greater thickness would only suppress the resonance curves more.

3. Yaniv's Method, Experiment and Results

The third and last technique which uses transmission line theory is the method proposed and experimentally verified by Yaniv [Ref. 5]. The experiment was conducted using the impedance tube of the previous two experiments, with several modifications. Yaniv's method requires measuring the surface impedance with the sample backed by a rigid termination and by an acoustic short-circuit, obtained by moving the rigid termination such that a $1/4 \lambda$ air gap exists between the rear surface of the material and the rigid termination.

The rigid end cap used in the two previous experiments was replaced with a 2 inch thick disc of plexiglass with a 3/8 inch diameter hollow aluminum tube threaded into the side away from the driver. A small amount of high vacuum grease was used to seal the edges of the disc at the tube walls while still allowing for positioning. The front face of the disc had a recess cut out of it into which a FET microphone mounted at the end of a 3/16 inch hollow aluminum rod could fit snugly and flush so as to provide a smooth surface when the disc was placed against the back end of the sample. The 3/16 inch diameter rod fit inside the 3/8 inch diameter rod, providing support and allowing the microphone to be positioned anywhere between the backside of the porous solid and the rigid termination. Electrical connection to a power supply switchbox was also made by wires which passed through the small hollow rod. This configuration allowed the disc and microphone to serve as the rigid termination for the open circuit impedance measurement and also allowed accurate positioning of the termination to provide the required one-quarter wavelength air gap between the porous solid and the rigid termination at each frequency. Figure 3.7 shows the movable termination and Figure 3.8 shows the equipment set setup.

A 1 inch thick disc of fiberglass was inserted into the impedance tube such that the distance between the driver and the sample was at least a quarter

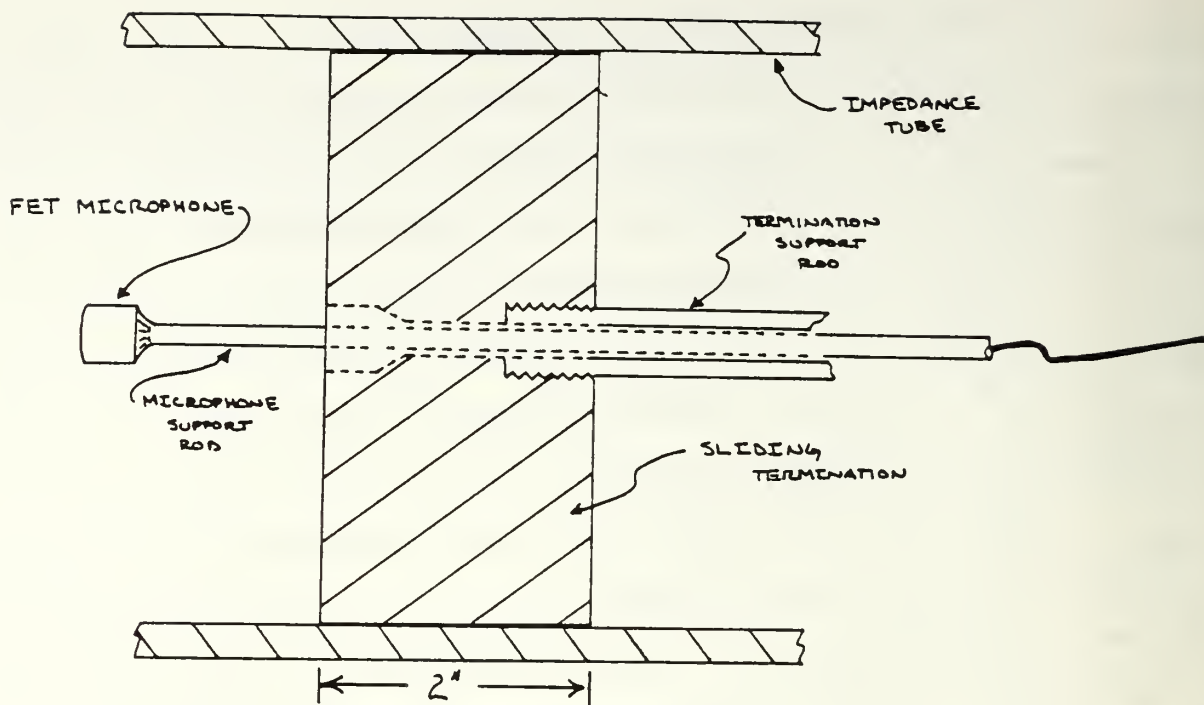


Figure 3.7 The Rigid Sliding Termination (Yaniv's Method)

wavelength. The lowest usable frequency was therefore approximately 250 Hz, the upper limit remaining approximately 2000 Hz to preclude the lowest crossmode. Measurements were made of the first minimum and maximum pressure amplitudes in front of the sample and of the distance between the sample surface and the first pressure minimum in front of the sample. For each frequency, these measurements were performed under conditions of open and short circuit terminations. A short circuit termination at the back side of the fiberglass disc was obtained by adjusting the position of the plexiglass plug until a null output was observed from the microphone, which was held flush to the fiberglass disc. It was found that, within experimental error, the resulting distance between the porous disc and the plexiglass plug was within 1% of the $1/4$ wavelength determination made in the empty tube at the frequencies used in the experiment. The standing wave ratio and the reflection coefficient phase angle were calculated using Eq. (2.67) and Eq. (2.70), respectively. The

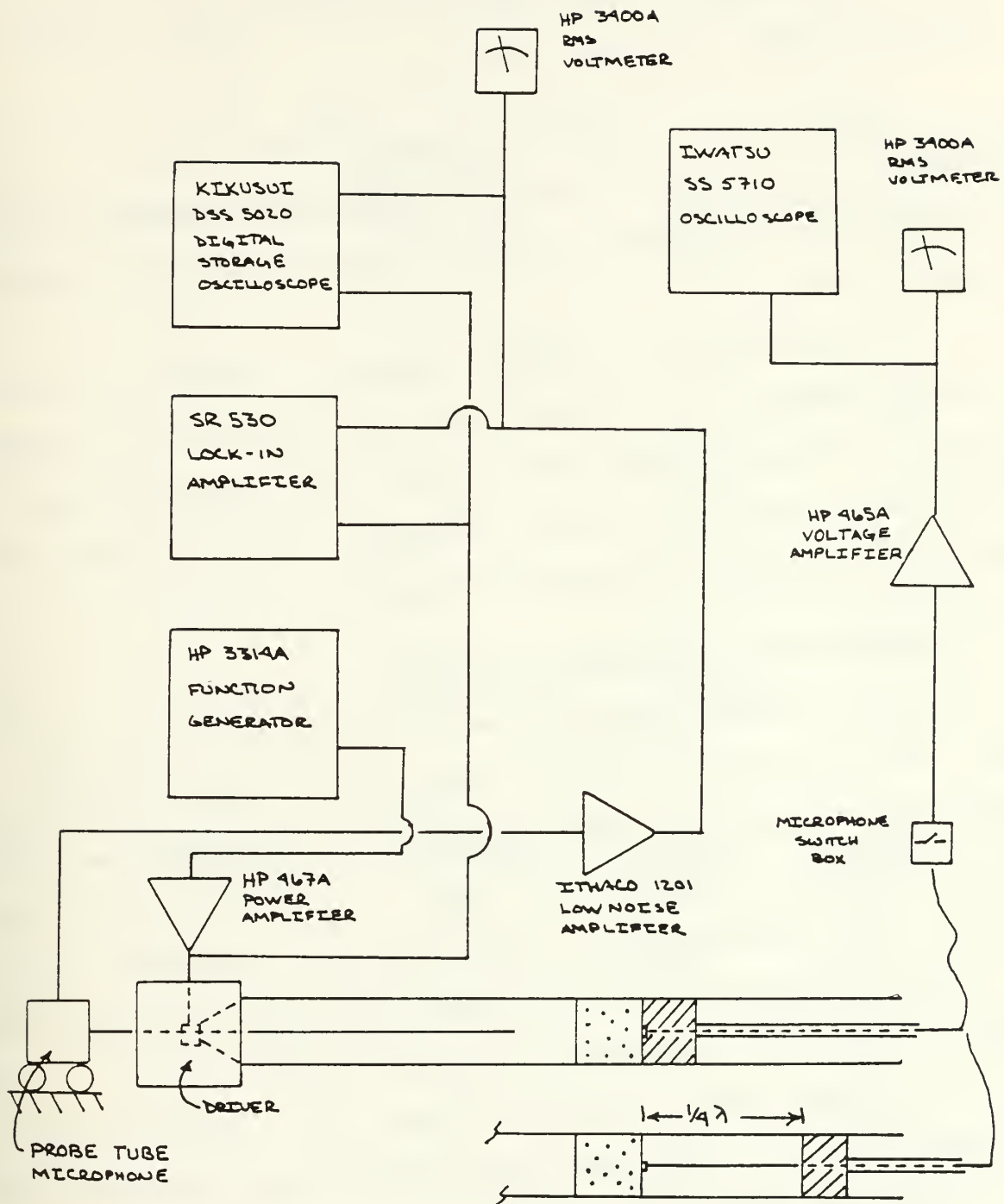


Figure 3.8 Equipment Setup for Yaniv's Method

open and short circuit impedances were found using the "Smith" chart. The characteristic impedance was then found by use of Eq. (2.84).

Determination of the complex propagation constant, $\tilde{\gamma} \equiv j\tilde{k}$, required finding the roots of Eq. (2.85) such that,

$$\tanh[\tilde{\gamma}L] - [\tilde{Z}_{SS}/\tilde{Z}_{OS}]^{1/2} = 0 \quad . \quad (3.5)$$

The roots were found using a numerical technique known as Ward's method. The details are given in Appendix A [Ref. 19]. The results of this experiment are listed in Table 8.

As for the previous methods, a decrease in impedance magnitude with increasing frequency was observed, with the transition from isothermal to adiabatic compression between 400 to 700 Hz in this 1 inch thick sample. The complex wave number also shows this transition. The data and results for 400 Hz appear to anomalous. The reason is not known.

C. PROBE TUBE METHOD, EXPERIMENT AND RESULTS

The probe tube measurements were made by setting up a plane wave in the Bruel and Kjaer Type 4002 Standing Wave apparatus filled partially with fiberglass and exploring the sound field by means of a probe tube extension to the impedance tube microphone. The slope of the decay of the pressure amplitude with distance provided a measurement of the attenuation constant α . The change in phase of the oscillatory wave with distance provided the wave number k . The complex wave number is then found from $\tilde{k} \equiv k - j\alpha$.

The equipment setup is shown in Figure 3.9. Three specimens, of thickness 4, 8, and 12 inches, were chosen for measurement and comparison with the impedance tube results. Each sample thickness was made up of the required number of fiberglass discs, 9.84 cm diameter and 4.76 cm thick, inserted into the tube opposite the driver, taking care to avoid compression of each disc

TABLE 8

YANIV'S METHOD EXPERIMENTAL RESULTS

Freq. (Hz)	\tilde{z}_{os}		\tilde{z}_{ss}		
	SWR	Distance to first node (cm)	SWR	Distance to first node (cm)	
250	50.40	30.90	1.36	30.50	
300	42.40	25.80	1.33	25.70	
400	24.03	18.60	1.89	33.20	
500	24.71	14.10	1.68	21.70	
600	12.29	11.50	1.65	17.20	
700	9.57	9.70	1.56	14.70	
800	8.71	8.20	1.70	12.60	
900	7.16	6.80	1.70	11.15	
1000	6.42	5.90	1.67	10.45	

Freq. (Hz)	$ \tilde{z}_{char} /\rho_0 c$	$\phi_{z_{char}}$ (degrees)	k (Rad/m)	a (Np/m)	c_{ph} (m/s)
250	2.79	-44.8	12.82	13.96	122.5
300	2.78	-43.6	12.56	13.86	150.2
400	2.04	-22.3	15.17	8.80	165.7
500	2.17	-30.1	20.82	12.75	150.9
600	2.10	-28.9	21.70	15.77	173.7
700	1.98	-28.4	21.73	16.81	202.2
800	1.94	-27.9	24.88	17.50	202.1
900	1.75	-27.7	27.75	18.40	203.7
1000	1.62	-25.6	28.41	17.92	221.2

while trying to minimize any air gaps between disc surfaces. Each disc had a 0.71 cm diameter hole cut in the center for a close fit around the probe tube without any deformation of the fiberglass.

The probe tube was manufactured out of steel tubing with the same outside and inside diameter of the existing open ended probe tube on the standing wave apparatus. A copper cap was welded onto the end of the extension next to a 3/16 inch diameter hole to allow the measurement of the sound field. The extension attached to the existing probe tube with a plastic sleeve. This is shown in Figure 3.10.

The experiment was conducted at frequencies of 125, 250, 500, and 1000 Hz for each of the three sample thicknesses, but only the 12 inch thick sample was long enough so that the wave reflected from the rigid end of the tube was sufficiently attenuated to be negligible compared to the incident wave. The pressure amplitude at the rigid termination was measured to be 20 dB less than that at the sample boundary. Determination of the attenuation constant was made by plotting pressure versus distance on semi-log paper and extracting the slope. The phase of the pressure was measured with a SR-350 Dual Channel Lock-In Amplifier. The wave number was determined from the change of phase with distance into the fiberglass. Table 9 displays the experimental results in terms of k and a .

The impedance magnitude decreases with frequency while the phase indicates that the material becomes more resistive with increasing frequency. Only the absorption coefficient shows any sign of the transition between isothermal and adiabatic compressions in the pore volume.

D. MATERIAL PROPERTY METHOD, EXPERIMENT AND RESULTS

All the methods discussed so far involve measuring certain characteristics of a progressive plane wave in the porous material or its proximity. Beranek

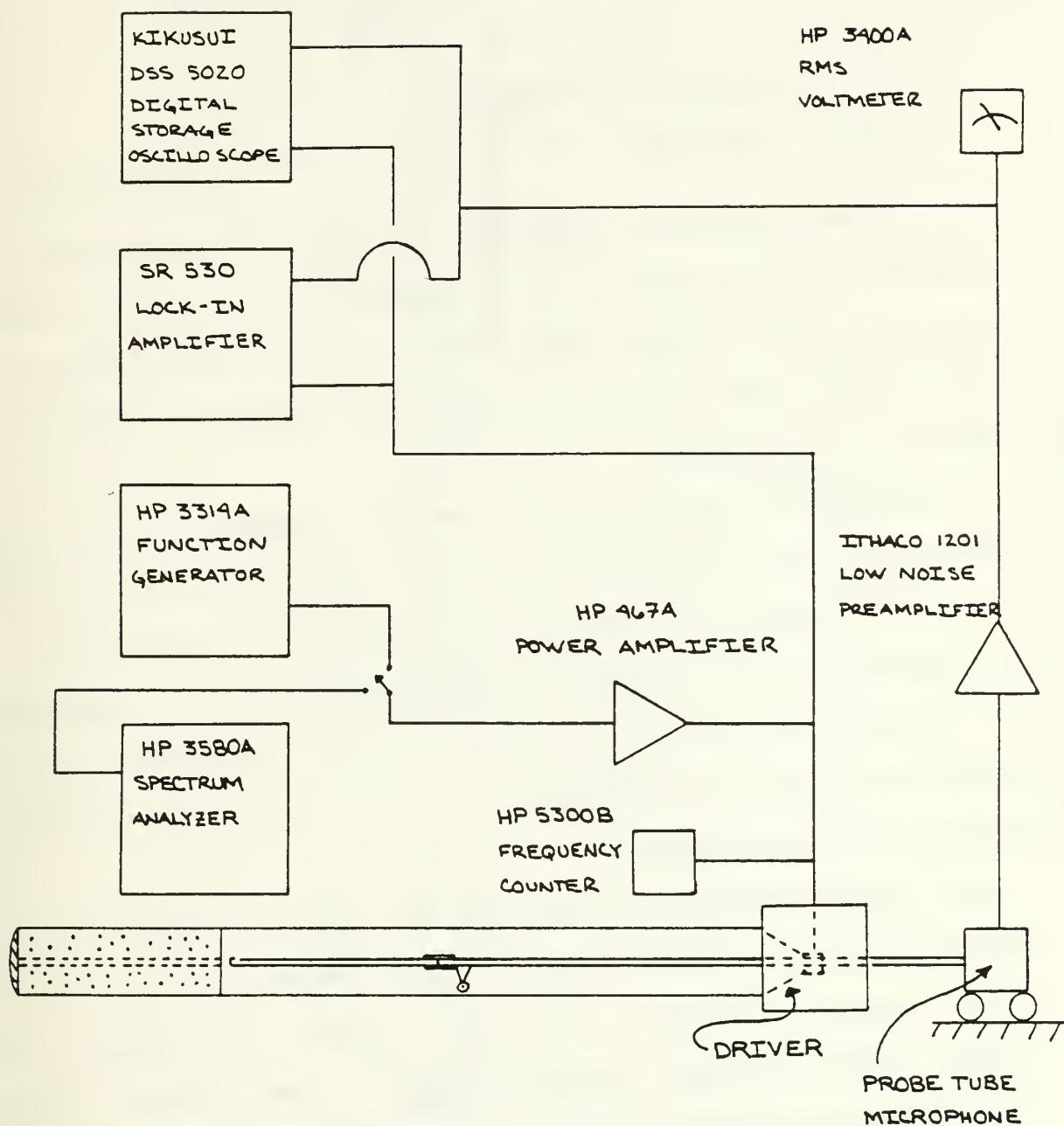


Figure 3.9 Equipment Setup for Probe Tube Experiment

has shown that the complex wave number and characteristic impedance can also be derived from the basic physical properties of the material with the aid of charts. These properties are:

- a) specific flow resistance per unit length, $R_1 (\approx R_{DC})$
- b) porosity, γ
- c) structure factor, k_{st} (tortuosity)
- d) volume coefficient of elasticity of air in the interstices K (Bulk modulus)
- e) volume coefficient of elasticity of the skeleton of the material.

Measurements of the specific flow resistance and porosity have already been discussed. The remaining three material properties are difficult if not impossible to measure, and will, based on a reasonable knowledge of the material, be approximated.

The structure factor k_{st} , known as the tortuosity in Biot theory, is essentially a path length correction factor. Experimentally, it is found to depend most strongly on the porosity of the porous solid [Ref. 11]. In the limit porosity = 1, the tortuosity also equals 1 for typical porous materials, and certainly for fiberglass. As the porosity of the samples used in this research was found to be very close to 1, a value of 1 for the tortuosity was assumed in all calculations.

The volume coefficient of elasticity of air in the interstices, K , is an important term; if isothermal conditions can be assumed then $K \approx 1 \times 10^6$ dynes/cm²; if adiabatic conditions exist then $K \approx 1.4 \times 10^6$ dynes/cm². For most fibrous acoustic materials however, K will, in some frequency region, be neither isothermal nor adiabatic but will be something in between and will be complex valued and frequency dependent, as is our case.

Finally, the volume coefficient of elasticity of the skeleton, K_{skel} , although not directly involved in the calculation of \tilde{k} and \tilde{z}_{char} , must be known or approximated since it is the ratio of K/K_{skel} that determined whether

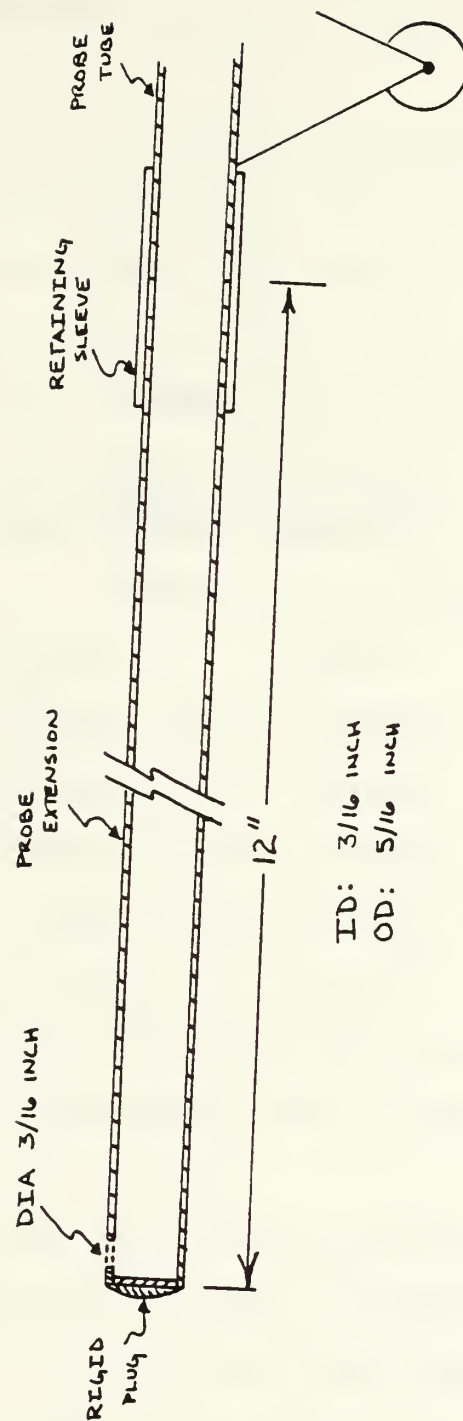


Figure 3.10 Probe Tube Extension

TABLE 9

PROBE TUBE EXPERIMENTAL RESULTS
12" Thick Fiberglass Sample)

<u>Freq</u> <u>(Hz)</u>	<u>k</u> <u>(Rad/m)</u>	<u>a</u> <u>(Np/m)</u>	<u>c_{ph}</u> <u>(m/s)</u>
125	14.8	13.6	53.1
250	20.9	16.3	75.2
500	29.7	22.7	105.8
1000	43.3	21.7	145.1

a material is treated as a soft blanket or a rigid/dense blanket. Based on the appearance, texture, and high flow resistivity of the fiberglass it was assumed that the material should be treated as a rigid/dense blanket. [Ref. 4, pp. 839-840]

Once the properties of the material were characterized, Eq. (2.89) could be used to directly calculate or Figure 2.6 and Figure 2.7 used to graphically determine the magnitude and phase of the complex propagation constant $\tilde{b} \equiv j\tilde{k}$ as a function of frequency, from which the complex wave number is determined. Once these were determined the characteristic impedance could be calculated by use of Eq. (2.90). The values determined from the graphs for \tilde{k} and the calculated values of \tilde{Z}_{char} assuming isothermal conditions in the pore volume are listed in Table 10. The same quantities, assuming adiabatic conditions, are listed in Table 11.

As expected, the impedance magnitude decreases with increasing frequency. The impedance phase calculated for both isothermal and adiabatic conditions is the same, a consequence of the bulk modulus being a real quantity in the two limiting cases. If isothermal conditions were to exist, then the impedance phase would approach an angle of -45 degrees (pure diffusion of sound pressure). Since the calculated phase values remain nearer to the diffusive limit, the assumption that isothermal conditions exist in the pore volume would be most nearly correct.

Over the frequency range considered, the isothermal values for k and a are greater than the adiabatic values, which is consistent with the fact that the isothermal sound speed is less than the adiabatic sound speed.

E. THE NEW TECHNIQUE, EXPERIMENT AND RESULTS

The plane wave resonator chosen to conduct all experiments was constructed out of plexiglass with interior dimensions as follows:

Length (x-direction) = 25.4 ± 0.1 cm

Width (y-direction) = 19.8 ± 0.1 cm

Height (z-direction) = 7.3 ± 0.1 cm.

This particular cavity was constructed for a laboratory experiment on standing waves in a rectangular room. The minimum wall thickness was 1.27 cm (1/2"). The cavity was mounted on three legs with the source hole located in the floor at one corner to allow the excitation of all modes. The top cover of the cavity is removable to allow insertion of fiberglass samples. When installed, the top cover seals the cavity and slides to allow the receiver position to be varied. A small microphone receptacle mounted on a slidebar installed in the removable cover allows the pressure to be measured throughout the cavity with a probe tube. All sliding surfaces were constructed with very close tolerances and coated with high vacuum grease to reduce leakage and to provide a tight fit when the cavity cover was installed.

The receiver slide bar assembly consisted of three portions: the slide bar, the microphone receptacle, and the receiver microphone. The slide bar fit into a groove machined into the interior surface of the top cover and fit flush with this surface. A threaded hole was cut into the slidebar to allow mounting the microphone receptacle. The microphone receptacle consisted of a hollow aluminum cylinder with a thumb screw to set and hold the height of a brass probe tube assembly. The probe tube assembly allowed insertion of a General Radio precision microphone flush with the smaller bore probe tube extension which could be inserted into the cavity interior without disrupting the sound field.

The bottom of the cavity was marked with grid lines, 21 in the length direction, 15 in the width direction, spaced 1/2" apart, producing 336 individual grid points. The in-phase and quadrature components of pressure

TABLE 10

MATERIAL PROPERTIES METHOD RESULTS
 (Isothermal Conditions)
 ($R_{DC} = 15,000$ MKS Rayl/m)

Freq. (Hz)	$ \tilde{z}_{char} /\rho_0 c$	$\phi_{z_{char}}$ (degrees)	k (Rad/m)	a (Np/m)	c_{ph} (m/s)
100	3.66	-43.5	6.83	6.48	92.0
125	3.17	-43.0	7.47	6.96	105.1
200	2.64	-42.0	10.08	9.08	124.7
250	2.32	-41.5	11.17	9.89	140.6
300	2.12	-41.0	12.33	10.72	152.9
400	1.83	-39.0	14.66	11.82	171.4
500	1.66	-37.5	16.94	13.00	185.5
600	1.49	-37.0	18.37	13.84	205.2
700	1.40	-35.0	21.26	14.88	206.9
800	1.32	-33.5	22.63	14.98	222.1
900	1.24	-32.0	24.46	15.28	231.2
1000	1.20	-31.0	26.38	15.85	238.2

TABLE 11

MATERIAL PROPERTIES METHOD RESULTS
 (Adiabatic Conditions)
 ($R_{DC} = 15,000$ MKS Rayl/m)

<u>Freq. (Hz)</u>	<u>$\tilde{z}_{char} /\rho_0 c$</u>	<u>$\phi_{z_{char}}$ (degrees)</u>	<u>k (Rad/m)</u>	<u>α (Np/m)</u>	<u>c_{ph} (m/s)</u>
100	4.28	-43.5	5.69	5.40	110.4
125	3.93	-43.0	6.60	6.16	119.0
200	3.04	-42.0	8.31	7.48	151.2
250	2.70	-41.5	9.29	8.22	169.1
300	2.39	-41.0	9.96	8.65	189.3
400	2.09	-39.0	11.91	9.65	211.0
500	1.88	-37.5	13.71	10.52	229.1
600	1.71	-37.0	15.05	11.34	250.5
700	1.68	-35.0	17.65	12.36	249.2
800	1.54	-33.5	18.86	12.48	266.5
900	1.44	-32.0	20.14	12.59	280.8
1000	1.39	-31.0	21.82	13.11	287.9

were measured at each grid point for the mode and sample selected. Figure 3.11 shows the location of the source and the grid numbering scheme that was applied to the interior floor of the cavity.

Ten fiberglass samples were cut from a fiberglass sheet, with thicknesses ranging from 0.48 cm (3/16 inch) to 4.76 cm (1 7/8 inch) the maximum thickness being equal to the full thickness of the sheet. The samples were cut in the form of rectangular strips so as to fit snugly along the side wall opposite the source. Figure 3.11 shows the location. The strips extended from grid point (0,15) to grid point (20,15). The samples were cut such that the surface normal to the flow velocity in the original flow resistance experiment would also be normal to the particle velocity expected when the [010] mode was excited (i.e., the "width" direction in Figure 3.11) and parallel to the particle velocity when the [100] mode was excited (the "length" direction). Table 12 lists the samples used and their thicknesses.

Three experiments were conducted:

1. The mode structure in the cavity was measured over the frequency range of interest for each sample. The effect of introducing the fiberglass samples on the strength and shape of the resonances was noted. Of particular interest were the [100] and [010] modes, which were expected to be relatively distinct.
 2. The DC flow resistance of the air-filled fiberglass was then extracted from the above measurements using the dispersion relation developed in Chapter 2 for the allowed modes (Eq. (2.51)), following which the complex wave number and characteristic impedance were calculated.
 3. The pressure field of the [100] and [010] modes was measured for varying sample thicknesses and compared to that predicted by theory.
- The equipment setup used to conduct all three of these experiments is shown in Figure 3.12.

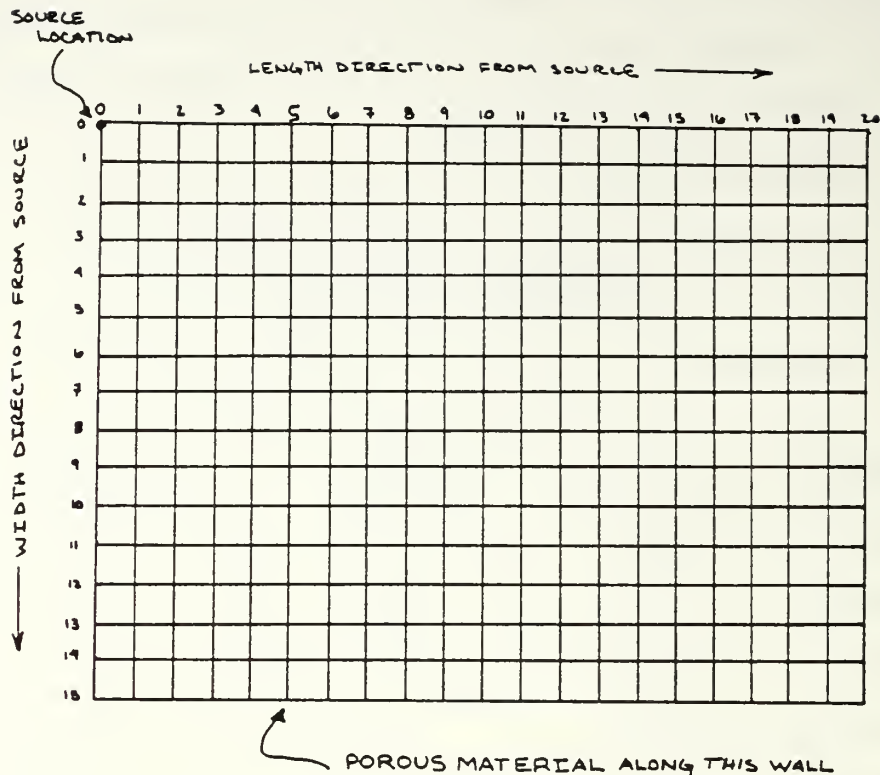


Figure 3.11 Rectangular Cavity Grid Map

1. Modal Frequencies Up to 2000 Hz for Various Fiberglass Thicknesses

The first of the three experiments was conducted to determine the modes present in the empty cavity and the effects of increasing sample thickness on the shape and strength of each resonant mode. From mode theory, seven modes were expected to exist in the empty cavity for frequencies less than 2000 Hz. Of these seven modes, the two lowest were the [100] and [010] modes, both of which occur below 1000 Hz. All seven modes were observed, with the two lowest modes being strong and relatively distinct compared to the others. This is shown in Figure 3.13. Table 13 lists the theoretically calculated and experimentally measured peak frequencies of the modes present in the cavity up to 2000 Hz.

There was some concern that as thicker samples were introduced the resonance peaks would overlap, making the measurement of the half-power widths unreliable. This condition set the upper limit on usable sample thickness to $1\frac{7}{8}$ " for the [100] mode (sample #10) and $1\frac{11}{16}$ " for the [010] mode (sample #5).

For all observed modes, the center frequency down-shifted as the sample thickness was increased, while the Q decreased. The [100] mode has an empty cavity peak frequency and Q of 680.2 Hz and 147.9, respectively. Inserting the $1\frac{7}{8}$ " (sample #10) fiberglass strip down-shifted its center frequency and lowered the Q to 570.0 Hz and 3.2, respectively, for a total frequency change of 110.2 Hz. The [010] mode has a center frequency of 870.2 Hz and a Q of 57.6 in the empty cavity, but when the $1\frac{11}{16}$ " (sample #5) fiberglass strip was inserted the peak frequency only down-shifted 17 Hz to 853.2 Hz with a Q of 21.1. For both mode measurements the receiver probe tube remained flush with the ceiling of the cavity at grid point (20,0). See Figures 3.14 and 3.15

Several observations from this experiment were made:

- (1) The Q and the center frequency of both modes decreased with increasing sample thickness.
- (2) Compared to the [010] mode, the [100] mode, with particle velocity parallel to the fiberglass surface, allowed thicker samples to be introduced before the resonance curve spread such that the Q could no longer be reliably determined.
- (3) For all sample thicknesses, the Q of the resonance curves was larger with the receiver positioned above the source (grid point (0,0)) than in the opposite corner (grid point (20,0)). This was assumed to be due to near field effects of the source on the receiver.

Consequently, only the resonance data taken with the receiver at grid point (20,0) is reported here.

TABLE 12

FIBERGLASS SAMPLE THICKNESS

<u>Sample #</u>	<u>Thickness (inches)</u>	<u>Thickness (cm)</u>
1	$3/16 \pm 1/32$	0.48 ± 0.01
2	$1/4$	0.64
3	$3/8$	0.95
4	$1/2$	1.27
5	$11/16$	1.75
6	$7/8$	2.22
7	1	2.54
8	$1 \ 1/4$	3.18
9	$1 \ 1/2$	3.81
10	$1 \ 7/8$	4.76

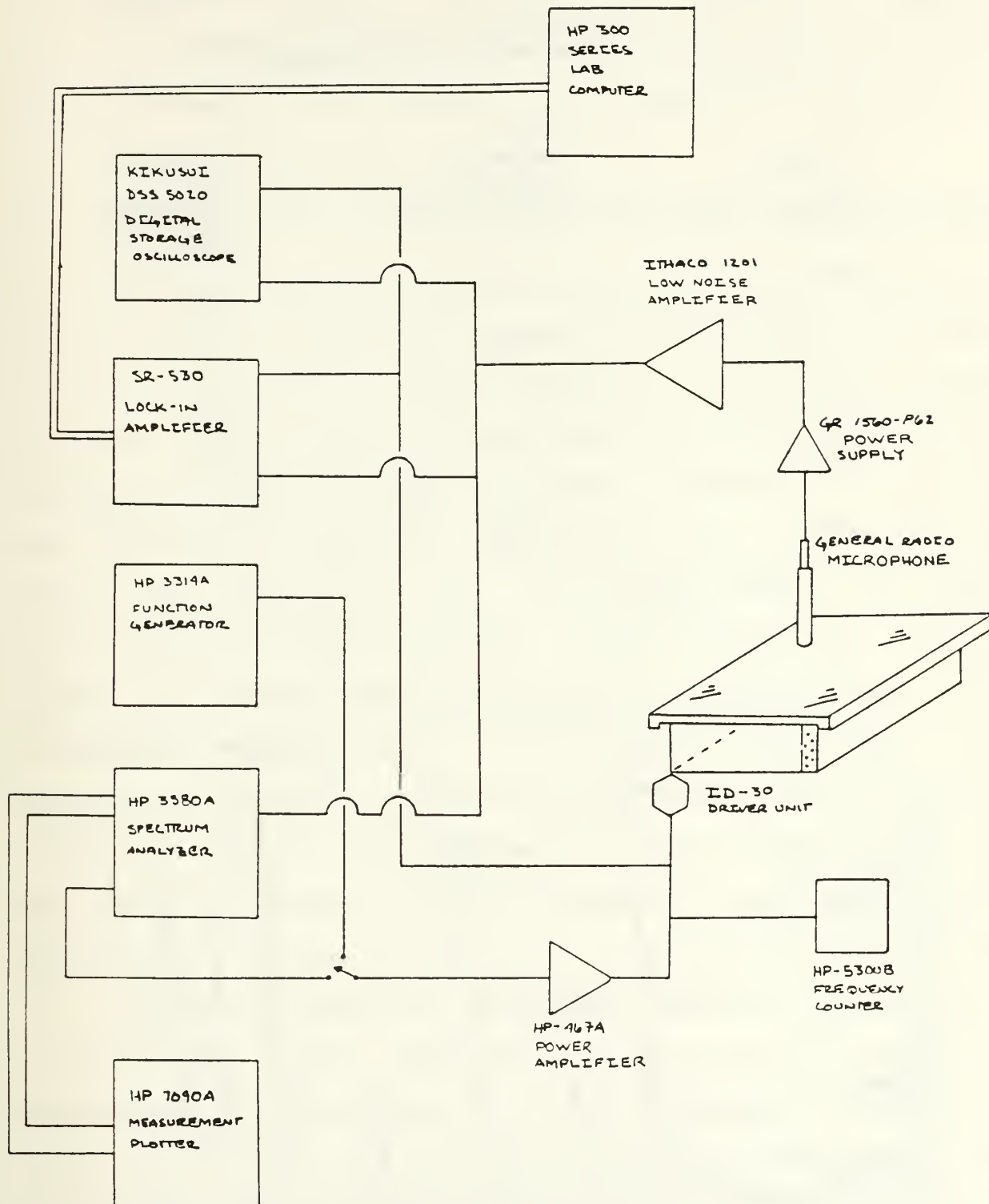


Figure 3.12 Experimental Setup for the New Method

TABLE 13

RESONANCE MODES OF THE EMPTY CAVITY
(Theoretical and Measured)

<u>Mode #</u>	<u>Resonant Frequency (calculated)</u>	<u>Resonant Frequency (measured)</u>
100	679 ± 4	676 ± 1
010	871 ± 5	868
110	1105 ± 9	1099
200	1358 ± 12	1354
210	1614 ± 14	1608
020	1742 ± 19	1738
120	1870 ± 23	1865

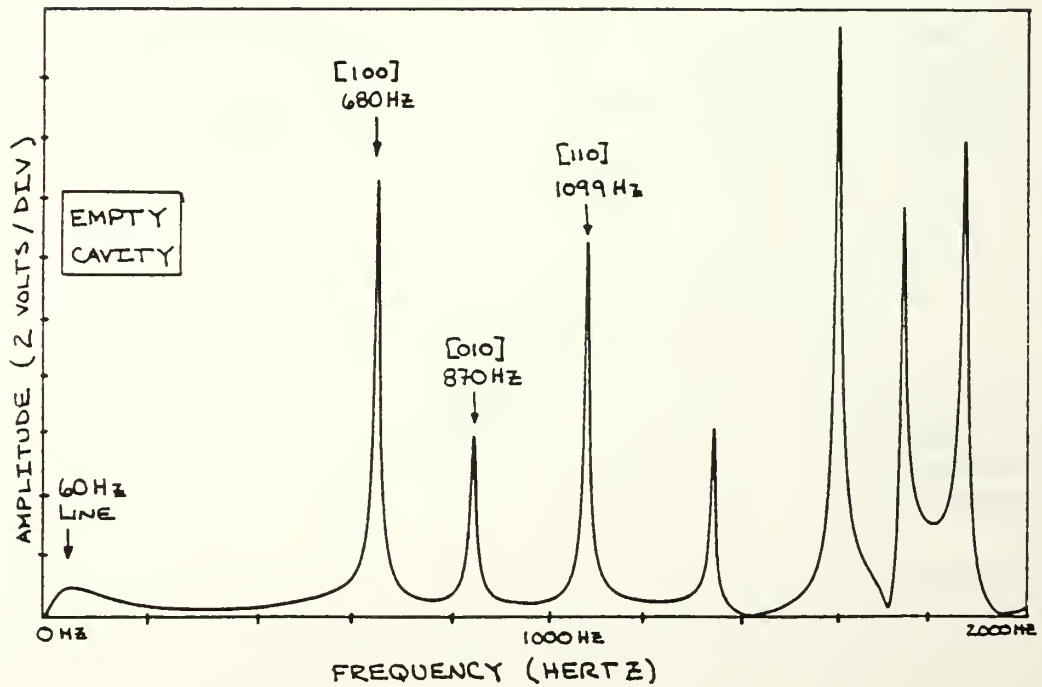


Figure 3.13 Mode Structure of the Empty Cavity

(4) Overlap of the [110] mode with the [010] mode was evident for fiberglass thickness of 1/2" (sample #4) and greater. Overlap of the [100] mode with the [010] mode was not significant until a thickness of 1 1/4" (sample #8) of fiberglass was introduced. See Figures 3.14 and 3.15.

2. Measured f_c and Q of the [100] and [010] Modes for Various Fiberglass Thicknesses

The second experiment consisted of measuring the center frequency and Q of the [100] and [010] modes as a function of sample thickness. The receiver was placed in the ceiling of the cavity at grid point (20,0) at the opposite end of the long wall from the source. This location was chosen to minimize direct acoustic cross-talk between the source and receiver. For the [100] mode, each of the 10 samples was inserted and the center frequency and Q were measured from the resonance curve. This sample procedure was repeated for the [010] mode except only samples 1 through 5 were used. The center frequency and half-power frequencies were measured to within a tenth of a Hertz by reading the frequency of the 1 to 1.5 MHz Local Oscillator output of the HP3580A Spectrum Analyzer on a HP5300B Frequency Counter. Setting the scale to 1 dB/div on the Spectrum Analyzer allowed the center frequency and half-power full width of the resonance curves to be measured. Tables 14 and 15 list the experimentally determined values of f_c and Q for the [100] and [010] modes.

Following the experimental measurements, theoretical values of f_c and Q for the [100] and [010] modes as a function of sample thickness were calculated from the complex roots of the dispersion relation (Eq. (2.51)) for various values of DC flow resistance using a numerical analysis technique known as Ward's method [Ref. 19, pp. 169-170]. A brief description of this method is given in Appendix A. However, before a comparison between theory and

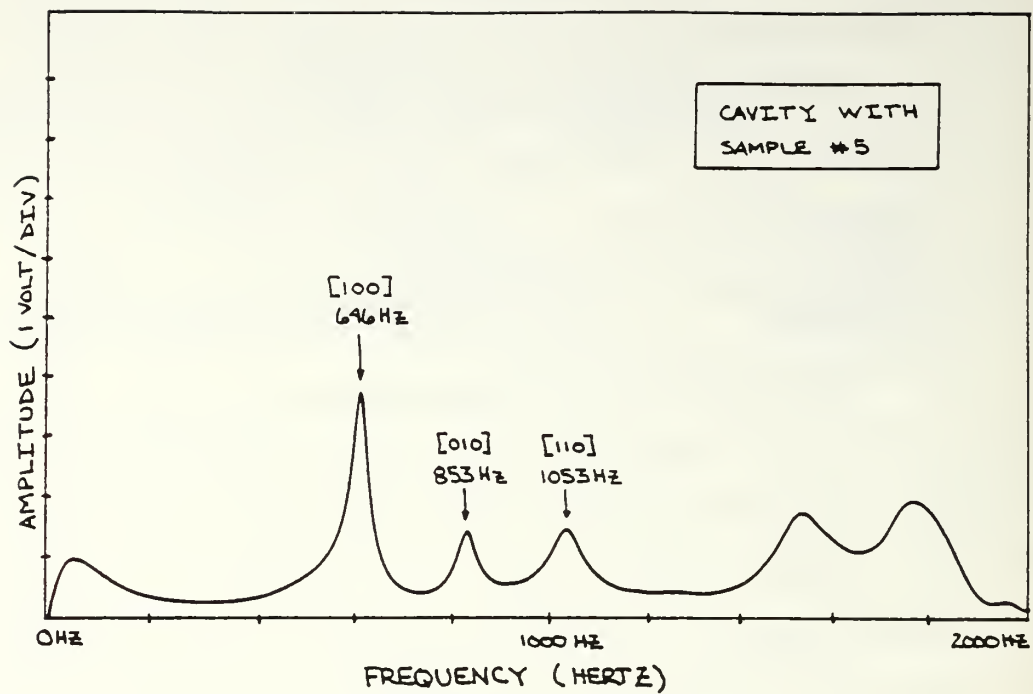


Figure 3.14 Mode Structure of Cavity With a 11/16" Fiberglass Strip (sample #5)

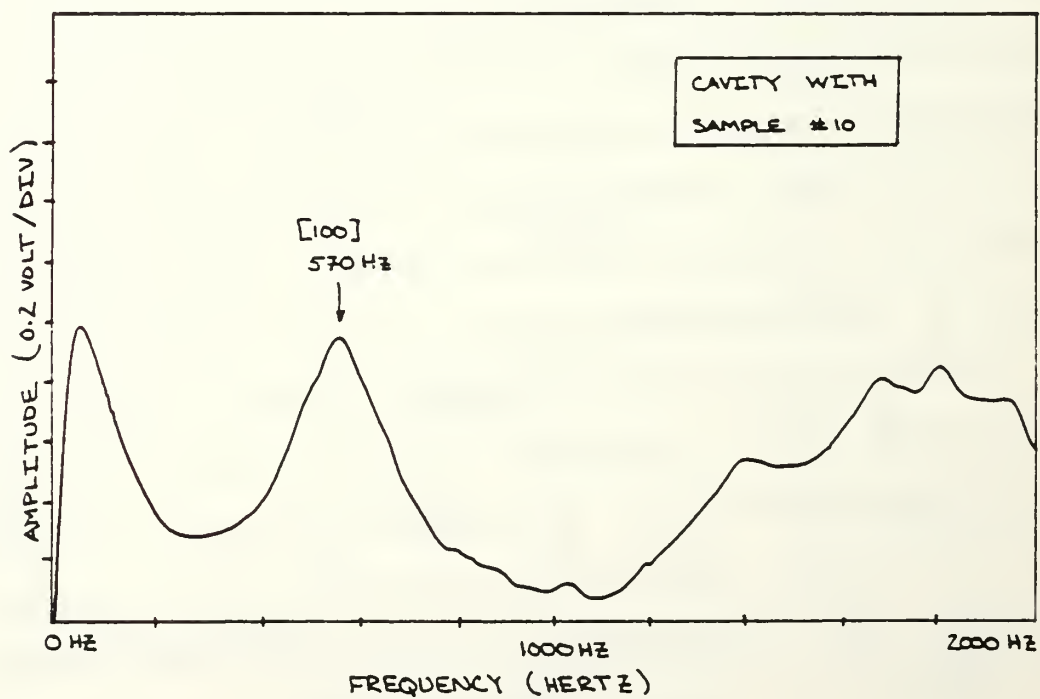


Figure 3.15 Mode Structure of the Cavity With 1 7/8" Fiberglass Strip (sample #10)

experiment could be made, and the best fitting value of DC flow resistance determined, it was necessary to correct one or the other for empty cavity losses. Possible sources of empty cavity losses are considered in the next subsection.

3. Sources of Loss in the Empty Cavity

In deriving the dispersion relation for the new resonance technique it was assumed that the only losses which occur in the plane wave resonator are due to viscous and thermal losses within the fluid saturated porous solid. Although these are the largest sources of loss in the cavity, other loss mechanisms must be accounted for. To account for these, several assumptions were made:

- (1) the losses in the empty cavity remain the same even though a portion of the volume and wall surface is lost due to the introduction of a fiberglass sample (less than 10%),
- (2) the shift of resonance frequency due to the introduction of a fiberglass sample does not effect the Q of the empty cavity and,
- (3) each loss mechanism can be treated as acting independently.

Generally, stated, it was assumed that,

$$\begin{array}{lclcl} \text{Total losses in the} & = & \text{losses in the} & + & \text{losses due to} \\ \text{fiberglass filled} & & \text{empty cavity} & & \text{only to fiber-} \\ \text{cavity} & & & & \text{glass} \end{array}$$

which can be written in terms of quality factors as

$$\frac{1}{Q_{TOT}} = \frac{1}{Q_E} + \frac{1}{Q_F} \quad , \quad (3.6)$$

where Q_{TOT} is the Q of the cavity due to all loss mechanisms, Q_E is the empty cavity Q and Q_F is the Q due to viscous and thermal losses within the fiberglass. Eq. (3.6) was used to compare the measured values of Q_{TOT} to the calculated values of Q_F for the [100] and [010] modes by setting the values of Q_E equal to those experimentally determined for the empty cavity.

TABLE 14

[100] MODE CENTER FREQUENCY AND Q VALUES

<u>Sample #</u>	<u>Thickness (cm)</u>	<u>f_c (Hz)</u>	<u>f_l (Hz)</u>	<u>f_u (Hz)</u>	<u>Q</u>
Empty	0.0	680.2 \pm 0.1	678.2 \pm 0.1	682.8 \pm 0.1	147.9 \pm 0.8
1	0.48	669.5	663.9	675.3	58.7
2	0.64	667.5	661.3	674.1	52.2
3	0.95	658.6	648.8	668.1	34.1
4	1.27	652.1	640.1	664.2	27.1
5	1.75	646.3	628.9	659.9	20.9
6	2.22	623.6	587.0	650.5	9.8
7	2.54	614.1	567.4	647.6	7.7
8	3.18	592.3	531.9	629.7	6.1
9	3.81	571.6	506.6	624.3	4.9
10	4.76	570.0	495.4	672.6	3.2

TABLE 15

[010] MODE CENTER FREQUENCY AND Q VALUES

<u>Sample #</u>	<u>Thickness (cm)</u>	<u>f_c (Hz)</u>	<u>f_ℓ (Hz)</u>	<u>f_u (Hz)</u>	<u>Q</u>
Empty	0.0	870.2 \pm 0.1	863.0 \pm 0.1	878.1 \pm 0.1	57.6 \pm 0.9
1	0.48	865.1	854.5	874.4	43.5
2	0.64	864.4	852.0	876.2	35.7
3	0.95	858.8	846.4	872.3	33.2
4	1.27	856.5	841.1	873.1	26.8
5	1.75	853.2	834.4	874.9	21.1

An attempt to identify the major source of loss in the empty cavity was made, as this in turn determined the value of Q_E to be used in correcting for losses other than in the fiberglass. The loss mechanisms in the empty cavity were assumed to be due to 3 mechanisms:

- transmission of energy through the plexiglass walls of the cavity,
- viscous and thermal losses at the interior surfaces of the cavity,
- leakage of energy due to incomplete sealing of the top cover and sliding section of the cavity and slide bar assembly.

The transmission of energy through the walls was of concern mainly since the cavity was not designed specifically for this experiment. For normal incidence, the transmission loss through the walls of the cavity was calculated to be 32 dB for the minimum wall thickness (1.27 cm), [Ref. 17, p. 128]. Based on the maximum wall thickness (2.54 cm) the lowest expected coincidence frequency for a free plexiglass plate was calculated to be 1282 Hz. For a plate fixed about its edges this frequency is higher. Therefore, transmission by coupling to flexural waves in the walls can be ignored. The following equation was used to estimate the Q resulting from each source of loss:

$$Q = \frac{2\pi E_{\text{stored}}}{E_{\text{lost/cycle}}} , \quad (3.7)$$

where

$$E_{\text{stored}} = \epsilon V \quad (3.8)$$

and ϵ is the average energy density, and V is the interior volume of the cavity. The energy lost per cycle can be written

$$E_{\text{lost/cycle}} \cong \frac{Ac}{4} \epsilon T_I \frac{1}{f} , \quad (3.9)$$

where A is the surface area, c is the speed of sound in the fluid, T_I the power transmission coefficient and f is the frequency. Inserting Eq. (3.8) and (3.9) into Eq. (3.7) results in

$$Q_{\text{trans}} \cong \frac{8\pi V}{\lambda T_I A} \cdot \quad (3.10)$$

For loss due to transmission through the cavity walls, assuming 1000 Hz as the worst case ($\lambda = 0.343$ m), the value of Q_{trans} was calculated to be 2700. It was concluded that transmission through the walls was not significant.

Next considered were the effects of the viscous and thermal losses occurring at the cavity surfaces. Again Eq. (3.7) was used to determine Q_{surf} , with E_{stored} remaining the same as in Eq. (3.8). The energy lost per cycle due to viscous effects can be written approximately as

$$E_{\text{lost/cycle}} \cong \epsilon A \delta_{\text{visc}} \quad (3.11)$$

where δ_{visc} is the viscous penetration depth in air. The energy lost per cycle due to thermal effect can be written approximately as

$$E_{\text{lost/cycle}} \cong \epsilon A (\gamma - 1) \delta_{\text{th}} \quad (3.12)$$

where γ is the ratio of specific heats c_p/c_v ($\cong 1.4$) for the air and δ_{th} is the thermal penetration depths in air. Since the viscous and thermal penetration depths in air are approximately equal, an expression for the energy lost per cycle due to both viscous and thermal effects is

$$E_{\text{lost/cycle}} \cong \epsilon A \delta_{\text{visc}} \gamma \cdot \quad (3.13)$$

In other words,

$$\delta_{\text{visc}} + (\gamma - 1) \delta_{\text{th}} \cong \gamma \delta_{\text{visc}} \cdot \quad (3.14)$$

Substituting Eq. (3.8) and (3.13) into Eq. (3.7) results in

$$Q_{\text{surf}} \cong \frac{2\pi V}{A \delta_{\text{visc}} \gamma} \cdot \quad (3.15)$$

Choosing a frequency of 100 Hz for the worst case (greatest viscous and thermal penetration depths), with the air temperature in the cavity assumed to be 20°C, the resulting Q_{surf} was 450. Therefore, viscous and thermal wall losses are negligible.

Lastly, the loss due to leakage past cavity sliding surfaces was considered. Since this loss could not be directly calculated, a measure of its significance was estimated by pressing down on the top cover of the cavity at the wall edges while retaking the [100] mode resonance curve data for each sample. The empty cavity Q increased from 147 to 252, with a 0.9 Hz upshift in the center frequency. From this experiment, a value of Q for leakage was estimated to be approximately 280. This indicated that leakage was the major source of loss in the empty cavity by at least a factor of two. The leakage problem could not be corrected without making major changes in the cavity design. No attempt was made to account for the upshift in the center frequency that occurred while pressing down on the cavity top (the frequency upshift was on the order of 1 Hz for each sample, while the frequency downshift due to introducing the fiberglass was on the average of 10 to 12 Hz drop per sample).

4. Determination of R_{DC} from f_C and Q

For the [100] mode, the iterative process used to extract the DC flow resistance of the fiberglass from the dispersion relation (Eq. (2.51)) was started by choosing R_{DC} equal to 59,200 MKS Rayl/m (the mean flow resistance determined in the large sample holder with particle velocity normal to the air-fiberglass surface). After entering the fluid and cavity parameters (see Appendix A for parameters and values used), the roots of the dispersion relation for $\tilde{\omega}$ were then determined for each sample using the measured values of f_C and Q as an initial starting point. The resulting roots for each sample were numerically computed until the sum of the magnitudes of the real and imaginary parts of the dispersion relation (Eq. 2.51) was less than 1×10^{-6} . By this means, calculated values of Q_F vs f_C were obtained for a particular value of R_{DC} .

The calculated and measured values of Q vs f_C were compared in two ways. Figure 3.16 shows Q_{TOT} vs f_C . Here the calculated values of Q_F have

been corrected for empty cavity losses using Eq. (3.6). Figure 3.17 shows Q_F vs f_C . Here the measured values of Q_{TOT} have been corrected for empty cavity losses using

$$\frac{1}{Q_F} = \frac{1}{Q_{TOT}} - \frac{1}{Q_E}.$$

If the calculated curve plotted above the measured curve, this indicated too high a value of R_{DC} and a lower value of R_{DC} was chosen. If the curve plotted below the measured curve, this indicated too low a value of R_{DC} and a larger value of R_{DC} was chosen. This process was continued until the measured curve was bounded between two values of R_{DC} . Once bounded, smaller increments were chosen for R_{DC} and the process was continued until a best fit (graphically) was obtained between the calculated and measured curves of Q_F or Q_{TOT} vs f_C . For the [100] mode, the best fit value for R_{DC} was 15,000 MKS Rayl/m, which was four times less than that measured experimentally.

Two possible causes were investigated to explain this discrepancy. The first possible cause is the 10% compression of the samples observed in the original DC flow resistance experiment (large sample holder). Assuming the total pressure drop across the test sample was independent of the compressed thickness, the extracted value of DC flow resistance per unit length should be corrected from 59,200 MKS Rayl/m to 53,000 MKS Rayl/m. The second possible cause is that the flow resistance of the fiberglass is not isotropic, and that it is greater for flow perpendicular to the sheet faces. This might be expected, as there is visual evidence that the fiberglass sheets have been compressed. In the first flow resistance measurement, the fiberglass sample was oriented so that the fiberglass sheet surface was normal to the flow velocity. However, for the [100] mode, the particle velocity is parallel to the fiberglass sheet surface. Flow resistance tests were again conducted, using a much smaller sample holder, with samples cut so that the anisotropy in

Q_{TOT} vs Center Frequency

([100] MODE--VARYING R_{DC} VALUES)

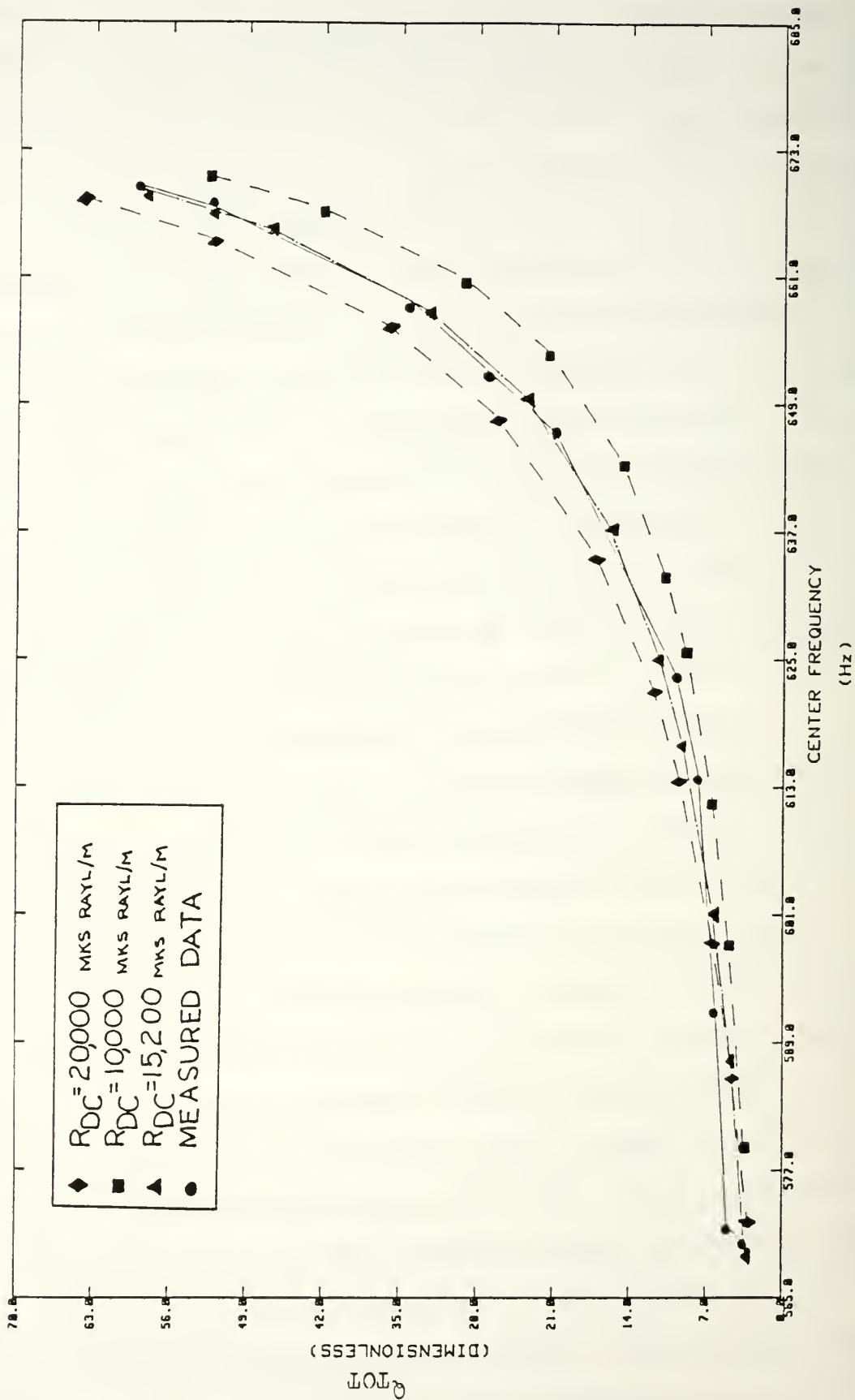


Figure 3.16 [100] Mode Q_{TOT} vs f_c

Q_F vs Center Frequency
([100] Mode--VARYING R_{DC} VALUES)

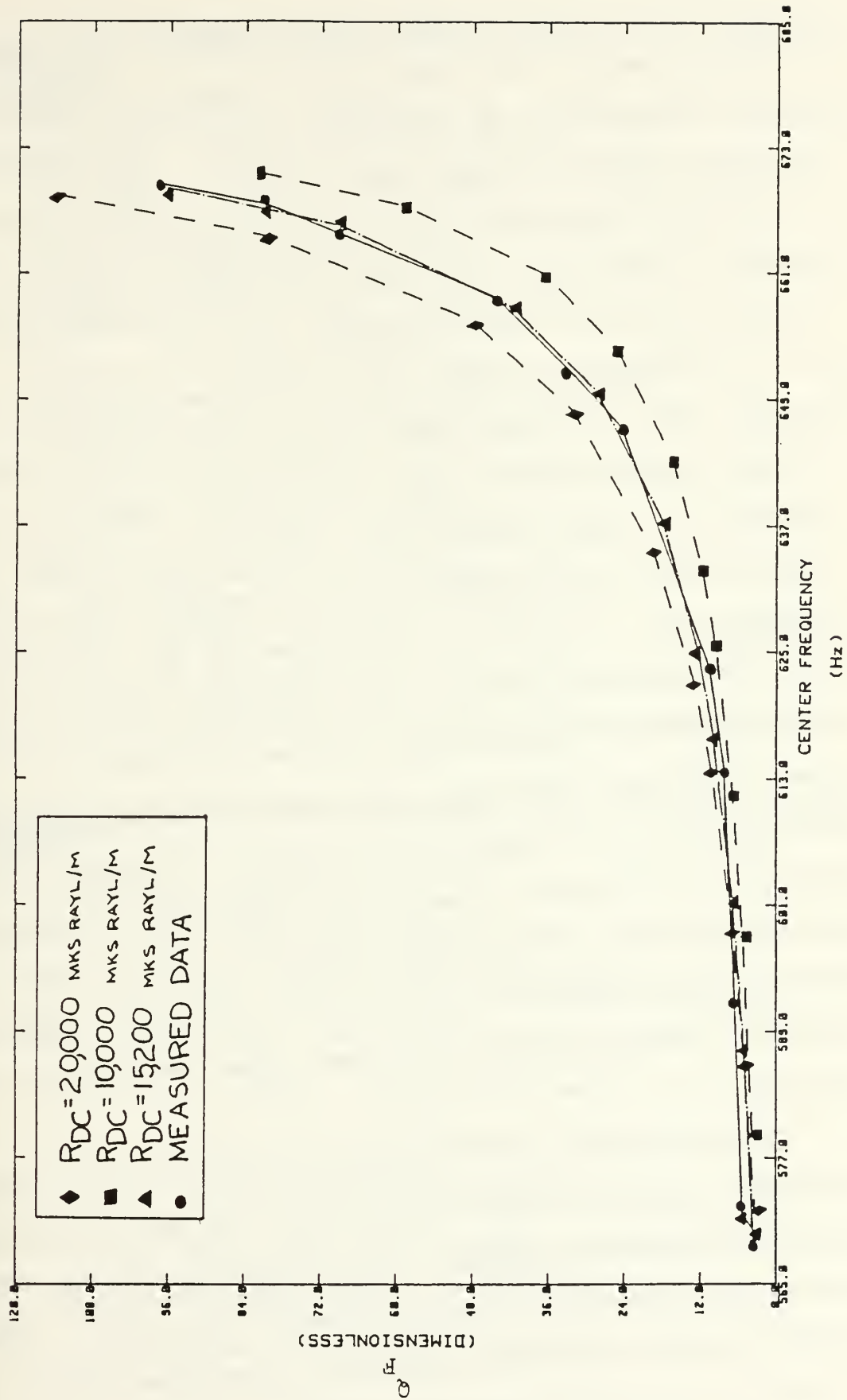


Figure 3.17 [100] Mode Q_F vs f_C

R_{DC} could be measured. As indicated earlier in this chapter, the flow resistance normal to the sheet surface now measured approximately three times greater than that parallel to the sheet surface. The value measured with flow parallel to the surface was 15,200 MKS Rayl/m. With this value of R_{DC} , the roots of the dispersion relation were recalculated, Q_{TOT} and Q_F calculated and plotted. These values fell within 8% of measured values for Q_{TOT} vs f_c and within 12% for Q_F vs f_c for all samples.

The method of extracting R_{DC} from measured values of f_c and Q was then applied to the [010] mode, which has particle velocity normal to the sheet surface. Starting with a value of 34,000 MKS Rayl/m for R_{DC} (the value measured in the small sample holder), values of Q vs f_c were calculated for various values of R_{DC} and were compared with measured values of Q vs f_c . The measured values of Q vs f_c are bounded by the calculated curves for $R_{DC} = 5,000$ MKS Rayl/m and $R_{DC} = 20,000$ MKS Rayl/m, and are consistent with a value of 15,000 MKS Rayl/m for R_{DC} , the same as for the [100] mode. This is shown in Figures 3.18 and 3.19. The reason for the discrepancy between these bounding values and the measured value of R_{DC} for flow normal to the fiberglass sheet face is not known. It may be due to mode overlap of both the [110] and [100] modes on to the [010] mode. Figures 3.20 and 3.21 show plots of the resonance center frequency for the [100] and [010] modes, respectively, as a function of sample thickness for the same values of R_{DC} as in Figures 3.18 and 3.19.

Having determined that the best fit value of the DC flow resistance in the porous material was approximately 15,000 MKS Rayl/m, the complex wave number and characteristic impedance were calculated using Eq. (2.56) and Eq. (2.57) and the roots of the dispersion relation, (Eq. (2.51)). Table 16 lists the results for the [100] mode, while Table 17 lists those for the [010] mode. The data for both modes is graphically presented in Figures 3.22 through 3.26.

5. Sensitivity of Roots of the Dispersion Relation to Variation in Parameters

In order to determine the sensitivity of the roots of the dispersion relation to variations in fluid and porous material physical properties, the roots were again calculated for the [100] mode with each of the input parameters changed by a small amount, one at a time, and the characteristic impedance and complex wave number were recalculated.

It was found that there was less than a 1% change in \tilde{k} and \tilde{z}_{char} when porosity was decreased to 0.95 (5% change), when bulk fluid sound speed was changed to 343 m/s (0.6% change or 2 m/s), and when bulk fluid density was changed to 1.23 Kg/m³ (1.6% change or 0.02 Kg/m³). However, an 11% change in \tilde{k} and \tilde{z}_{char} was found when the DC flow resistance was varied by $\pm 5,000$ MKS Rayl/m about 15,000 MKS Rayl/m. Because the uncertainty in the measured data is so much greater, the sensitivity of the best fit value of R_{DC} , and hence \tilde{k} and \tilde{z}_{char} , to slight uncertainties in other physical properties is negligible.

6. Modal Pressure Field in a Rectangular Cavity with Porous Acoustic Material

To theoretically determine the [100] and [010] modal pressure distribution in the cavity for each fiberglass sample requires the values of \tilde{k}_{1z} and \tilde{k}_{2z} be determined from the roots of the dispersion relation for $\tilde{\omega}$ for the best fit value of R_{DC} . Then, using Eq. (2.63) for the bulk fluid and Eq. (2.64) for the porous material, the normalized magnitude and phase of the pressure at each grid point can be determined. See Appendix B for a more detailed discussion. For the [100] mode, Figure 3.27 shows graphically the results for sample #1 (3/16") and Figure 3.28 shows the results for sample #10 (1 7/8"). For the [010] mode, Figure 3.31 shows graphically the results for sample #1 (3/16") and Figure 3.32 shows the results for sample #5 (11/16").

Q_{TOT} vs Center Frequency
([010] Mode -- VARYING R_{DC} VALUES)

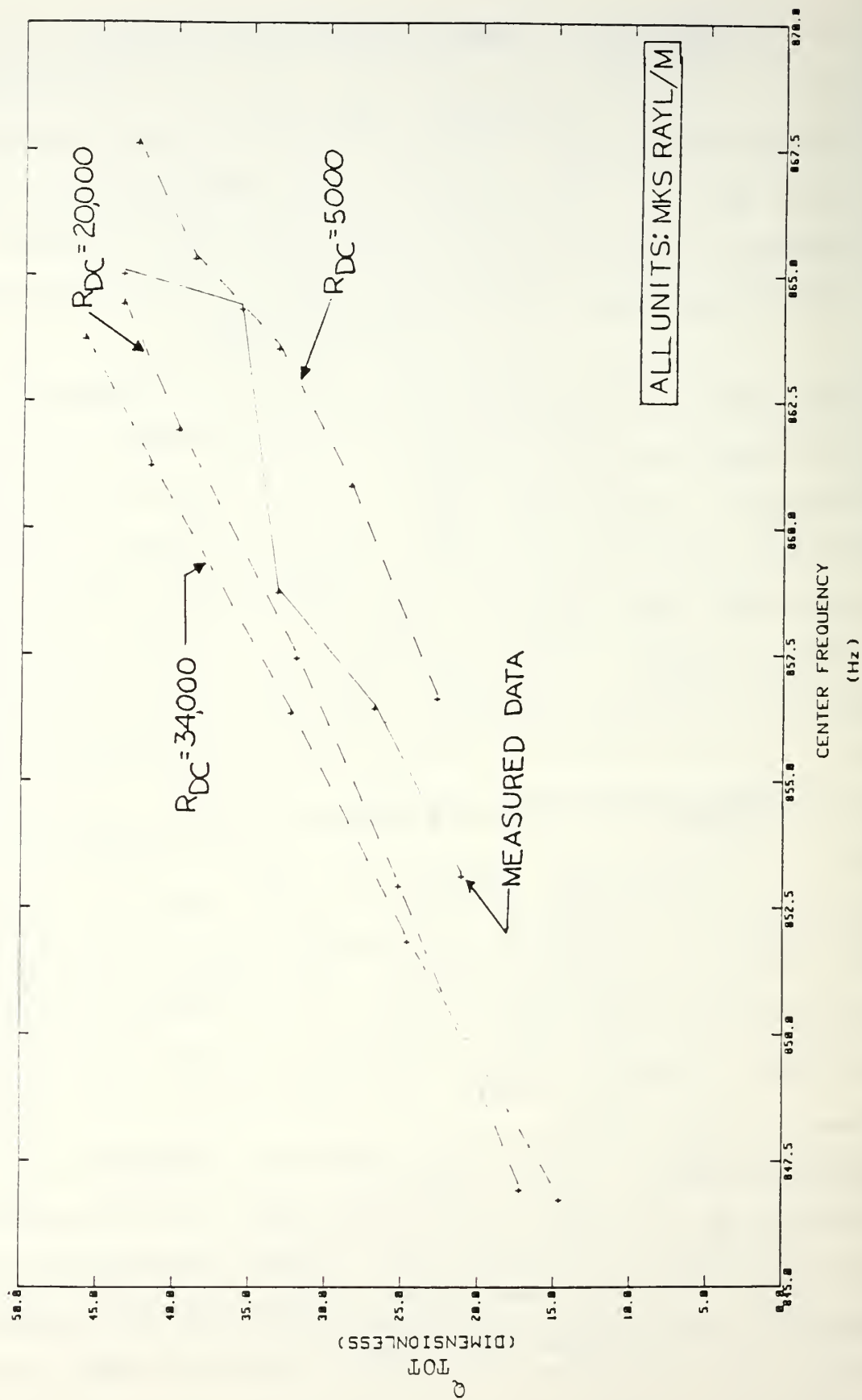


Figure 3.18 [010] Mode Q_{TOT} vs f_c

Q_F vs Center Frequency
([010] Mode---VARYING R_{DC} VALUES)

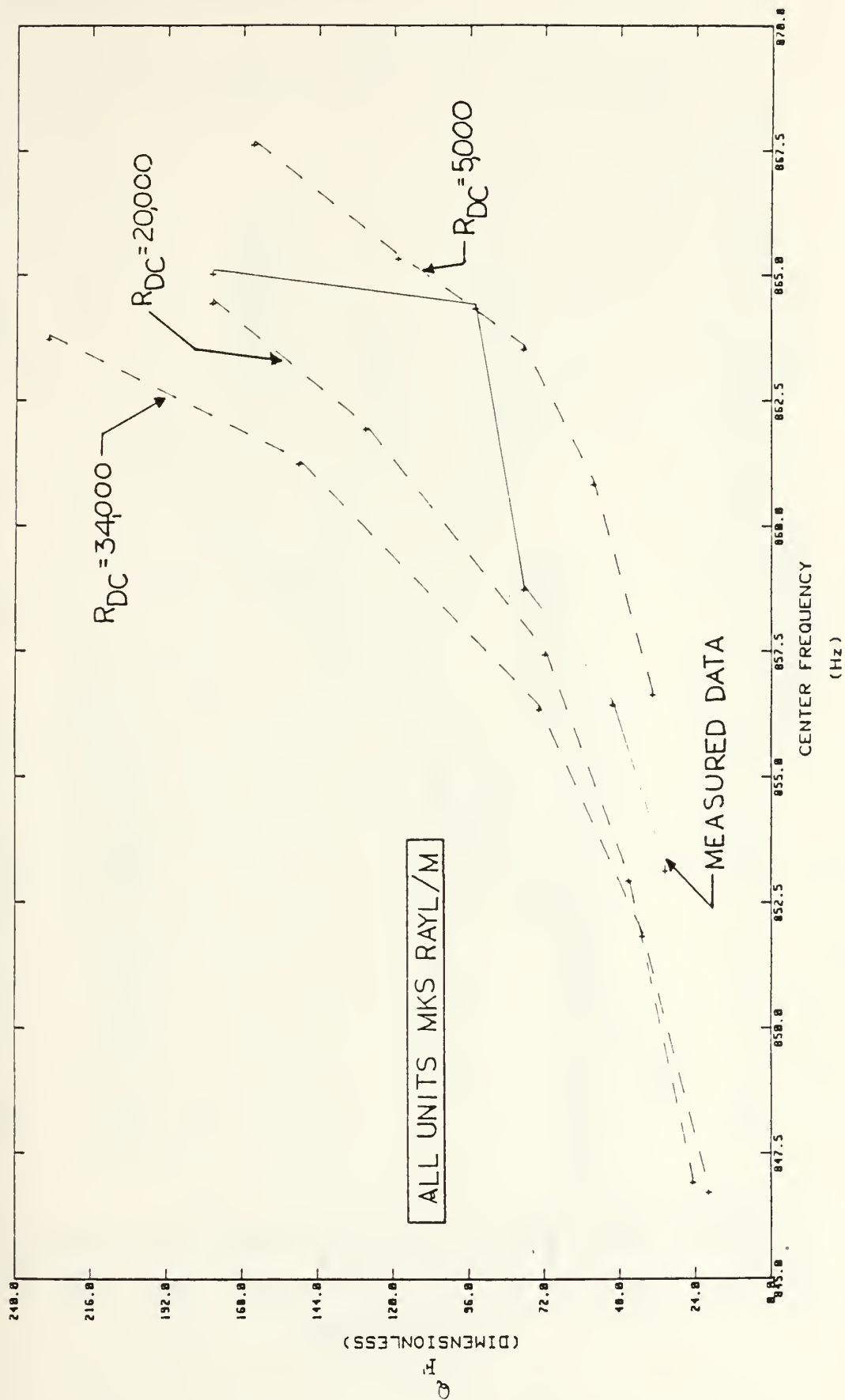


Figure 3.19 [010] Mode Q_F vs f_c

Center Frequency vs Thickness ([100] Mode---VARYING R_{DC} VALUES)

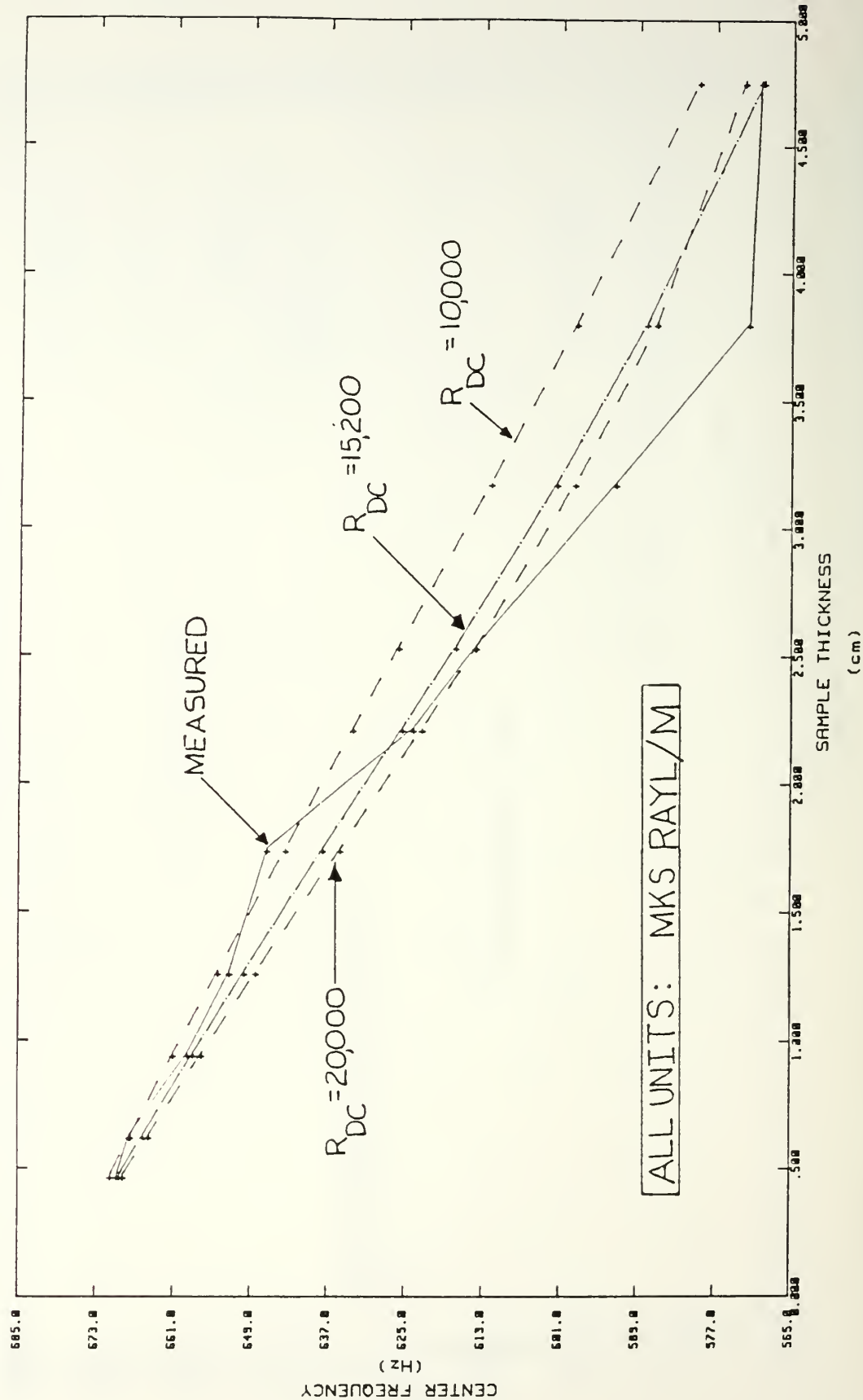


Figure 3.20 [010] Mode f_c vs Sample Thickness

Center Frequency vs Frequency

([010] Mode--VARYING R_{DC} VALUES)

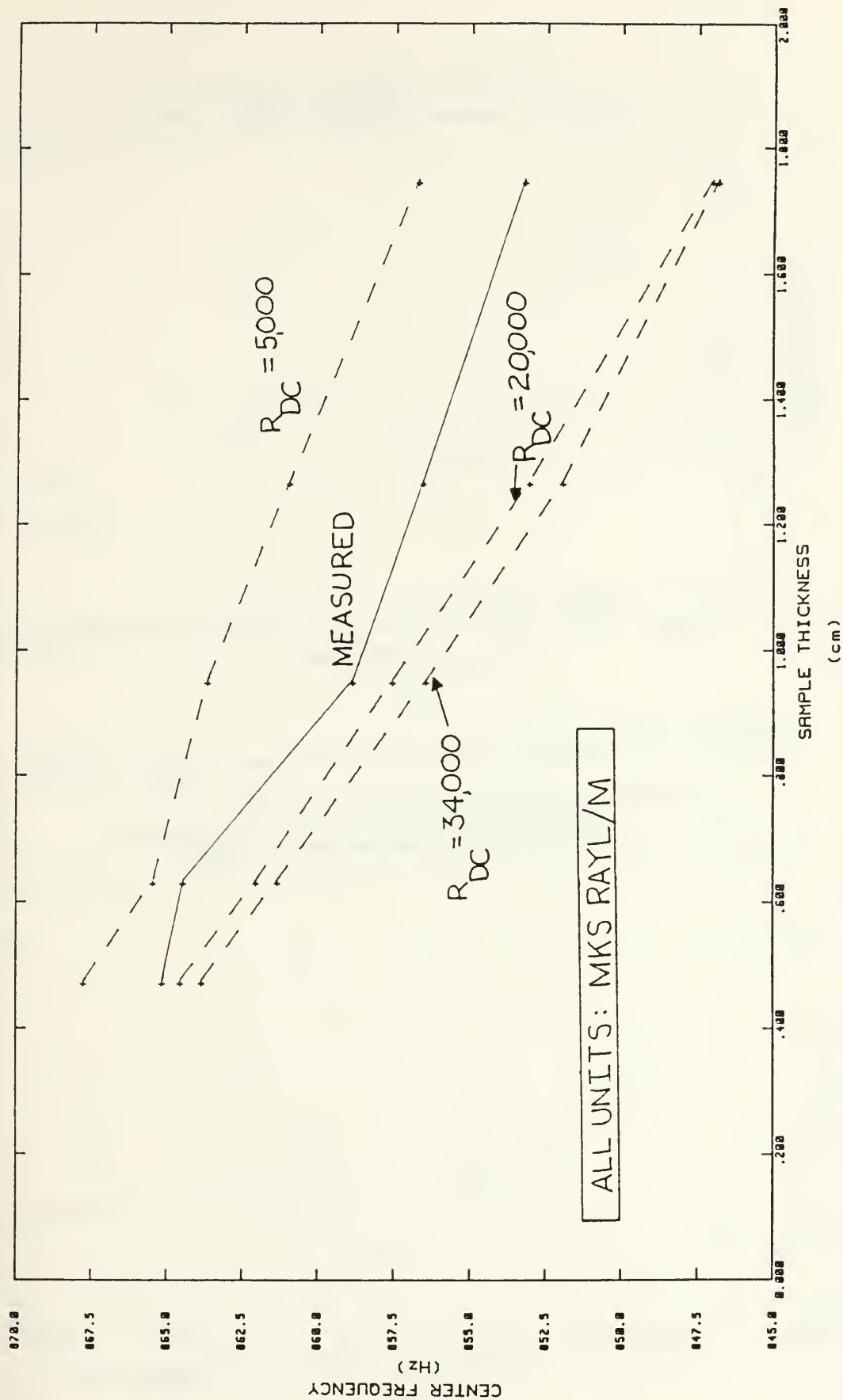


Figure 3.21 [010] Mode f_c vs Sample Thickness

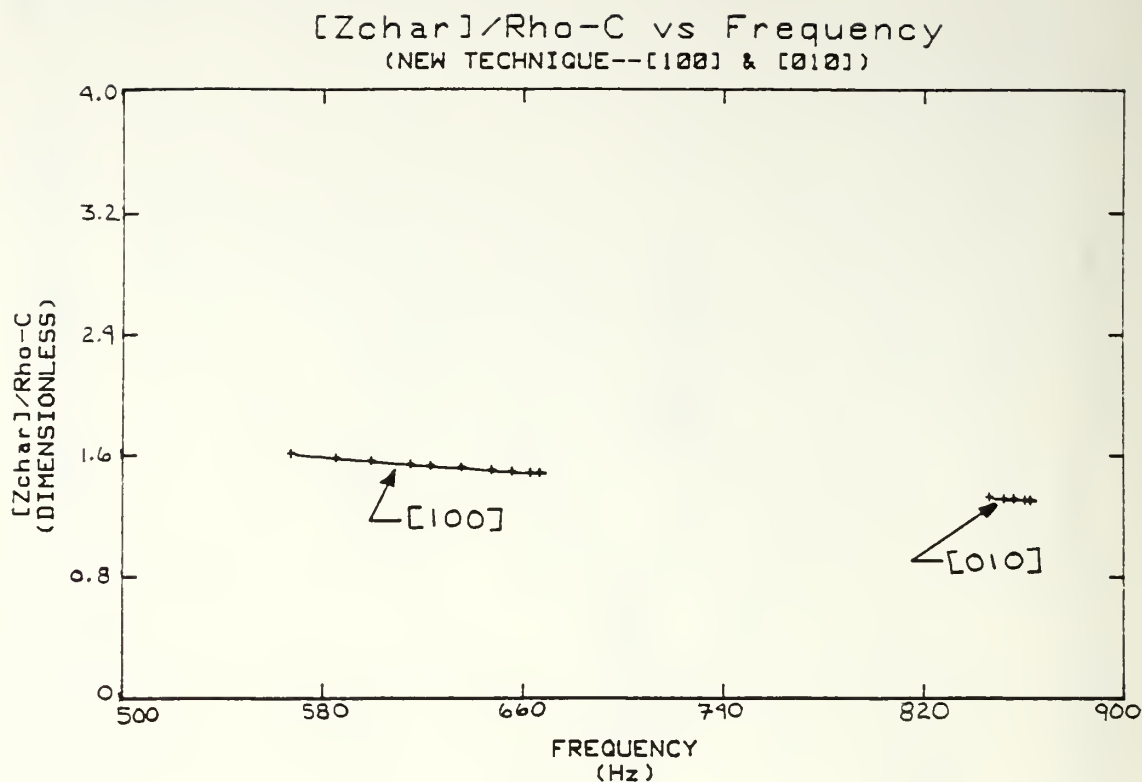


Figure 3.22 $|\tilde{Z}_{char}|/\rho_0 c$ vs f For New Method ([100] and [010] Modes)

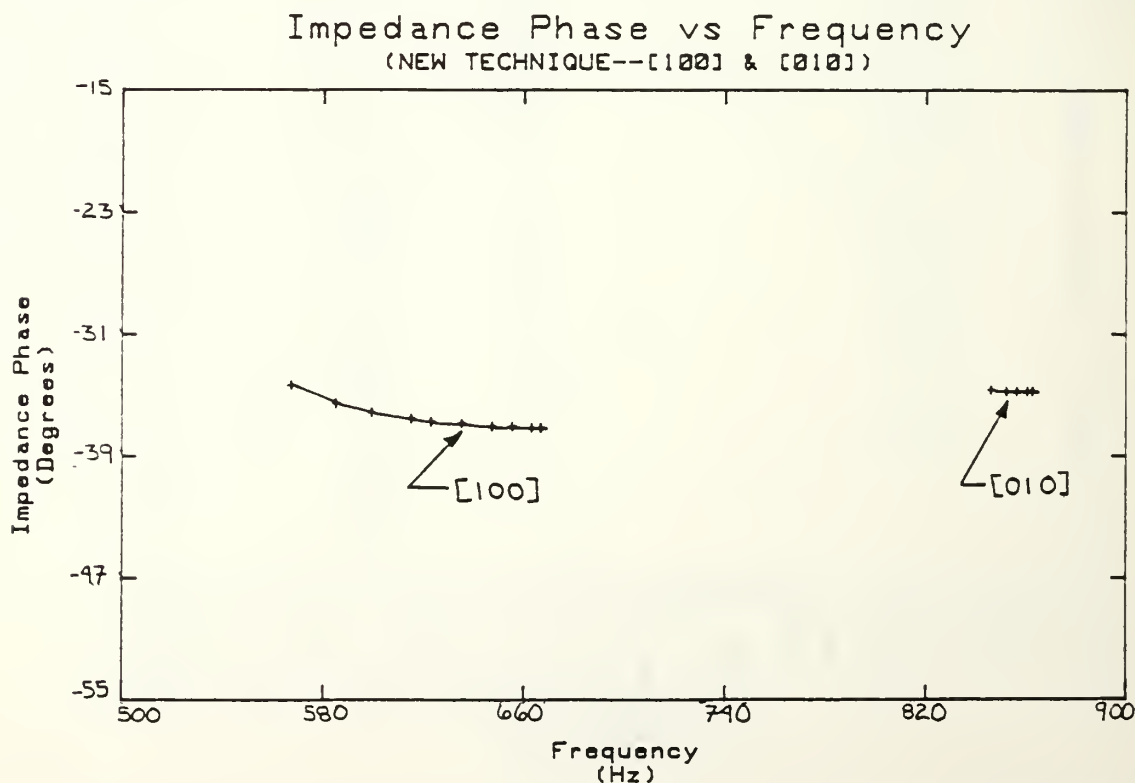


Figure 3.23 ϕZ_{char} vs f For New Method ([100] and [010] Modes)

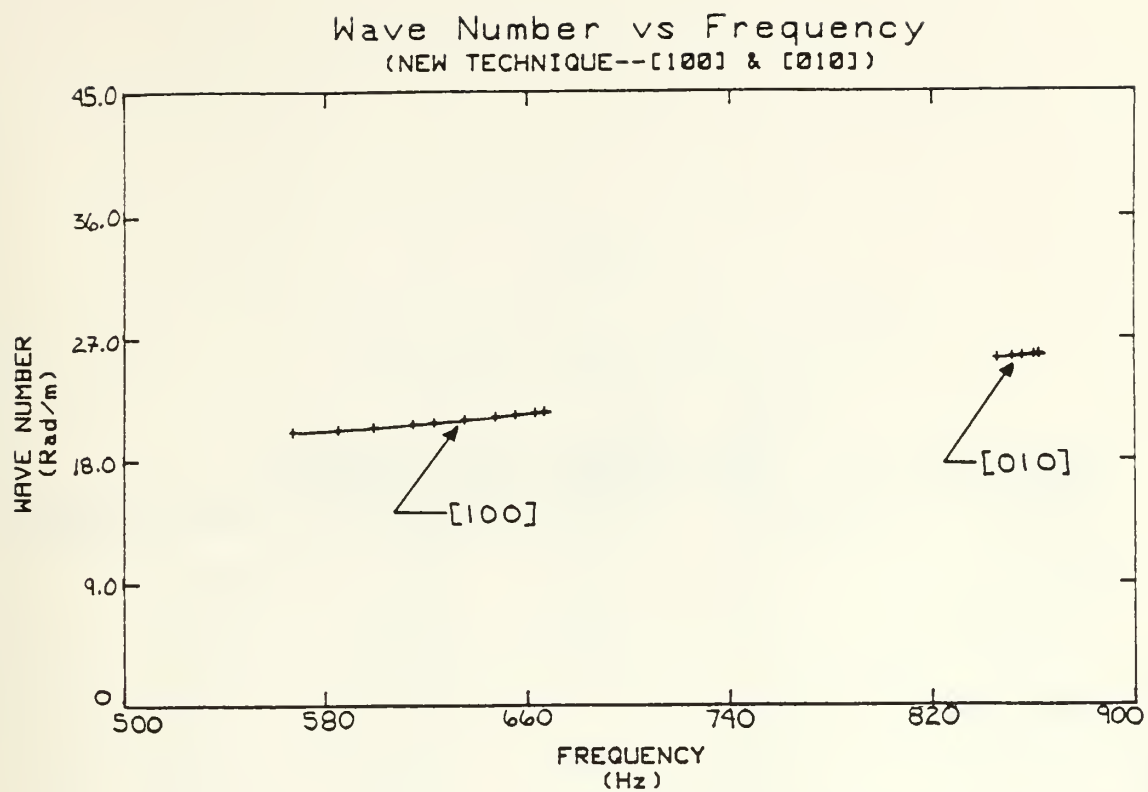


Figure 3.24 k vs f For New Method ([100] and [010] Modes)

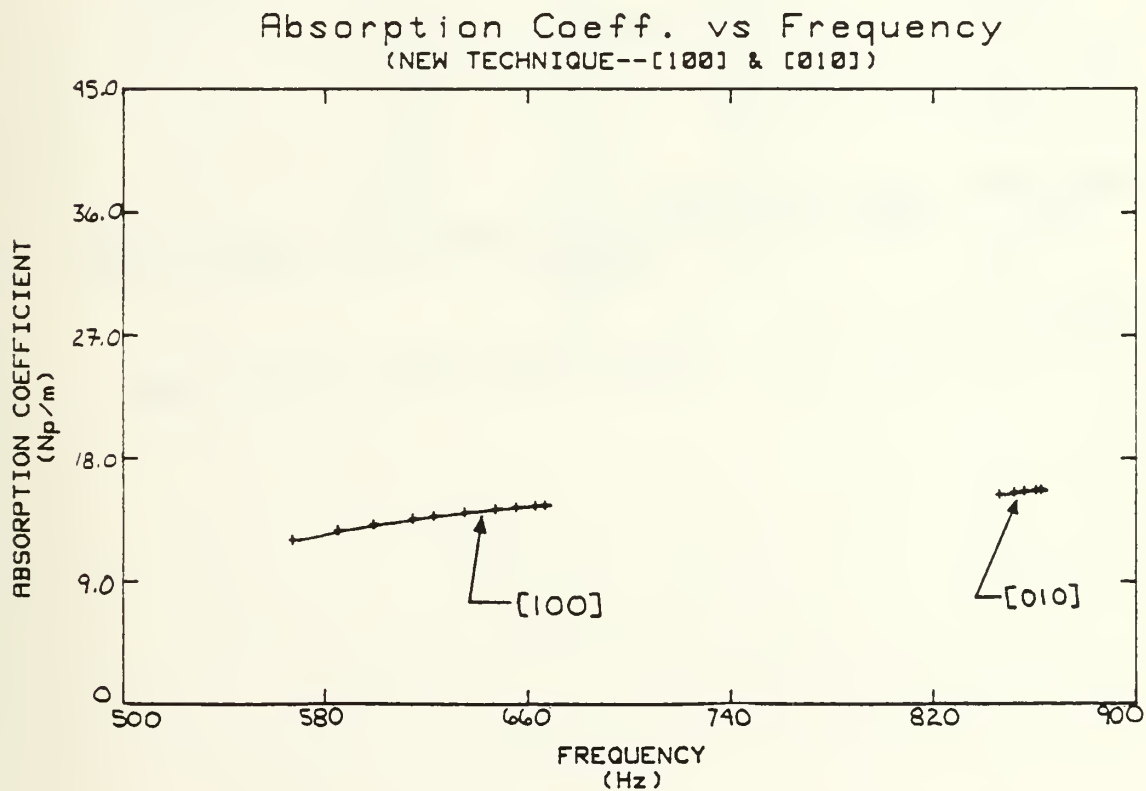


Figure 3.25 a vs f For New Method ([100] and [010] Modes)

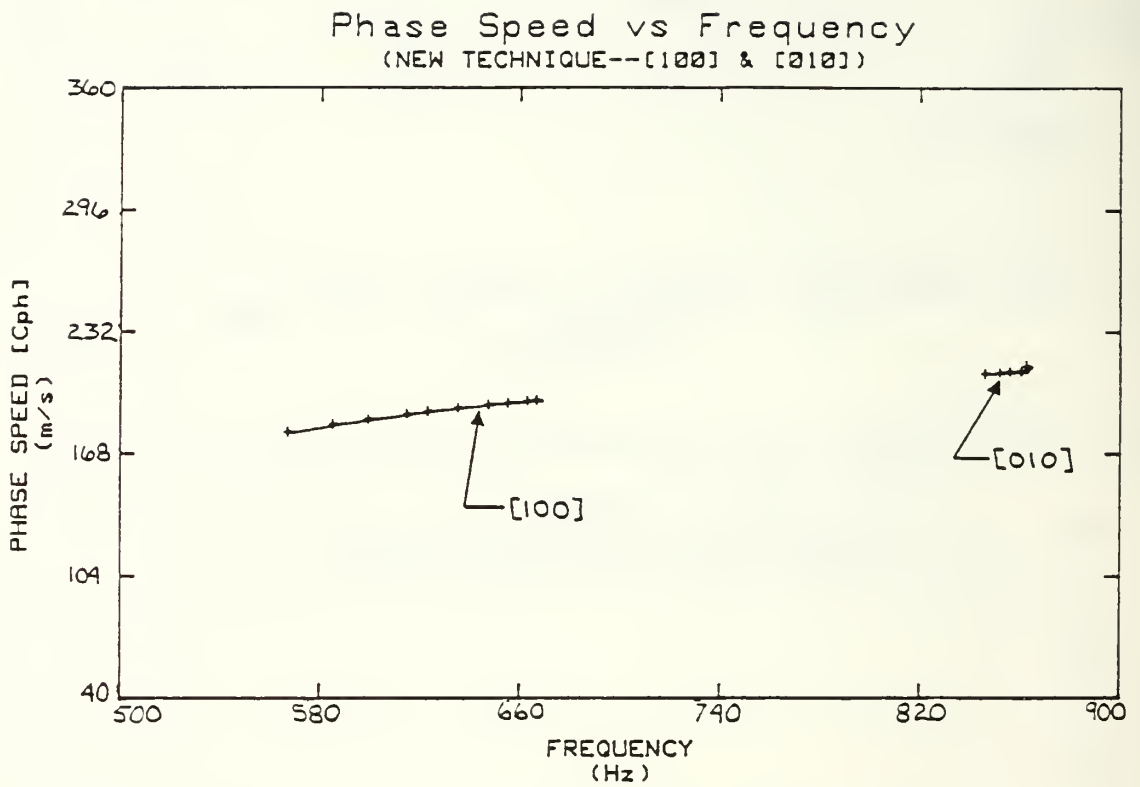


Figure 3.26 c_{ph} vs f For New Method ($[100]$ and $[010]$ Modes)

TABLE 16

\tilde{z}_{char} AND \tilde{k} RESULTS FOR [100] MODE
 ($R_{\text{DC}} = 15,200$ MKS Rayl/m)

Sample #	f_c (Hz)	k (Rad/m)	a (Np/m)	$ \tilde{z}_{\text{char}} /\rho_0 c$	$\phi_{\tilde{z}_{\text{char}}}$ (degrees)	c_{ph} (m/s)
1	669.4 \pm 0.1	21.54	14.53	1.48	-37.2	195.2
2	665.4	21.47	14.47	1.48	-37.2	194.8
3	657.7	21.32	14.35	1.49	-37.1	193.8
4	649.8	21.17	14.21	1.50	-37.1	192.9
5	637.6	20.95	13.98	1.52	-37.0	191.2
6	625.3	20.74	13.71	1.53	-36.8	189.4
7	617.1	20.61	13.52	1.54	-36.6	188.1
8	601.5	20.38	13.10	1.56	-36.2	185.4
9	587.4	20.19	12.66	1.58	-35.6	182.8
10	569.5	20.03	11.96	1.61	-34.4	178.6

TABLE 17

\tilde{z}_{char} AND \tilde{k} RESULTS FOR [010] MODE
 ($R_{\text{DC}} = 15,000$ MKS Rayl/m)

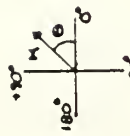
<u>Sample #</u>	<u>f_c (Hz)</u>	<u>k (Rad/m)</u>	<u>a (Np/m)</u>	<u>$\tilde{z}_{\text{char}} /\rho_0 c$</u>	<u>$\phi_{\tilde{z}_{\text{char}}}$ (degrees)</u>	<u>c_{ph} (m/s)</u>
1	865.0 \pm 0.1	25.76	15.67	1.30	-34.8	213.5
2	862.9	25.72	15.63	1.30	-34.8	210.8
3	858.5	25.64	15.55	1.31	-34.8	210.4
4	854.3	25.57	15.46	1.31	-34.8	209.9
5	848.3	25.47	15.29	1.32	-34.7	209.3

These plots present the mode's modal pressure field in phasor notation. The magnitude is represented by the size of the arrow and the phase angle by the angular rotation of the arrow in degrees from the horizontal (i.e., zero degrees of phase angle is a phasor pointing horizontally to the right).

Experimentally, the pressure field was measured by inserting each sample into the cavity and exciting the desired mode at its center frequency for that sample. By programming a HP-300 series computer to take data from the SR 530 Dual Channel Lock-In Amplifier (in the X, Y mode), the in-phase and quadrature components of pressure were measured at each grid point. The normalized magnitude and phase of the pressure was then plotted. For the [100] mode, Figure 3.29 displays the results for sample #1 (3/16") and Figure 3.30 displays the results for sample #10 (1 7/8"). The results for the [010] mode are displayed in Figures 3.33 and 3.34 for sample #1 (3/16") and sample #5 (11/16"), respectively.

In comparing the theoretical and experimental pressure field plots several observations can be made:

- (1) The effects of cavity leakage at the sliding surfaces is evident when the experimental plot (Figure 3.29) is compared to the theoretical plot (Figure 3.27) of the [100] mode for sample #1 (3/16") by noting that the pressure phasors along the boundaries not in contact with the fiberglass strip in Figure 3.29 exhibit a small increase in phase angle (i.e., they are not horizontal as they would be if no losses existed at the boundaries) which is not present in Figure 3.27. This effect may also be seen for the [010] mode in Figure 3.31 and Figure 3.33.
- (2) The effects of the porous material on the pressure distribution in the bulk fluid can be seen to "grow" with increasing sample thickness by observing the relative increase in the phase angle away from the



Theoretical Modal Pressure Field
 [100] Mode, 3/16" (sample #1)
 (NORMALIZED TO MAXIMUM)

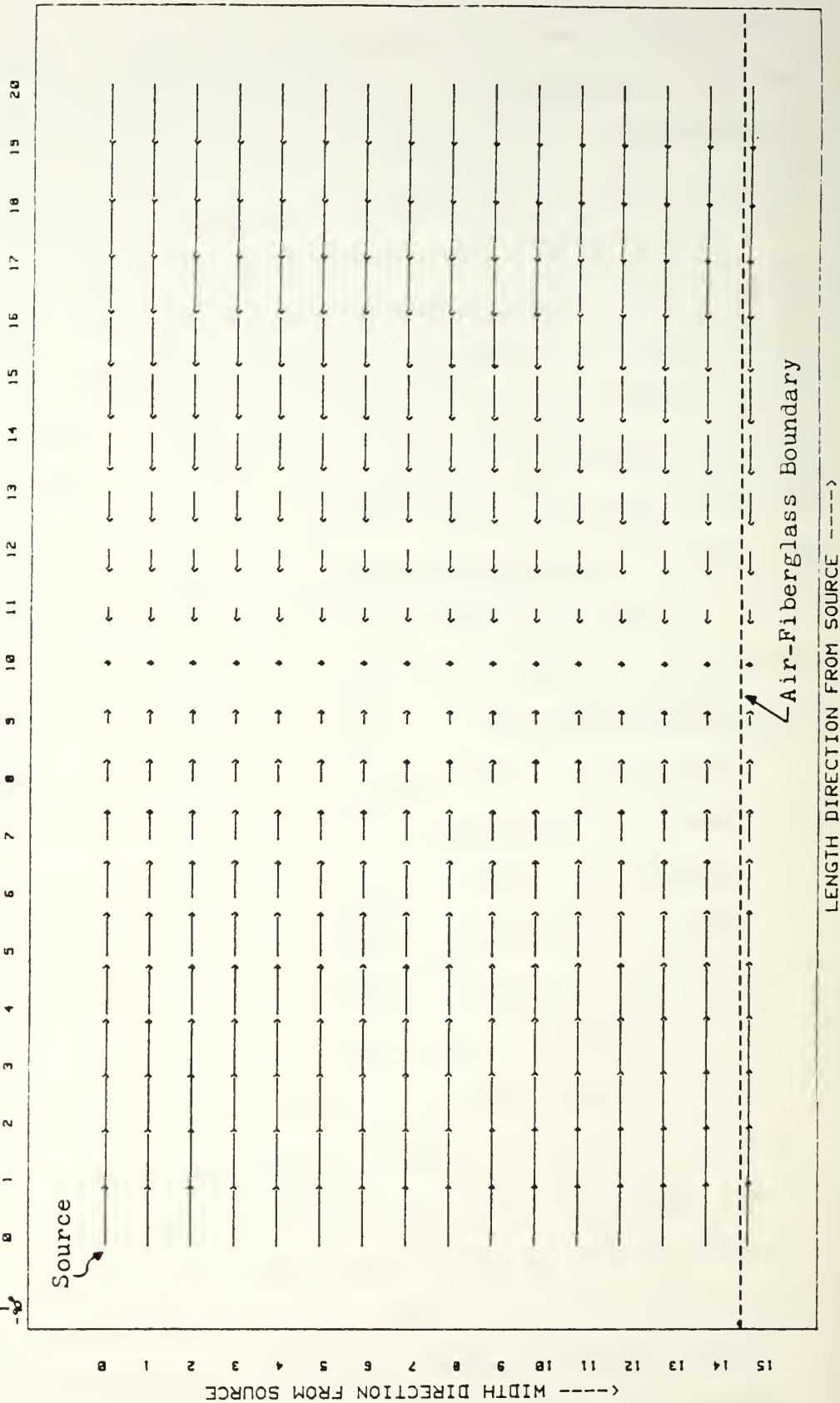


Figure 3.27 Theoretical [100] Mode Pressure Distribution for Sample #1

Theoretical Modal Pressure Field
 [100] Mode, 1-7/8" (sample #10)
 (NORMALIZED TO MAXIMUM)

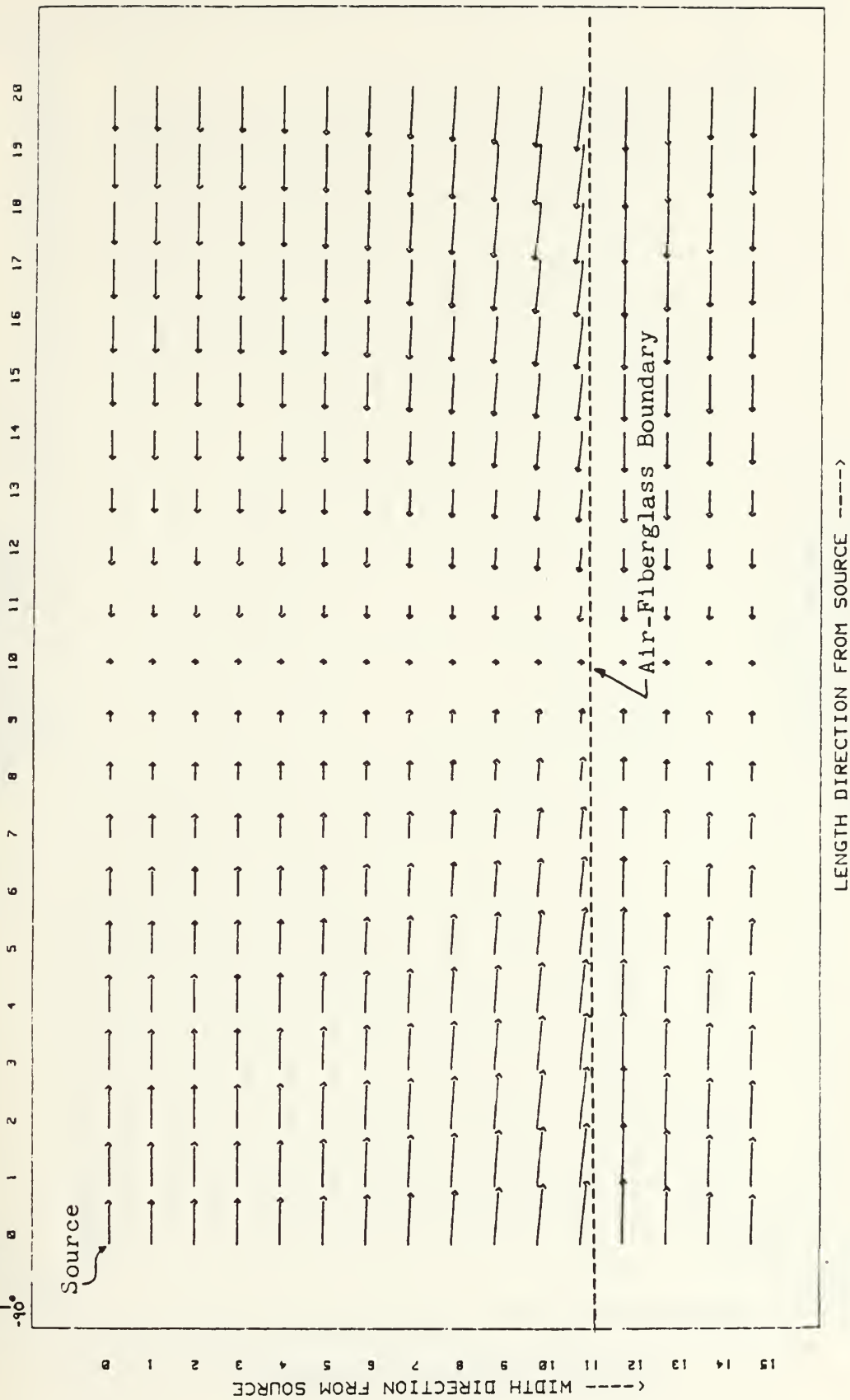


Figure 3.28 Theoretical [100] Mode Pressure Distribution for Sample #10

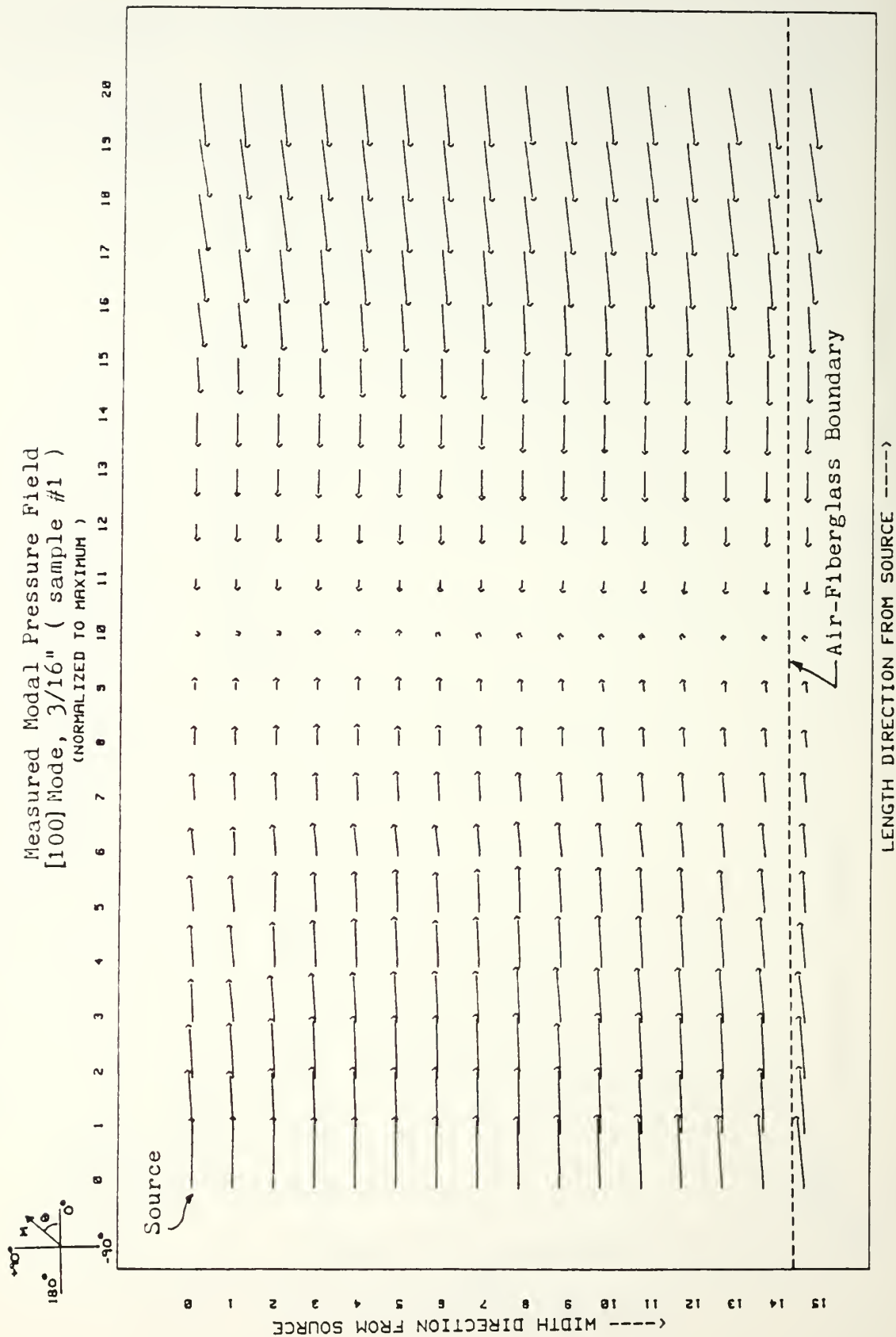


Figure 3.29 Experimental [100] Mode Pressure Distribution for Sample #1

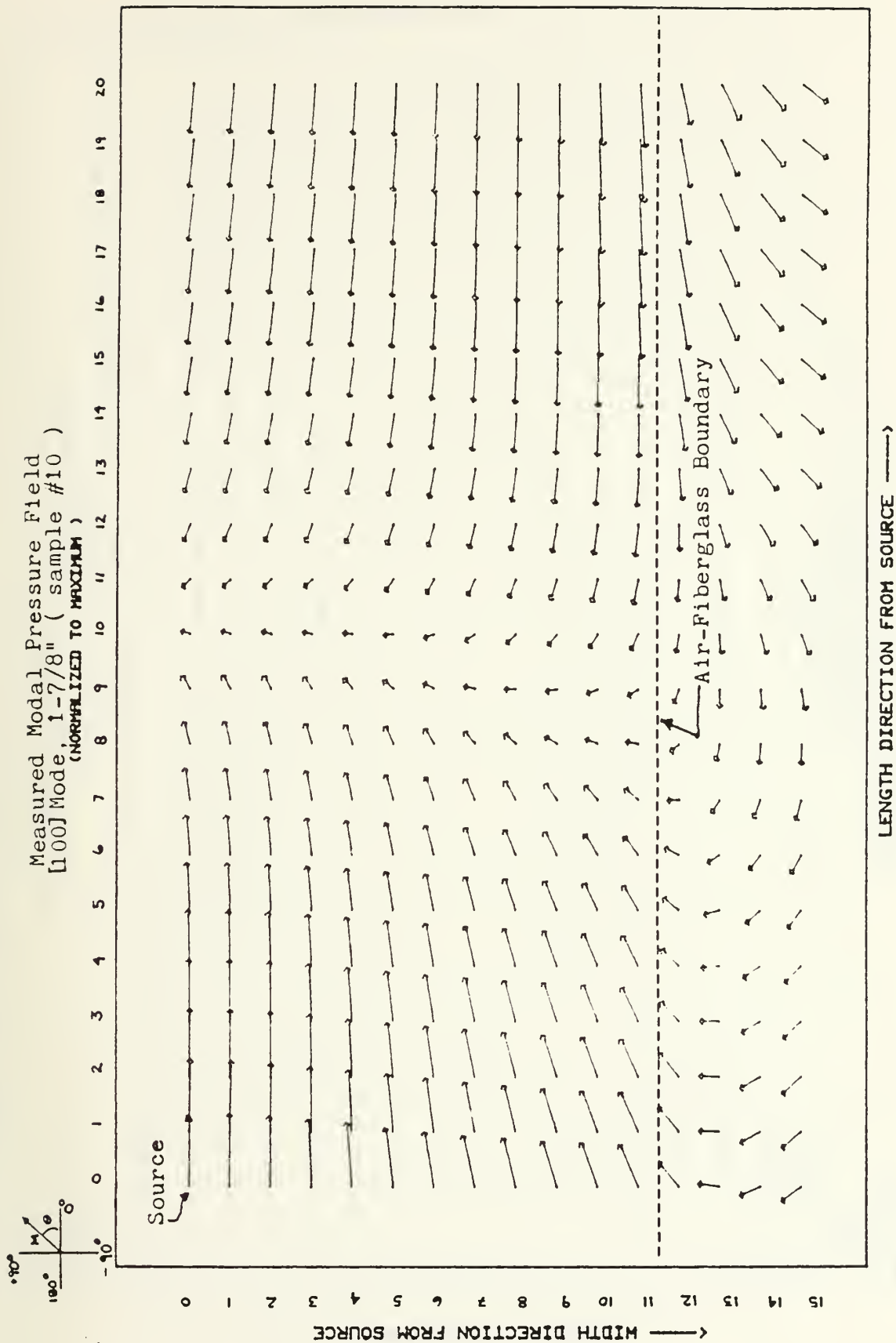


Figure 3.30 Experimental [100] Mode Pressure Distribution for Sample #10

Theoretical Modal Pressure Field
 [010] Mode, 3/16" (sample #1)
 (NORMALIZED TO MAXIMUM)

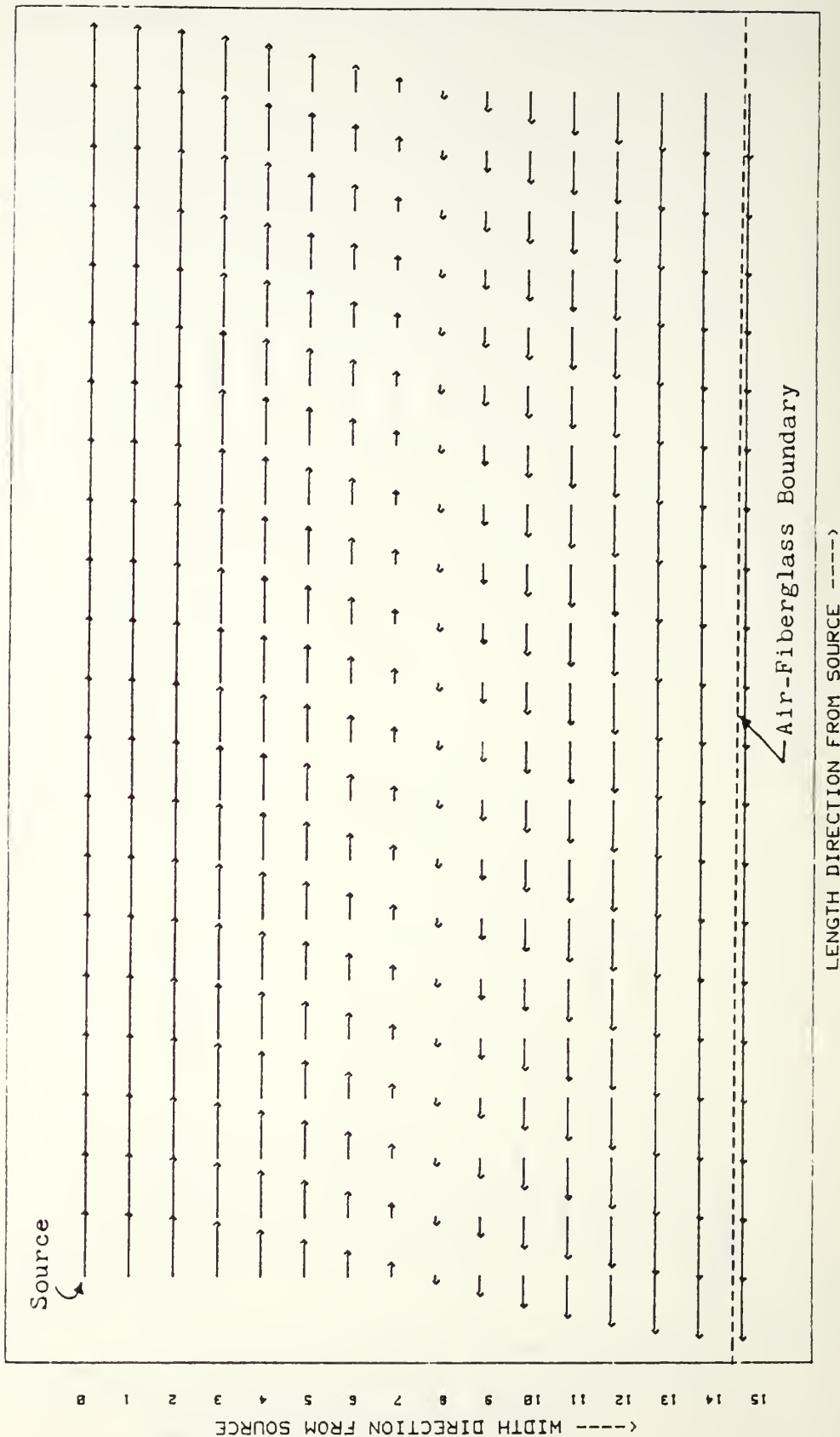
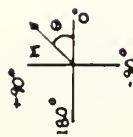


Figure 3.31 Theoretical [010] Mode Pressure Distribution for Sample #1

Theoretical Modal Pressure Field
 [010] Mode, 11/16" (sample #5)
 (NORMALIZED TO MAXIMUM)

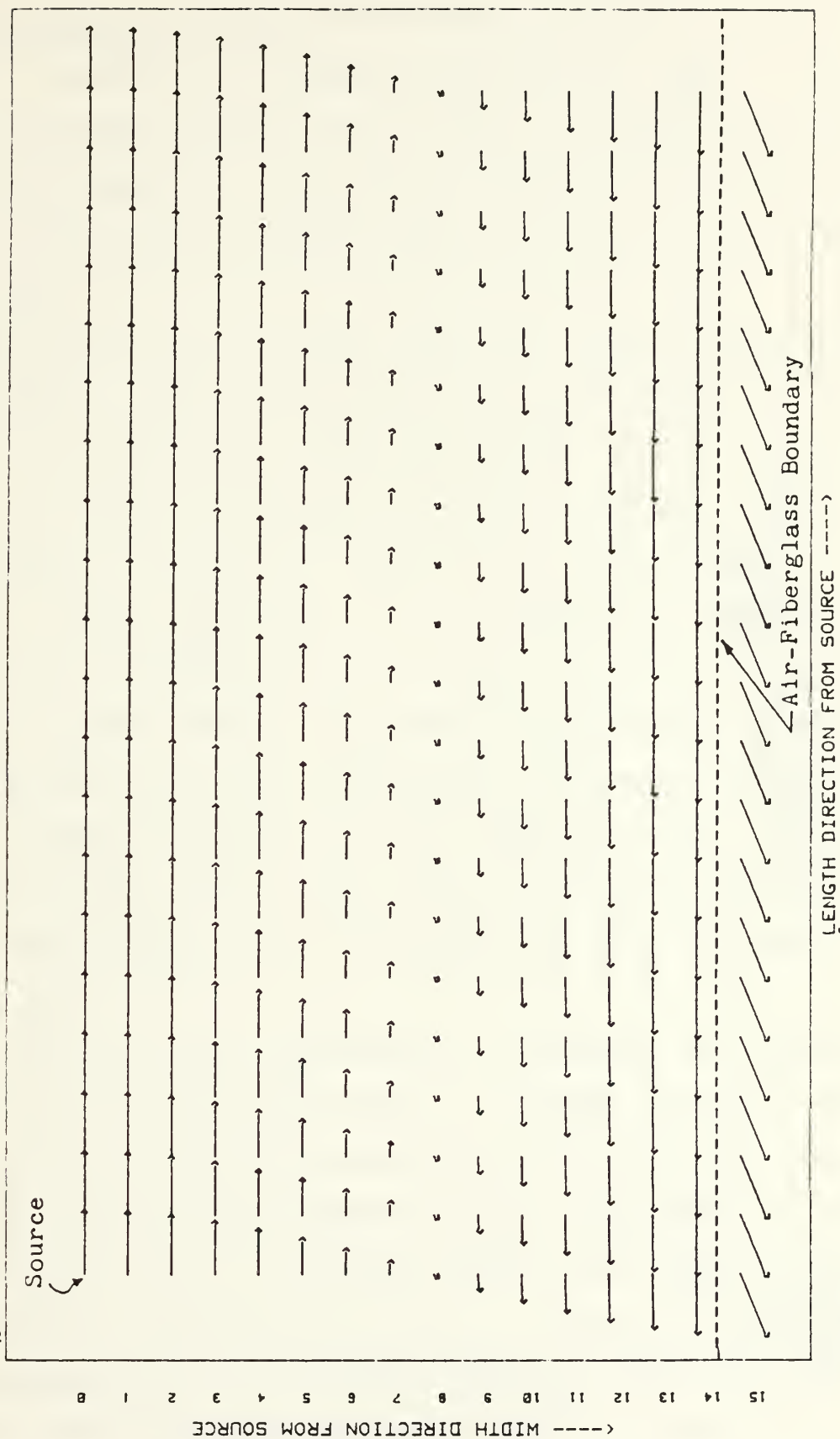


Figure 3.32 Theoretical [010] Mode Pressure Distribution for Sample #5

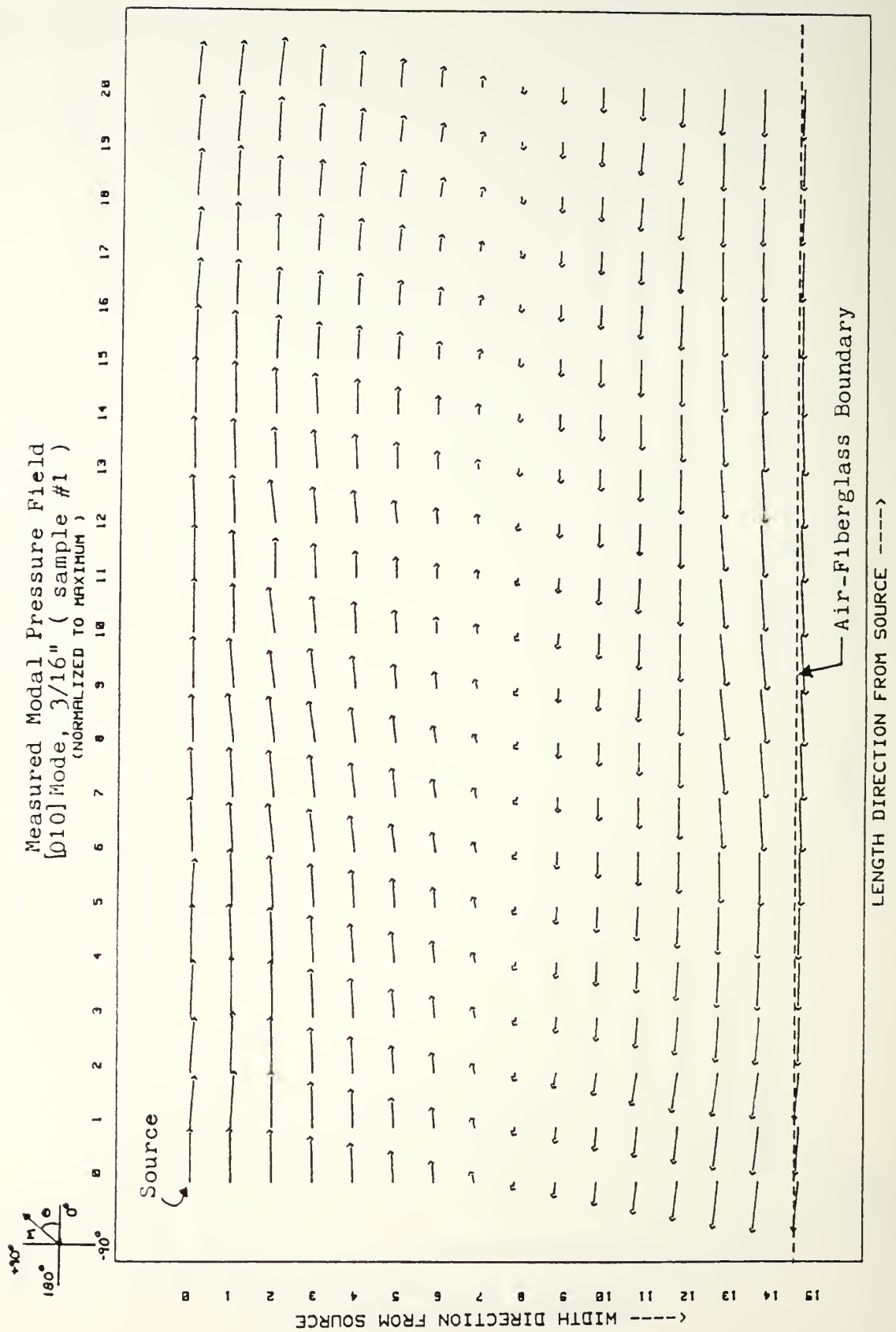


Figure 3.33 Experimental [010] Mode Pressure Distribution for Sample #1

air-fiberglass boundary from the theoretical plot of the 3/16" (sample #1) fiberglass strip compared to the theoretical plot of the 1 7/8" (sample #10) fiberglass strip. This can be seen in Figures 3.27 and 3.28, respectively. This effect is not seen in the theoretical plots of the [010] mode for sample #1 (Figure 3.31) and for sample #5 (Figure 3.32)

- (3) The effects of mode overlap become more evident as sample thickness is increased by comparing the measured and calculated modal pressure fields for the same sample thickness. For example, compare Figure 3.29 (sample #1) to Figure 3.30 (sample #10) for the [100] mode and Figure 3.33 (sample #1) to Figure 3.34 (sample #5) for the [010] mode.
- (4) The pressure distribution at the air-fiberglass boundary shows the effect of the relative size and sign of k_{1z} and k_{2z} by noting that for the thickest samples the pressure phasor's angle increases as the interface is approached. For the [100] mode compare the theoretical plot for sample #1 (Figure 3.27) to the theoretical plot for sample #10. (Figure 3.28) and for the [010] mode compare the theoretical plot for sample #1 (Figure 3.31) to the theoretical plot for sample #5 (Figure 3.32).

The primary reason for comparing the calculated and measured pressure distributions was to verify which mode was excited and to check its purity. The determination of whether the expected mode had been excited was made by comparing the calculated and measured pressure field plots for the thinnest fiberglass strip (3/16"). For the [100] mode the nodal plane runs normal to the length direction from grid point (10,0) to grid point (10,15). Travelling across the nodal plane, a 180 degree phase shift in the pressure phasor is observed, with the pressure magnitude reaching a maximum at the cavity

Measured Modal Pressure Field
 [010] Mode, 11/16" (sample #5)
 (NORMALIZED TO MAXIMUM)

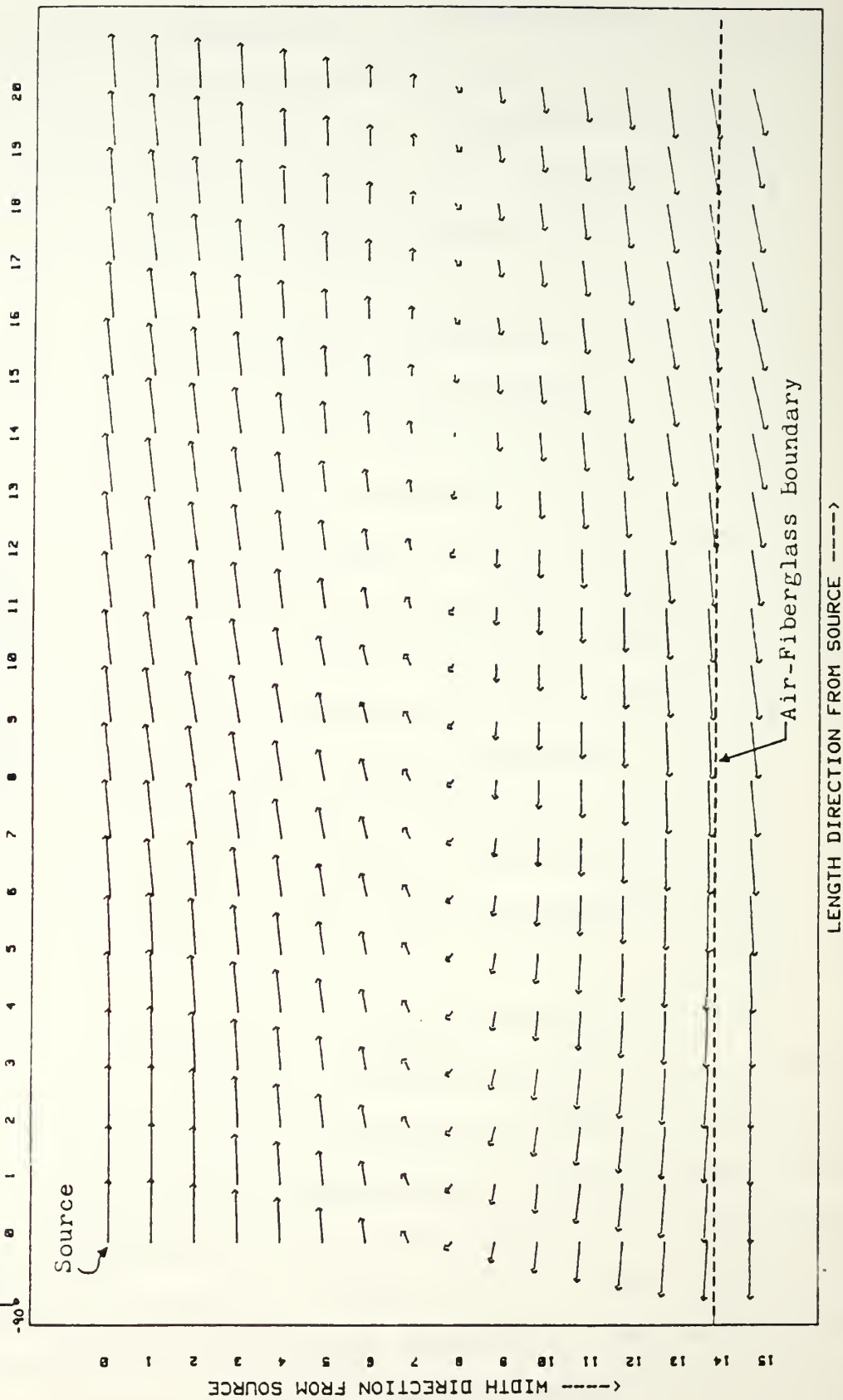


Figure 3.34 Experimental [010] Mode Pressure Distribution for Sample #5

boundaries normal to the length direction. Likewise, for the [010] mode the nodal plane is normal to the width direction falling half-way between the boundaries parallel to the length direction. The pressure phase also changes 180 degrees in crossing this nodal plane, with its magnitude reaching a maximum at the fiberglass boundary and opposite wall.

The purity of these modes is retained only with the thinner samples and becomes contaminated as thicker samples are introduced. This is clearly seen by comparing Figures 3.29 and 3.30.

IV. COMPARISON OF RESULTS AND CONCLUSION

A. COMPARISON OF THE COMPLEX WAVE NUMBER

The complex wave number may be written in terms of its real and imaginary parts as the wave number k and the absorption coefficient α , respectively. Figure 4.1 shows the wave number k as a function of frequency for each method. Values of k determined by the new method fall between those found by Yaniv's method (the upper bound) and by Beranek's Material Properties method in the isothermal limit (the lower bound). For example, at 600 Hz the value of the wave number determined by the new method was within 6% of the value determined by Yaniv's method. The values of k from the probe tube experiment are about twice those determined by the new method. This is to be expected, since the particle velocity in the probe tube experiment was normal to the air-fiberglass boundary, i.e., was in the direction of higher measured flow resistance. (Note that although the [010] mode also has particle velocity normal to the fiberglass surface, the best fit value of R_{DC} (15,000 MKS Rayl/m) was used to calculate both the complex wave number and characteristic impedance).

The absorption coefficient as a function of frequency is displayed in Figure 4.2 for each method. The values determined by the new method fall about those obtained by Beranek's Material Properties method (in the isothermal limit). For example, at 600 Hz the value of the absorption coefficient determined from the new method falls with 17% of the value determined by Yaniv's method. Again, the values determined using the probe tube method were about twice those measured by the new method. The cause of the dip in the values of the absorption coefficient determined by Yaniv's method is not known.

Figure 4.3 displays the phase speed in the porous material as a function of frequency for each method. Values determined by the new method are bounded by

Wave Number vs Frequency

(COMPARISON--ALL METHODS)

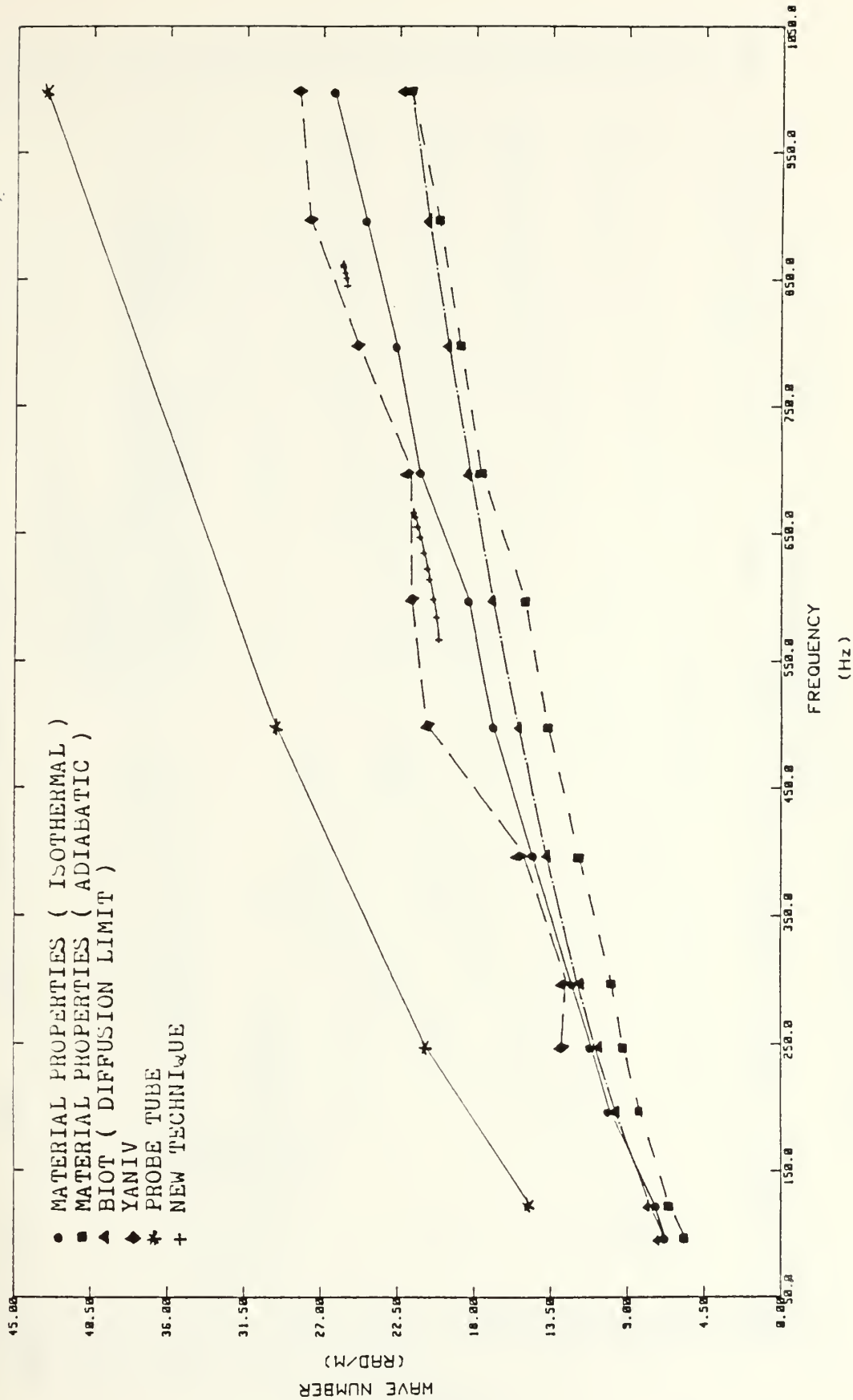


Figure 4.1 k vs f For All Methods

Absorption Coeff. vs Frequency

(COMPARISON--ALL METHODS)

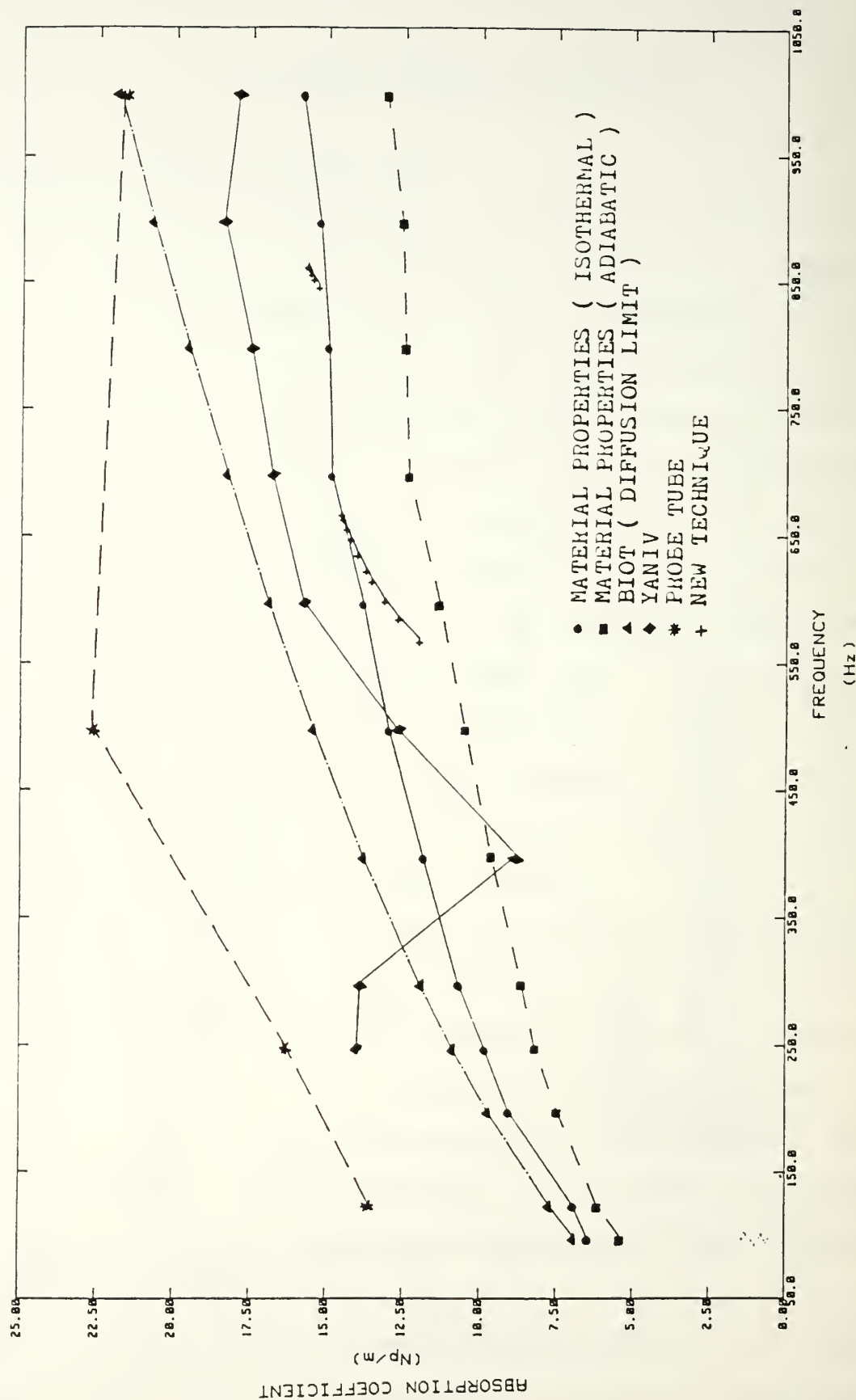


Figure 4.2 a vs f For All Methods

Phase Speed vs Frequency

(COMPARISON--ALL METHODS)

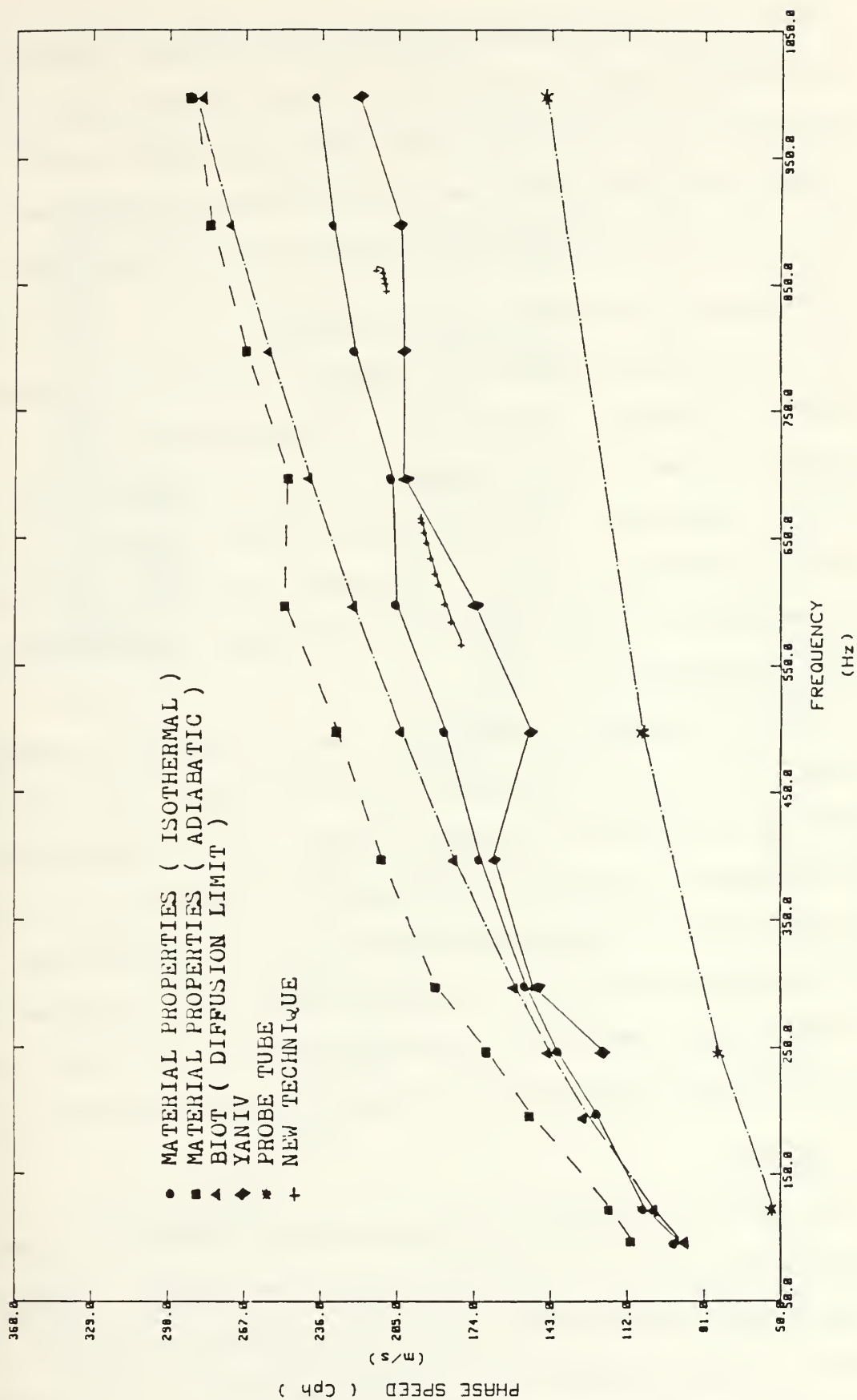


Figure 4.3 cph vs f For All Methods

those found by Yaniv's method and by Beranek's Material Properties method (in the isothermal limit). For example, at 600 Hz the phase speed determined by the new method is within 7% of the value determined by Yaniv's method. The values of phase speed determined by the probe tube method are approximately one-half of those found by the new method for the same reason discussed above.

B. COMPARISON OF THE CHARACTERISTIC IMPEDANCE

The normalized characteristic impedance as a function of frequency for all methods is displayed in Figure 4.4. Values determined by the new method are bounded by those from the adiabatic and the isothermal material properties method. Values from the new method plot almost directly on top of the Biot theory in the diffusion limit. For example, at 600 Hz the value determined by the new method fell within 26% of that determined by Yaniv's method and within 20% of the impedance tube value.

Figure 4.5 displays the impedance phase as a function of frequency for each method. The values determined by the new method fall about the values determined by the material properties method. The low frequency values (< 200 Hz) determined by the impedance tube method are thought to be in error due to the difficulties in measuring the distance to the first node in that method. It is not known why the values of the phase extracted using the new method from the [100] mode data increase for decreasing frequency, since in the low frequency limit, the phase should approach -45 degrees (pure diffusion of sound pressure).

C. CONCLUSION

The ability to determine a material's DC flow resistance from parameters of the resonance curve in a plane wave resonator was verified. Additionally, the values of both the complex wave number and characteristic impedance determined from the new method compared well with classical methods; the values obtained by the various methods agree with each other to within 26%.

[Z_{char}]/Rho-C vs Frequency

(COMPARISON--ALL METHODS)

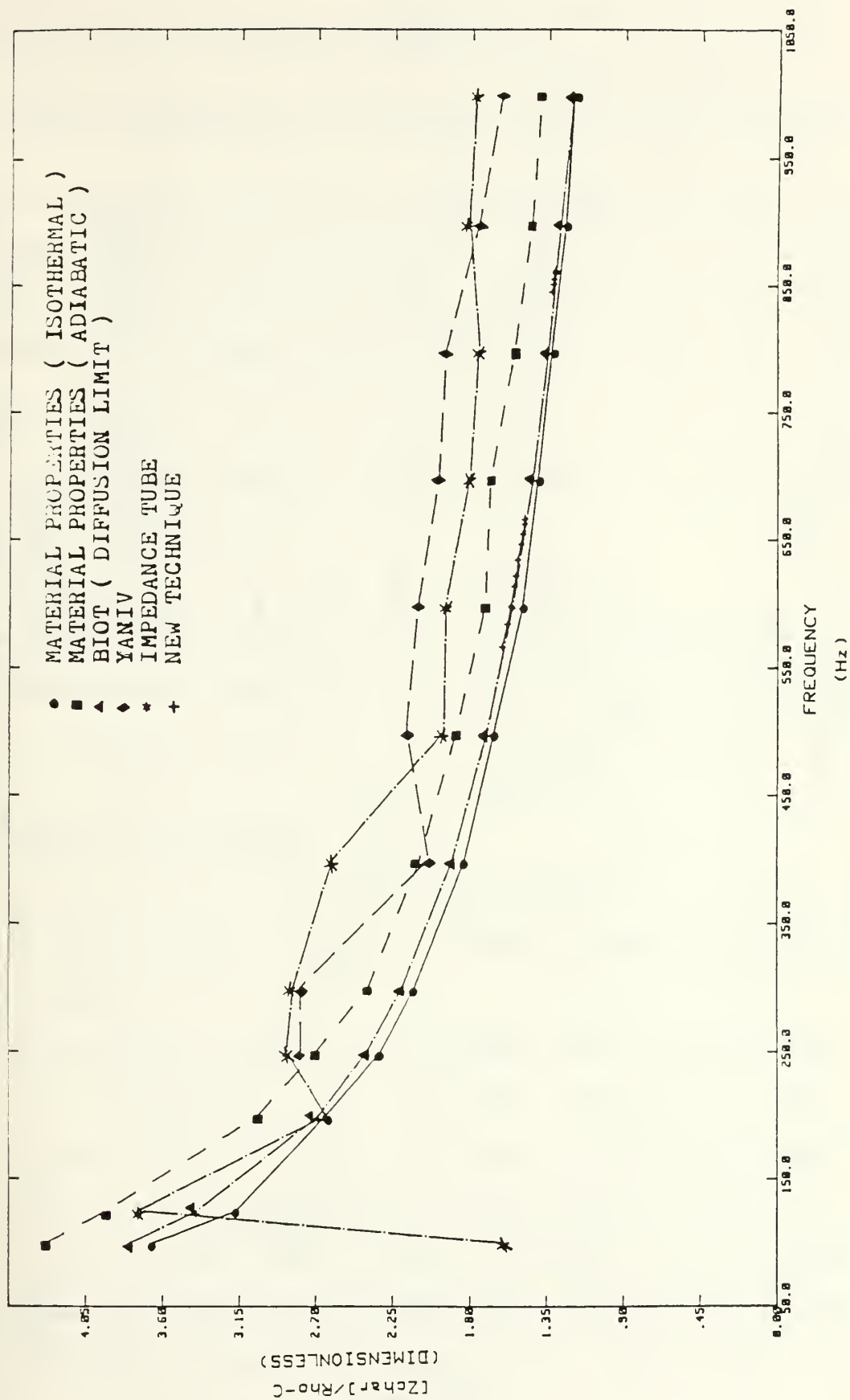


Figure 4.4 $\tilde{Z}_{char}/\rho_0 C$ vs f For All Methods

Imped. Phase vs Frequency

(COMPARISON--ALL METHODS)

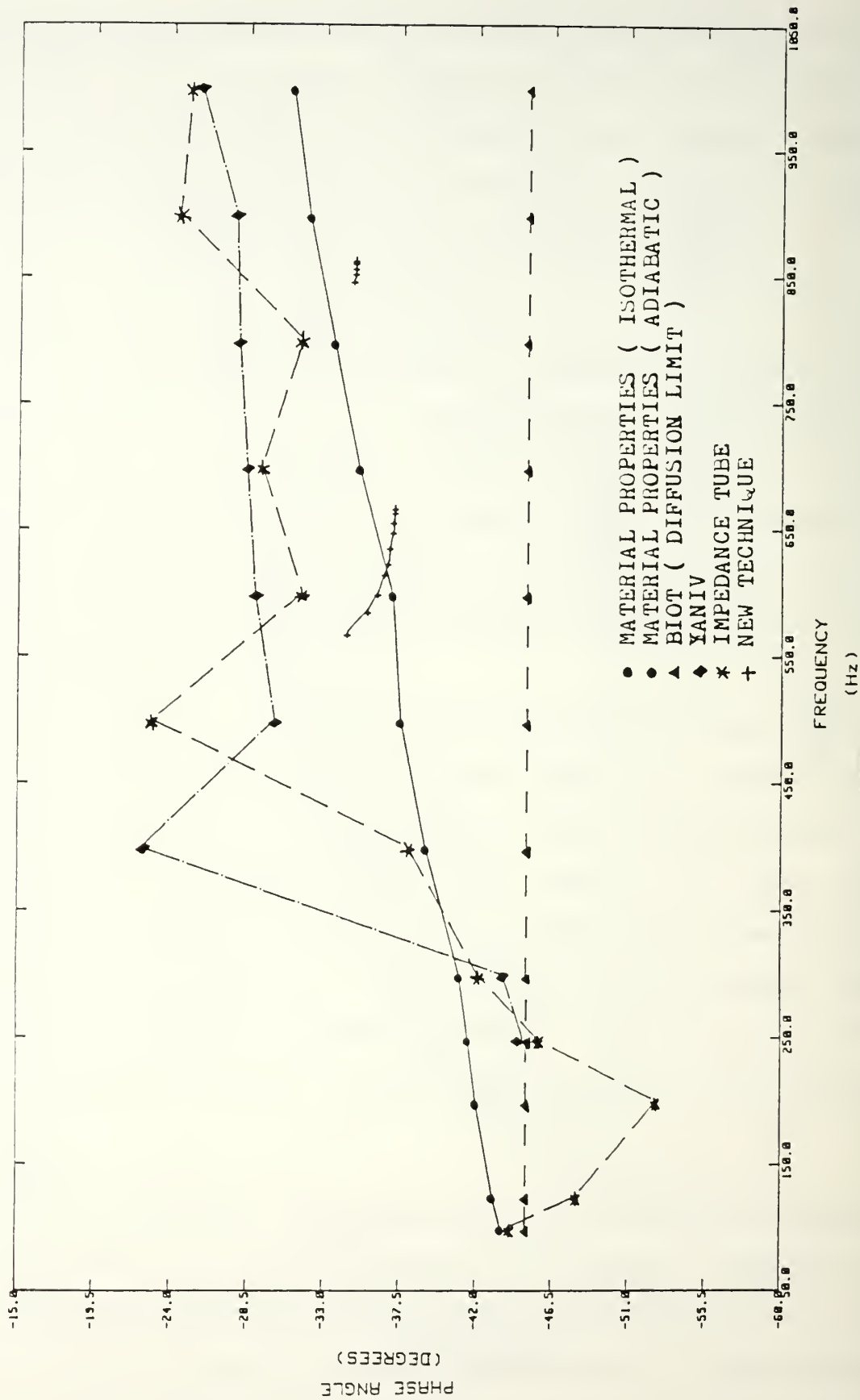


Figure 4.5 ϕ_{char} vs f For All Methods

METHOD OF SOLUTION OF THE DISPERSION RELATION AND ITS IMPLEMENTATION

The method used to find the roots of the dispersion relation (Eq. (2.51)) was Ward's method [Ref. 19, pp. 169-170]. This method is not the only method available to find the roots of a complex transcendental equation but is easy to understand and to implement, as no derivatives are needed.

1. WARD'S METHOD

If we let the polynomial $f(z)$ be a function of the complex variable $z = x + iy$ such that

$$f(z) = u(x,y) + iv(x,y) , \quad (\text{A.1.1})$$

it can be shown that $f(z)$ has a zero $a = b + id$ if and only if $u(b,d) = v(b,d) = 0$. This pair of simultaneous equations in $u(x,y)$ and $v(x,y)$ may be conveniently solved in two ways. First, one can seek to minimize

$$u^2(x,y) + v^2(x,y) \quad (\text{A.1.2})$$

or, secondly, one can minimize

$$w(x,y) = |u(x,y)| + |v(x,y)|. \quad (\text{A.1.3})$$

Since no derivatives are employed, this method seems well suited for finding multiple roots.

Ward's technique is based on the knowledge that in every neighborhood of a point (x,y) such that $w(x,y) \neq 0$, there exists a point $w(x',y')$ such that $w(x',y') < w(x,y)$. At a given step in the process, which is iterative, the current value of $w(x,y)$ is compared with the values $w(x+h,y)$, $w(x-h,y)$, $w(x,y+h)$ and $w(x,y-h)$ until a smaller value is found (if possible). The coordinates yielding this smaller value of x and y are used in the next iterative step. Should these four points yield no decrease in $w = |u| + |v|$, the increment h is decreased

by some amount and the process is repeated. As with other methods which can show convergence within certain limits, there is no guarantee of convergence with this method.

2. IMPLEMENTING WARD'S METHOD

In order to apply Ward's method to find the roots of the dispersion relation, it must be separated into its real and imaginary parts. To do so note that the parameters \tilde{k}_{1z} and \tilde{k}_{2z} , and $\tilde{\alpha}(\tilde{\omega})$ are functions of $\tilde{\omega}$, they may be separated into their respective real and imaginary components (these three terms also have complex parameters buried within them which are frequency dependent). Although tedious, it is necessary with this method.

Once each parameter has been reduced to its simplest complex form (real and imaginary portions), these can be inserted back into the dispersion equation and by use of complex arithmetic, the dispersion relation may be recast in the form

$$\text{Re}\{\text{Dispersion Relation}\} + j\text{Im}\{\text{Dispersion Relation}\} = 0$$

and Ward's Method of Eq. (A.1.3) may be now implemented in a computer algorithm.

The numerical analysis program written using Ward's Method required the following inputs for each sample thickness:

(1) Measured Quantities

- a) f_c (measured in the cavity)
- b) Q (measured in the cavity)

(2) Cavity Parameters

- a) Length of the cavity, L . (in x-direction)
- b) Width of porous material, d_2 . (sample thickness)
- c) Width of remaining bulk fluid, d_1 .
- d) Mode number in the long direction. $\{n = 0 \text{ for the } [010] \text{ mode, } n = 1 \text{ for the } [100] \text{ mode}\}$

(3) Fluid and Porous Solid Parameters

- a) Adiabatic fluid sound speed, c_f . (@ 23°C, 345.2 m/s)
- b) Fluid bulk density, ρ_f . (@ 20°C, 1.21 Kg/m³)
- c) Adiabatic ratio of specific heat of fluid, γ . (@ 20°C, 1.402)
- d) Prandtl number, Pr. (@ 20°C, 0.733)
- e) Porosity, P. (≈ 1.0)

(4) Program Parameters

- a) Angular frequency increment, $\Delta\omega$.
- b) Damping frequency increment, $\Delta\beta$.
- c) An ending criterion for $w(\omega, \beta)$.

(5) Initial Estimate of R_{DC}

- a) If no a priori knowledge of material's flow resistance, then assume very high or low value as the starting point.
- b) Perform a DC flow resistance experiment to extract a mean value for R_{DC} .

Once these quantities are entered, the program calculates its first $w(\omega, \beta)$ based on the initial inputs of f_c and Q . This value of $w(\omega, \beta)$ will be compared to the four incremental values of $w(\omega \pm \Delta\omega, \beta \pm \Delta\beta)$, that is, it compares the initial $w(\omega, \beta)$ with

$$w(\omega + \Delta\omega, \beta)$$

$$w(\omega - \Delta\omega, \beta)$$

$$w(\omega, \beta + \Delta\beta)$$

$$w(\omega, \beta - \Delta\beta)$$

Which ever is the lowest, those coordinates in ω, β space are chosen as the new values and the process is continued until $w(\omega, \beta)$ is less than the ending criterion. The output converts the roots of ω and β to f_c and Q .

This process is continued for each sample thickness, and the resulting values can be plotted either as Q vs f_c or as f_c vs sample thickness and compared with the respective curve after loss corrections to Q are made. An evaluation is made as to whether R_{DC} is too high or too low, the value of R_{DC} changed and the process repeated for this new value of R_{DC} for all samples. This iterative process is completed when the roots are found for a value of R_{DC} which provides the best fit curve through the measured data. With this value of R_{DC} and the roots for each sample thickness determined, the characteristic impedance and complex wave number may be calculated by use of Eq. (2.56) and Eq. (2.57).

DETERMINATION OF THE THEORETICAL MODAL PRESSURE DISTRIBUTION IN A PLANE
WAVE RESONATOR WITH AN ACOUSTICALLY ABSORBING MATERIAL

The equation that governs the pressure distribution in the bulk fluid (region 1) is:

$$\delta \tilde{p}_1 = \left[-j\tilde{\omega}\rho_f \cos[k_x x] \tilde{\phi}_{10} \cos[\tilde{k}_{1z}(z-d_1)] \right] e^{j\tilde{\omega}t} . \quad (B.1.1)$$

The equation that governs the pressure distribution in the porous material (region 2) is, after substituting Eq. (2.62) for $\tilde{\phi}_{20}$:

$$\delta \tilde{p}_2 = \left[-j\tilde{\omega}\rho_f \cos[k_x x] \tilde{\phi}_{10} \frac{\cos[\tilde{k}_{1z}d_1]}{\cos[\tilde{k}_{2z}d_2]} \cos[\tilde{k}_{2z}(z+d_2)] \right] e^{j\tilde{\omega}t} . \quad (B.1.2)$$

With the value of R_{DC} known, along with the roots of the dispersion relation for a given sample thickness, the pressure distribution in region 1 and region 2 can be calculated.

In the experimental measurement of the modal pressure field, the quadrature component of the pressure was zeroed at the reference position of (0,0,1) to set a reference point such that both theory and experiment could be compared. The 0,0 indicates the grid point (0,0) and the 1 indicates that the receiver probe tube was located in the ceiling of the cavity. To set the reference at $x = 0$, $z = d_1$ such that the phase of the pressure distribution at this point is zero, requires that

$$\tilde{\phi}_{10} = 1 / \underline{-\text{ATN}(-\omega/\beta)} . \quad (B.1.3)$$

To calculate the theoretical modal pressure distribution, start at the reference location of $x = 0$ and $z = d_1$ and incrementally move away from this position in increments of Δx and Δz such that the theoretical grid points match those existing in the actual cavity.

LIST OF REFERENCES

1. Rayleigh, Lord, Theory of Sound, Vol. II, Macmillan, 1929.
2. Scott, R. A., "The Absorption of Sound in a Homogeneous Porous Medium", Proceedings of the Physical Society of London, Vol. 58, pp. 165-183, 1945.
3. Taylor, H. O., "A Direct Method of Finding the Value of Materials as Sound Absorbers", Phys. Rev., Vol. 2, pp. 270-287, 1913.
4. Beranek, L. L., Acoustic Measurements, Wiley, 1949.
5. Yaniv, S. L., "Impedance Tube Measurements of Propagation Constant and Characteristic Impedance of Porous Acoustical Material", J. Acoust. Soc. Am., Vol. 54, pp. 1138-1142, 1973.
6. Chung, J. Y. and Blaser, D. A., "Transfer Function Method of Measuring In-Duct Acoustic Properties I. Theory II. Experiment", J. Acoust. Am., Vol. 68(3), pp. 907-921, 1980.
7. Mason, J. T., "A Comparison of Impedance Measurement Techniques in Air", Master's Thesis, Naval Postgraduate School, Monterey, California, March 1984, DTIC Report #A143638 and J. Acoust. Soc. Am., Vol. 74, p. 63. 1983.
8. Biot, M. A., "Theory of Propagation of Elastic Waves in a Fluid-Saturated Porous Solid., I. Low-Frequency range, II. Higher Frequency Range", J. Acoust. Soc. Am., Vol. 28, pp. 168-194, 1956.
9. Biot, M. A., "Mechanics of Deformation and Acoustic Propagation in Porous Media", J. Appl. Phys., Vol. 33, pp. 1482-1489, 1962.
10. Biot, M. A., "Generalized Theory of Acoustic Propagation in Porous Dissipative Media", J. Acoust. Soc. Am., Vol. 34, pp. 1254-1261, 1961.
11. Baker, S. R., "Sound Propagation in a Superfluid Helium Filled Porous Solid: Theory and Experiment", Ph. D. Dissertation, UCLA Dept. of Physics, Tech. Report #45, 1986.
12. Landau, L. D. and Lifshitz, E. M., Fluid Mechanics, Vol. 6 of Course of Theoretical Physics, Pergamon Press, 1959.
13. Morse, P. M. and Ingard, K. U., Theoretical Acoustics, Princeton University Press, 1968.
14. Johnson, D. L., Koplik, J. and Dashen, R., "Theory of Dynamic Permeability and Tortuosity in Fluid-Saturated Porous Media", submitted to J. Fluid Mech., 1986.
15. Plona, T. J. and Johnson, D. L., "Acoustic Properties of Porous Systems: I. Phenomenological Description", in Physics and Chemistry of Porous Media, AIP Conference Proceedings Number 107, D. L. Johnson and P. N. Sen, editors, Hugh C. Wolfe, series editor, American Institute of Physics, New York, pp. 89-103, 1984.

16. Rudnick, I. and Baker, S. R., "Measurement of the Biot Structural Factor δ for Sintered Bronze Spheres", in Proceedings of the IEEE 1985 Ultrasonics Symposium, B. R. McAvoy, Editor, pp. 1039-1044, 1985.
17. Kinsler, L. E. and others, Fundamentals of Acoustics, 3rd Edition, Wiley, 1982.
18. Sears, F. W. and Salinger, G. L., Thermodynamics, Kinetic Theory, and Statistical Thermodynamics, 3rd Edition, Addison-Wesley, 1975.
19. Carnahan, B. and others, Applied Numerical Methods, Wiley, 1969.

INITIAL DISTRIBUTION LIST

	Number of Copies
1. Defense technical Information Center Cameron Station Alexandria, Virginia 22304-6145	2
2. Superintendent Attn: Library, Code 0142 Naval Postgraduate School Monterey, California 93943-5002	2
3. Naval Postgraduate School Physics Department Attn: Steven Garrett, Code 61Gx Monterey, California 93943-5000	1
4. Naval Postgraduate School Physics Department Attn: Steven Baker, Code 61Ba Monterey, California 93943-5000	10
5. Naval Postgraduate School Physics Department Attn: Anthony Atchley, Code 61Ay Monterey, California 93943-5000	2
6. LT Frederick F. Schulz 5100 26th Street North Arlington, Virginia 22207	1
7. Foundation Research Council Director of Research Attn: Gilbert Howard, Code 012 Naval Postgraduate School Monterey, California 93943-5000	2
8. Chairman, Department of Physics (Code 61) Naval Postgraduate School Monterey, California 93943-5000	1
9. Applied Physics Laboratory Dr. Morris Shulkin University of Washington Seattle, Washington 98105	1
10. Office of Naval Research Dr. Logan Hargrove Physics Division, Code 1112 800 N. Quincy Street Arlington, Virginia 22217	1

DUDLEY KNOX LIBRARY
NAVAL POSTGRADUATE SCHOOL
MONTEREY, CALIFORNIA 93943-6002

Thesis

S36452 Schulz

c.1 Development of a new
method of measuring the
characteristic impedance
and complex wave number
of a porous acoustic ma-
terial.

Thesis

S36452 Schulz

c.1 Development of a new
method of measuring the
characteristic impedance
and complex wave number
of a porous acoustic ma-
terial.

thesS36452

Development of a new method of measuring



3 2768 000 73623 5

DUDLEY KNOX LIBRARY